



SAPIENZA
UNIVERSITÀ DI ROMA

High gradient ultra-high brightness RF photoinjector optimization

Università degli studi di Roma La Sapienza
Dottorato di Ricerca in Fisica degli acceleratori – XXX Ciclo

Candidate
Michele Croia
ID number 1104662

Thesis Advisor
Dr. Massimo Ferrario

A thesis submitted in partial fulfillment of the requirements
for the degree of Doctor of Philosophy in Physics
October 2017

Thesis defended on January 2018
in front of a Board of Examiners composed by:
Prof. Cesare Bini (chairman)
Prof. Alessandro Cianchi
Prof. Vittoria Petrillo

High gradient ultra-high brightness RF photoinjector optimization
Ph.D. thesis. Sapienza – University of Rome

© 2017 Michele Croia. All rights reserved

This thesis has been typeset by L^AT_EX and the Sapthesis class.

Author's email: Michele.Croia@lnf.infn.it

*Dedicated to
my wife Benedetta, my son Tommaso and my daughter Priscilla.
You supported me and you enlightened my path during the PhD.*

Contents

Introduction	7
1 A brief introduction on accelerators history and beam transport in linacs	11
1.1 Introduction to particle accelerators and applications	11
1.2 Beam dynamics regimes and emittance concept	16
1.2.1 Beam emittance lower limit	20
1.3 The rms envelope equation	20
1.3.1 Correlated emittance oscillations	21
1.4 Free Electron Lasers	24
2 Photoinjector physics	29
2.1 RF photo-gun	30
2.2 RF effects on the longitudinal phase space distribution	32
2.3 RF acceleration effects in the transverse phase space	36
2.4 Emittance growth due to the space charge forces	39
2.5 Emittance compensation in photoinjectors for high brightness beams	41
2.5.1 Space charge induced emittance compensation	42
2.5.2 Invariant envelope and double emittance minimum	46
2.6 Particle emission from the cathode	51
2.6.1 Thermionic emission	52
2.6.2 Photoelectric emission	54
2.6.3 Field emission	57
3 Advanced High Brightness Photoinjectors	61
3.1 Accelerating peak field enhancement at the cathode surface	62
3.1.1 Peak field enhancement techniques	63
3.1.2 Cryogenic operation in RF structures to increase the peak field	68
3.2 Ultra high field cryogenic RF S-band gun	71
3.3 High gradient, higher frequency and Ultra-High brightness C-band gun	83

3.3.1	Gun parameters and starting point for the optimization . . .	84
3.3.2	High gradient C-band gun optimization	86
3.3.3	High gradient C-band gun working point	88
3.4	A possible SPARC_LAB upgrade	94
4	SPARC_LAB Photoinjector optimizations	101
4.1	Particle motion in a solenoid	103
4.2	The SPARC_LAB gun solenoid	106
4.3	Beam based alignment at SPARC_LAB	111
4.4	Printed circuit skew quadrupoles at SPARC_LAB	120
	Conclusions	125

Introduction

In the past decades particle accelerators and especially RF photoinjectors had an impressive development, thanks to which a lot of applications were possible from the industrial one up to the medical use. Historically accelerators were developed for nuclear and particles physics but nowadays only a small part of accelerators are devoted to science, most of them are used for applications.

The current request for scientific scope, especially for particle physics, is an higher and higher beam energy. The energy scale of TeV in the center of mass, in the past decades was reached. In the most recent and powerful proton particle accelerator Large Hadron Collider (LHC), was reached the impressive energy value in the center of mass of about 13 TeV and a Luminosity of about $10^{34} \text{ cm}^{-2}\text{s}^{-1}$. The energy request from the scientific community has led to some accelerators project that exceed 50 Km length.

In order to overcome these accelerator dimensions and especially to reduce costs, a good solution is the plasma acceleration. With this new accelerator technique the accelerating gradients can be a factor 10^3 more intense with respect to the modern RF technology. Nowadays plasma acceleration does not look like a chimera anymore, it was been demonstrated as a proof of principle but a lot of work is still to do in order to reach a good beam quality such that it can be used in accelerator facilities and in applications.

Most of the applications in fact demand an high beam quality: ultra low energy spread and ultra high brightness beams. High brightness beams means bunches with an high peak current and a low emittance. These quality parameters are also necessary in order to perform a good matching between beams from accelerator and plasma in the so called external injection scheme for plasma acceleration. For example the energy spread that a bunch acquires during the acceleration is proportional to the length of the bunch that is injected into the plasma. Furthermore with a low transverse emittance the beam can be easily focused in order to reach the transverse matching conditions between beam and plasma.

Beam brightness is a fundamental parameter for applications as the Free Electron Laser (FEL) that is able to produce X rays, where the gain length (L_g) is inversely

proportional to the electron beam brightness $L_g \propto B^{-1/3}$ in the Self Amplified Spontaneous Emission (SASE) X-ray regime.

These requests in the electron beam quality means that a perfect control of the bunches along the beam line is necessary, starting from the bunch generation in an electron gun up to the accelerator end, especially in the photoinjector region where the beam is not yet relativistic and is in the so called space charge regime.

From these requests the beam transport has to be optimized, especially at low energies, performing a fine tuning of the machine parameters and of the positions of the machine elements along the beam line. To do that have to be fixed: a proper position for the first accelerating section, an integrated magnetic field of the gun solenoid, an optimal bunch compression scheme and mostly avoid any misalignments of the accelerating sections and of any magnetic components. In the photoinjector, where the beam is not yet relativistic, any misalignments can generate a transverse kick of the entire beam and a distortion of the beam transverse shape. The bunch can easily degrade its quality parameters in the photoinjector region, which in case of standard applications (e.g. industrial or medical) could be not so detrimental. Differently in case of applications as the ones here discussed (plasma acceleration or FEL) it is a serious matter which compromise the application itself. One of the effects of a low beam quality is a more difficult matching with the linac and subsequently with the plasma channel.

In order to meet these stringent beam quality parameter requests, I optimized the beam dynamics of a new ultra high gradient 1.6 cells C-band (5.712 GHz) gun able to reach 240 MV/m as a peak field. By means of the ultra high gradient a better control of the space charge forces inside the bunch is possible. After optimizations on this electron gun a proper emittance compensation scheme was found through simulations with the software General Particle Tracer (GPT) (see Ref. [1]). Simulations showed the possibility to have, with a 100 pC beam and an energy of about 150 MeV, an emittance value of about $\epsilon_{n,rms} \approx 55 \text{ nm}$ and a final beam brightness value of about $B \approx 5 \times 10^{16} \text{ A/m}^2$.

In order to optimize the present and future SPARC_LAB beam line, I wrote an algorithm able to evaluate transverse misalignments of a gun solenoid with coils powered with opposite currents. This algorithm was checked successfully in a dedicated run at SPARC_LAB. Using this algorithm the estimation of misalignments was about 1 mm and 0.5 mm in the transverse planes. During the SPARC_LAB machine operations we measure a bunch centroid displacement due to the misaligned solenoid. Aligning the solenoid to the found values we will improve the centroid orbit displacement of about 99.4%. Furthermore it will be possible avoid transverse kicks and distortions of the transverse beam shape and emittances i.e. the fundamental

parameters to match simultaneously the beam with plasma in both transverse planes. The beam can have different spots and emittances in the x, y transverse planes due to laser on cathode misalignments, or due to some residual misalignments on the gun solenoid or on accelerating sections. I studied the possibility to insert Printed Circuit(PC) skew quadrupoles inside the future SPARC_LAB gun solenoid. By GPT simulations these PC skew quadrupoles will be able to reduce spot differences in σ_x versus σ_y , respectively spots in the x and y planes, from 14% up to about 1% and a differences in the emittances ϵ_x versus ϵ_y from 14% up to 5%. A first design of these PC quadrupoles was made, and we are planning to install them in the future SPARC_LAB gun solenoid.

Chapter 1

A brief introduction on accelerators history and beam transport in linacs

To understand the modern particle accelerators, and choices adopted, is useful to briefly summarize their history from the origins, when a static electric field to accelerate the particles was used. With the increase in available technology, choices have been made, which have allowed in addition to an increase in the final beam energy, a big leap forward in the quality of accelerated beams.

We discuss the main concepts of beam transport in a modern accelerator introducing one of the main beam figure of merit, the rms emittance. Since in the next chapters we will present beam dynamics optimizations for new photoinjectors in order to minimize the beam emittance, we introduce also the emittance lower limit considering the single electron in the quantum mechanical limit.

1.1 Introduction to particle accelerators and applications

Accelerators and their components have experienced a great development from their origin. The basic concept of a particle accelerator is to accelerate particles (electrons, protons, ions...) with an electric field, while the magnetic field is used to bend or focus the particles in the transverse plane.

Initially in order to accelerate the particles a static electric field was used, but the energy gain was very low. In fact the energy gain in an electrostatic accelerator is proportional to an applied electrostatic potential between an anode and a cathode and the particle charge:

$$E_g = q\Delta V. \quad (1.1)$$

The electrostatic field was used in the first particle accelerators, such as the belt charged Van der Graaf accelerator and the cascaded voltage Cockroft-Walton generator that were able to reach, in different configurations, up to some MV potentials. These tools opened the way to the possibility to obtain electrons with relativistic velocity, and furthermore the birth of nuclear and particle physics using particle accelerators. The main limitation using an electrostatic accelerator is the breakdown, increasing the potential ΔV a discharge between anode and cathode can occur stopping the energy gain to tens MeV.

Since there is not a net energy gain using a multi stages electrostatic accelerator, by the necessity to increase particle energies a multi stages time dependent field accelerator is required. The first multi stages linear accelerator was designed by Wideroe in his thesis work, taking advantage from a time dependent electric field. The idea was to alternate increasing length drift tubes followed by alternating voltage

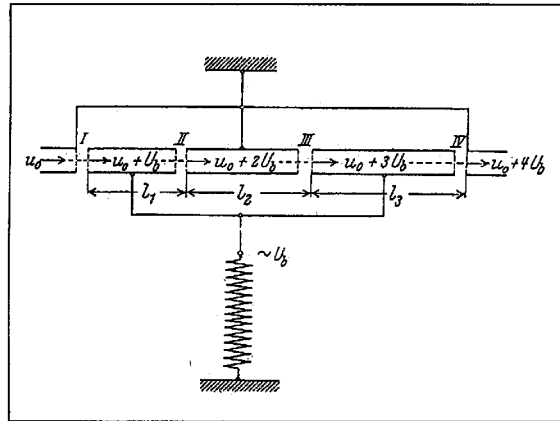


Figure 1.1. Original sketch of the Wideroe linear accelerator, from his thesis work (see Ref. [2]).

gaps where particle were accelerated. The radiofrequency (RF) phase changes by 180 degrees while particles travel from on gap to the next (see Figure 1.1). The energy gain in a Wideroe linac is proportional to the applied potential ΔV in a gap and the number of the energy gaps N_{gap}

$$E_{g,W} = qN_{gap}\Delta V \quad (1.2)$$

With the Cyclotron invention, i.e. a circular structures designed to use the same accelerating RF gap many times and a superimposed magnetic field to bend the

particles, the idea of an accelerator based on resonance of particles motion with a time dependent electromagnetic field was introduced. In the Synchro-Cyclotron the frequency field is varied in time with the particle energy grow up, to compensate relativistic effects, and was possible reach around 100 MeV of kinetic energy for heavy particles. Nowadays a lot of cyclotrons are still used for nuclear and medical application.

With the high power and high frequency RF invention it was possible push a wave inside a close resonant cavity to directly accelerate particle beams. This important innovation allowed to build the Alvarez accelerator (see Figure 1.2) i.e. the first standing wave linear accelerator (linac).



Figure 1.2. Inside view of the Alvarez linac at FermiLab. Drift tubes shield particles from the electromagnetic field, so when they pass inside they do not accelerate. Between tubes there are gaps in which particles perceive the electromagnetic field in the tank and they are accelerated by the electric field.

The Alvarez structure was very similar to the Wideroe one, but the accelerating gaps and tubes were enclosed in a metallic structure, to avoid the losses to electromagnetic radiation of the Wideroe structure at higher RF frequency. Most modern accelerators use the same principles but mainly in a traveling wave configuration i.e. waves that travel in the structure do not have fixed nodes inside the resonant cavities.

In parallel to the linac development, the synchrotron accelerator idea was developed. In synchrotron particles travel in a ring with at least one accelerating stage, while the other parts of the ring is filled with bending and focusing magnets.

As a consequence of the accelerators technological development and using the parasitic synchrotron radiation many unexpected applications became possible. Accelerators and synchrotron radiation became powerful tools in order to study the structure of

matter and a probe to study biological components.

Light production experienced a similar impressive development with the invention by John Madey of the first Free Electron Laser (FEL) at Stanford University. A FEL is able to produce coherent and tunable synchrotron radiation in a spectrum where conventional lasers are not able to cover. A completely free drifting electron cannot radiate due to the momentum conservation. An accelerated relativistic charge can radiate around his instantaneous velocity vector, and an emission due to a transverse force is greater than the emission due to a parallel force by a factor γ^2 (see Ref. [3]), where

$$\gamma = \left(1 - \frac{v^2}{c^2}\right)^{-\frac{1}{2}} = (1 - \beta^2)^{-\frac{1}{2}} \quad (1.3)$$

is the Lorentz factor. As we will see in next sections, injecting an electron beam into a periodic magnetic field B_u , provided by an magnetic device called undulator, electrons start to bunch and emit photons at a wavelength λ_s

$$\lambda_s = \frac{\lambda_u}{2\gamma^2} (1 + K_u^2) \quad (1.4)$$

where λ_u is the undulator period and K_u is the so called undulator parameter defined as

$$K_u = \frac{e\lambda_u B_u}{2\pi mc} \approx 0.93 B_u(T) \lambda_u(cm) \quad (1.5)$$

The emitted wavelength can be changed varying the bunch energy (γ) or the undulator parameters (λ_u, B_u). The bunch parameters are fundamental both for the emitted wavelength and the FEL layout. In order to reach the desired wavelength the bunch energy must be tuned. For example the Linac Coherent Light Source (LCLS) at SLAC is able to tune the wavelength from 22 to 1.2Å varying the electron bunch energy from 3.5 to 15 GeV [4]. Defining the FEL gain length L_g as the length after which the emitted power increases by a factor e (Nepero number), it strongly depends on the bunch transverse emittance ϵ i.e. the bunch phase space volume:

$$L_g \propto \left(\frac{\epsilon}{I_{peak}}\right)^{1/3} \quad (1.6)$$

where I_{peak} is the bunch peak current. Reducing the emittance and increasing the peak current is possible to reduce the gain length and so the length of undulators. Furthermore in order to increase the bunch peak current, short bunches and low energy spreads are required.

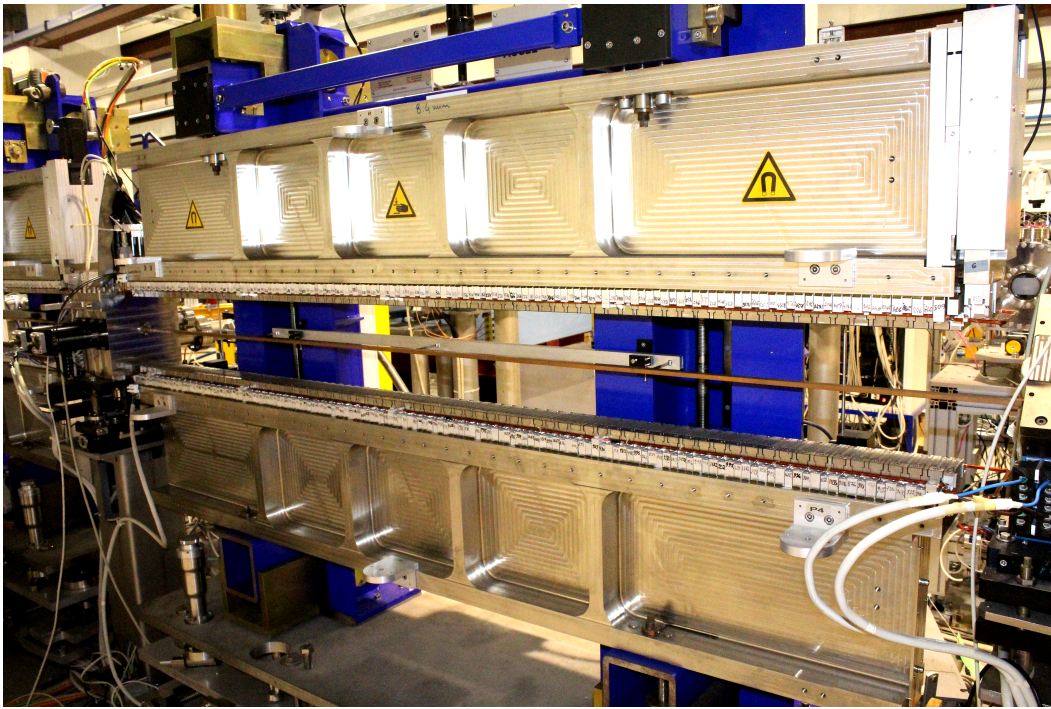


Figure 1.3. An undulator module at SPARC_LAB facility INFN-LNF. There are 75 undulator period, the length of each one is $\lambda_u = 2.8\text{cm}$. The magnetic field B is generated by permanent magnets arranged around the beam pipe. In order to vary the magnetic field on axis it is possible to vary the distance between permanent magnets (i.e. distancing the gray module in the figure) reaching a maximum undulator parameter of $K_{max} = 2.2$. The SPARC_LAB FEL is able to work in SASE (Self Amplified Spontaneous Emission) and seeding scheme, with High Harmonic Generation (HHG).

1.2 Beam dynamics regimes and emittance concept

As can be seen from FEL requirements, and in general by many applications, a high quality beam is required in order to tune the proper wavelength and reduce the FEL length and costs. The main parameter that describes the transverse beam quality is the transverse emittance. To understand the concept of this parameter we introduce some basis on the particle beam dynamics (see Ref. [5]).

An ideal beam is made by particle orbits that flow with any orbit intersections. For a beam that propagates on the z axis, this happens when in a given longitudinal position all bunch particles have identical transverse velocities, or when the magnitude of the slopes of the trajectories in the transverse directions x and y are linearly proportional to the displacement from the z axis of beam propagation.

Since in an accelerator the transverse particle momentum is much smaller than the longitudinal momentum, $p_{x,y} \ll p_z \approx p$, we can use the paraxial approximation $x' = dx/dz = p_x/p_z \approx p_x/p$ and $y' = dy/dz = p_y/p_z \approx p_y/p$.

Figure 1.4 shows the trajectories evolution for a laminar beam without energy spread that passes through a thin lens. Considering that focusing forces in the lens are linearly proportional to the displacement from the z axis, the beam focus maintaining a laminar flow and the orbit do not cross each other. After passing the beam waist the particles start to diverge. In the below part of the figure there is the trace space distribution (x, x') that is equivalent to the phase space distribution $(x, p_x \approx x'p)$ when p is constant i.e. without beam acceleration. The beam phase space in the laminar ideal motion is a segment with zero area. The effect of the beam propagation in the phase space is to modify the slope of the distribution.

Figure 1.5 shows a non laminar beam where the particles trajectories cross each other during the motion and in a fixed longitudinal position there is a random distribution of the beam particle velocities. Due to this all particles are focused by the lens in different longitudinal positions.

A convenient figure of merit of the beam is the phase space area occupied by the particles, and we call it emittance ϵ . Usually it is represented by an ellipse that contains all the particles in the phase space, and this kind of parameter is also known as geometric emittance. We can define an emittance for each plane obtaining ϵ_x , ϵ_y , ϵ_z if we consider respectively the phase spaces (x, x') , (y, y') and (z, z') and we can measure this parameter in *m rad*. The reasons of the elliptical shape come from the fact, the trajectory of each particle in phase space moves on an ellipse. The ellipse equation in this case is written as

$$\gamma x^2 + 2\alpha_x x x' + \beta_x x'^2 = \epsilon_x \quad (1.7)$$

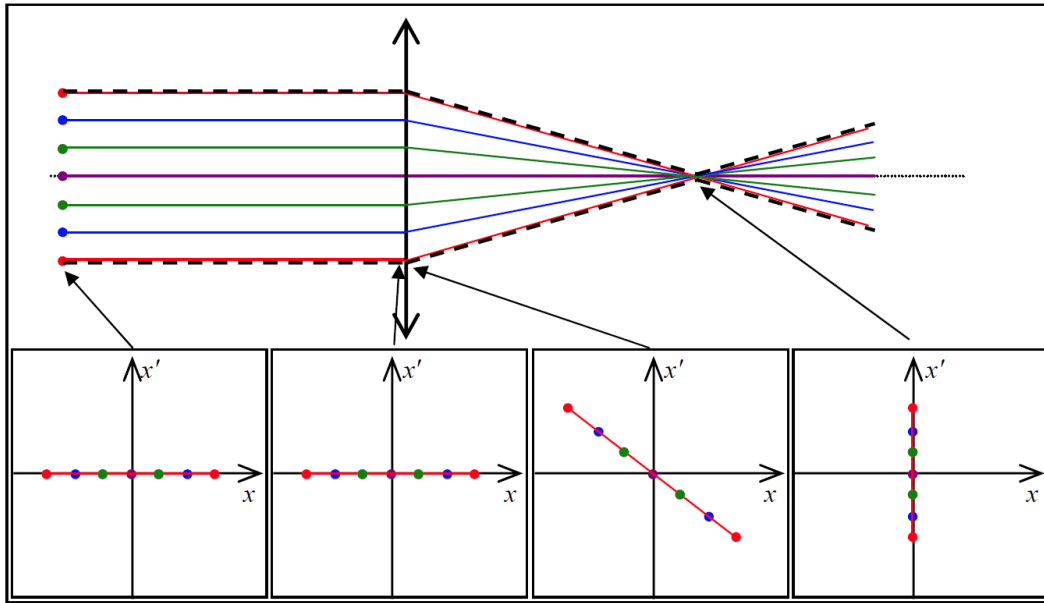


Figure 1.4. In the top of the figure particle trajectories of a laminar beam pass through a lens. In a fixed longitudinal position the particles have the same transverse velocity so that they are focused in the same longitudinal position. Below is represented the beam phase space area, the propagation through the lens generates a rotation of this segment. From Ref. [6]

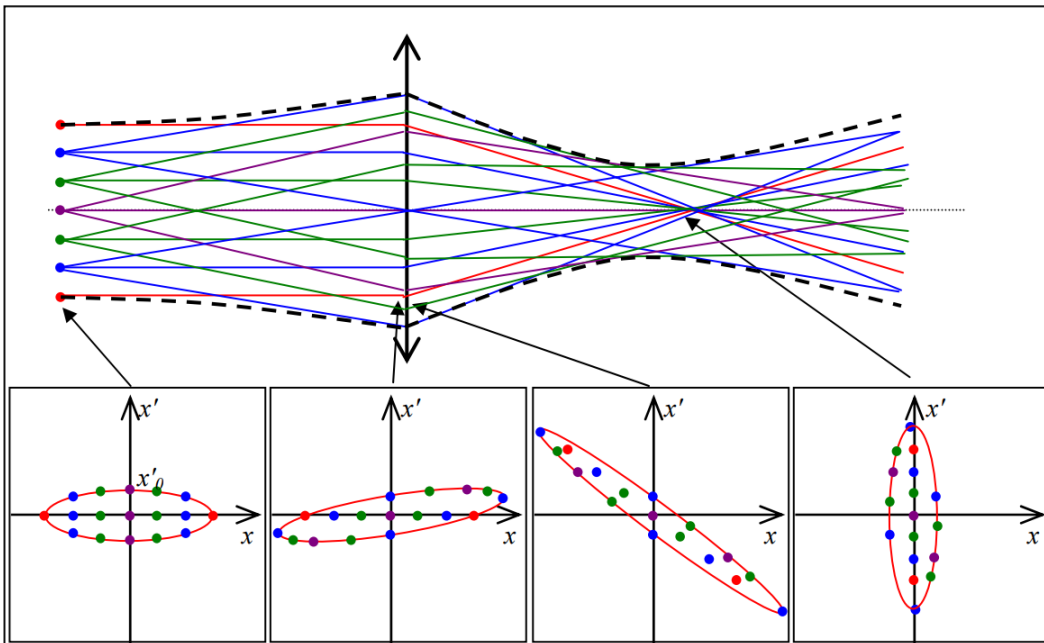


Figure 1.5. In the top of the figure particle trajectories of a non-laminar beam pass through a lens. Due to different velocities in the same position the beam focus in one point is impossible. Below corresponding phase space rotation. The phase space area is the geometric emittance. A low emittance allow to transport the beam parallel over a long distance, and focus it to a small spot size. From Ref. [6]

where x and x' are the particle coordinates and α_x, β_x and γ_x are the so called Twiss parameters, related by

$$\beta_x \gamma_x - \alpha_x^2 = 1 \quad (1.8)$$

Defining the beam spot size x_{max} , its derivative $(x_{max})'$ and the beam divergence x'_{max} it is possible to relate them to the ellipse parameters as

$$x_{max} = \sqrt{\beta_x \epsilon_x} \quad (1.9)$$

$$(x_{max})' = -\alpha \sqrt{\frac{\epsilon}{\beta}} \quad (1.10)$$

$$x'_{max} = \sqrt{\gamma_x \epsilon_x} \quad (1.11)$$

these relations are represented in the phase space in Figure 1.6

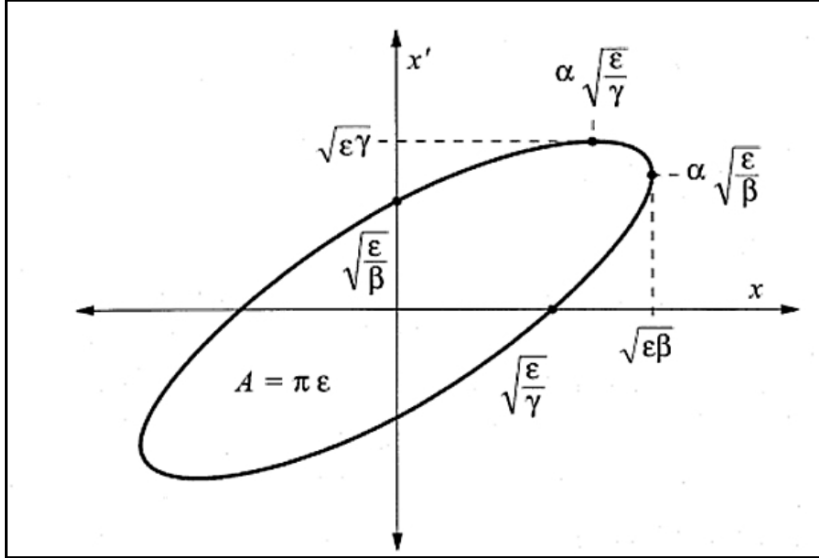


Figure 1.6. Relation between the twiss parameters and the ellipse in the phase space. [7]

The evolution of a system in the phase space can be considered as mapping of the phase space onto itself, relating the two representative points $M(T)$ and $M(T')$ at two different times. The Liouville Theorem establishes that in the evolution of a conservative system, the time derivative of the state densities in the phase space is zero, so that the density of the states is conserved. By the Liouville Theorem the six dimensional phase space volume (6-D emittance) occupied by an isolated bunch subject to non dissipative forces is an invariant during the system evolution. A real beam in an accelerator can be subject to phenomena that do not conserve the phase space volume and so the 6-D emittance. For example scattering between particles

or with residual gas in the pipe, synchrotron radiation emission, wake fields, space charge effects (see Ref. [8]). The geometric emittance is a conserved quantity during the motion if the system is isolated i.e. also without acceleration.

Because non linear forces acting on the beam distort the beam phase space area, the ellipse equation does not well describe the geometric emittance anymore. It is convenient to introduce the root mean square, or rms, emittance i.e. a statistical definition of the emittance that depends on the particle distribution in the phase space through a distribution function $f(x, x', z)$. This figure of merit better measures the beam quality than the phase space area. To introduce the rms emittance we have to consider that the projection of the ellipse on the x and x' axis corresponds to the rms values of the distribution such that

$$\sigma_x = \sqrt{\beta_x \epsilon_{x,rms}} \quad (1.12)$$

$$\sigma_{x'} = \sqrt{\gamma_x \epsilon_{x,rms}}. \quad (1.13)$$

and the second moments of the distribution function $f(x, x', z)$ are

$$\begin{aligned} \sigma_x^2(z) = \langle x^2 \rangle &= \int_{-\infty}^{\infty} \int_{-\infty}^{\infty} x^2 f(x, x', z) dx dx' \\ \sigma_{x'}^2(z) = \langle x'^2 \rangle &= \int_{-\infty}^{\infty} \int_{-\infty}^{\infty} x'^2 f(x, x', z) dx dx'. \end{aligned} \quad (1.14)$$

Considering also the degree of (x, x') correlations described by

$$\sigma_{xx'}^2(z) = \langle xx' \rangle = \int_{-\infty}^{\infty} \int_{-\infty}^{\infty} xx' f(x, x', z) dx dx' \quad (1.15)$$

that is called correlation term.

It is possible to obtain the definition of the rms emittance as

$$\epsilon_{rms} = \sqrt{\sigma_x^2 \sigma_{x'}^2 - \sigma_{xx'}^2} \quad (1.16)$$

The rms emittance is an important parameter that gives information about the beam phase space distribution under the effect of linear or non-linear forces acting on the beam. In fact the rms emittance depends not only by the area occupied by the particles, but also on distortions produced by non linear forces.

When the beam is subject to acceleration, the divergence $x' = p_x/p_z$ varies due to the increase of p_z . In this case it is more convenient to use the so called rms normalized emittance $\epsilon_{n,rms}$, for which the transverse momentum $p_x = p_z x' = mc\beta\gamma x'$ is used instead of the divergence. This invariant beam figure of merit is related to the rms

emittance by (see Ref. [9]):

$$\epsilon_{n,rms} = \epsilon_{rms}(\beta\gamma) \quad (1.17)$$

where β, γ are the relativistic parameters in equation 1.3.

1.2.1 Beam emittance lower limit

Since in the next chapters we will study the beam dynamics for a new photoinjector able to minimize the beam emittance, it can be interesting to evaluate the emittance lower limit. To do that, we have to evaluate the single particle emittance. In the classical limit the single particle emittance is zero. Considering the quantum mechanics limit the six dimensional phase space volume occupied by a particle is \hbar^3 . Due to the Heisenberg indeterminacy principle

$$\sigma_x \sigma_{p_x} \geq \frac{\hbar}{2} \quad (1.18)$$

Introducing the reduced compton wavelength λ

$$\lambda = \frac{\hbar}{mc} \quad (1.19)$$

the single particle emittance can be written as [5]

$$\epsilon_{n,rms}^{1e^-} \geq \frac{1}{2} \frac{\hbar}{mc} = \frac{\lambda}{2} \quad (1.20)$$

Inserting in the previous equation the electron invariant mass, it is possible to obtain the emittance lower limit for an electrons beam.

$$\epsilon_{n,rms}^{1e^-} \geq 1.9 \times 10^{-13} m \quad (1.21)$$

1.3 The rms envelope equation

A fundamental equation to describe the beam and its evolution during transport and acceleration is the so called root mean square envelope equation [5]. It is a differential equation that well describes internal and external forces acting on the beam

$$\sigma_x'' + \frac{\gamma'}{\gamma} \sigma_x' + k_{ext}^2 \sigma_x = \frac{\epsilon_{n,rms}^2}{\gamma^2 \sigma_x^3} + \frac{k_{sc}}{\gamma^3 \sigma_x} \quad (1.22)$$

where the symbol ' means a spatial derivative (d/dz).

The longitudinal acceleration appears in the equation as a damping term proportional to $\frac{\gamma'}{\gamma}$. The third term of the equation take in to account external linear forces acting

on the beam in the form $F_x = \pm kx$. Usually these forces are provided by external focusing elements like solenoids and quadrupoles.

The fourth and fifth terms represent inner defocusing beam forces. The term $\frac{\epsilon_{n,rms}^2}{\gamma^2 \sigma_x^3}$ expresses the effect of the beam emittance that acts as a defocusing term, and it can be interpreted as an outward pressure on the beam envelope caused by the particles spread in transverse trajectory. It depends by the beam energy as $\frac{1}{\gamma^2}$, for high energy beam this effect is negligible if σ_x does not become too small. The fifth term considers the Coulomb repulsion between charged particles and it is proportional to the beam current along the beam: $k_{sc} = \frac{I}{2I_A}$ where $I_A = \frac{4\pi\epsilon_0 mc^3}{e} = 17kA$ is the Alfvén current for electrons. As we will see in the next chapter the space charge force scales as $1/\gamma^2$. Computing the moment of this force to calculate the term that enters in the envelope equation for a relativistic beam, we obtain that the space charge term in the envelope equation strongly depends by the beam energy as $\frac{1}{\gamma^3}$. From these consideration in an high energy beam the defocusing forces, space charge and emittance pressure, decrease significantly.

It is convenient to introduce the laminarity parameter ρ that is the ratio between space charge term and emittance pressure term in 1.22 and measure the relative importance of the space charge term with respect to the emittance one during beam propagation

$$\rho = \frac{I}{2I_A \gamma} \frac{\sigma^2}{\epsilon_n^2}. \quad (1.23)$$

When $\rho > 1$ the beam is space charge dominated, if $\rho \gg 1$ a laminar flow occurs and the particle trajectories do not cross each other during propagation. When $\rho < 1$ the emittance pressure is dominant and space charge forces can be neglected. The transition between two regimes occur at $\rho = 1$, it coincide with a transition energy

$$\gamma_{tr} = \frac{I}{2I_A} \frac{\sigma^2}{\epsilon_n^2}. \quad (1.24)$$

1.3.1 Correlated emittance oscillations

One of the space charge effects in the bunch evolution are longitudinal correlations inside the bunch. It means that the beam envelope evolution depends also by an internal longitudinal bunch coordinate ζ . It is convenient consider the bunch made by n slices with different envelopes $\sigma_s(z, \zeta)$. These longitudinal correlations lead to consider a correlated emittance defined by

$$\epsilon_{rms,cor} = \sqrt{\langle \sigma_s^2 \rangle \langle \sigma_s'^2 \rangle - \langle \sigma_s \sigma_s' \rangle}. \quad (1.25)$$

Considering the simplest case in which the bunch is made by only two slices it means each slice has its own envelope and the previous definition of the correlated

emittance reduces to

$$\epsilon_{rms,cor,2slices} = | \sigma_1 \sigma_2' - \sigma_2 \sigma_1' | \quad (1.26)$$

The total rms emittance can be obtained superimposing the uncorrelated rms emittance with the correlated rms emittance.

From slices scheme follow that is impossible to match simultaneously all bunch slices. For example considering a focusing channel without acceleration the single slice equation is

$$\sigma_s'' + k_{ext}^2 \sigma_s = \frac{k_{sc,s}}{\gamma^3 \sigma_s} \quad (1.27)$$

A stationary solution of the envelope equation corresponds to a slice propagation with an invariant envelope called Brillouin flow $\sigma_{r,B}$ in which internal and external forces are balanced

$$\sigma_{r,B} = \frac{1}{k_{ext}} \sqrt{\frac{I g(\zeta)}{2 \gamma^3 I_A}} \quad (1.28)$$

where $g(\zeta)$ expresses the local dependence of the current along the bunch. Because the current can vary in different slices while k_{ext} is a constant value in all the focusing channel it means that each slice has a different matching conditions inside the same focusing channel. Some slices will be matched in the focusing channel and some slices will oscillate around the own equilibrium solution. Considering an initial slice mismatching δ_0 with respect to its envelope equilibrium the perturbed solution is [5]

$$\sigma_s = \sigma_{s,B} + \delta_0 \cos(\sqrt{2} k_{ext} z) \quad (1.29)$$

From 1.29 all slices oscillate with the same frequency $\sqrt{2} k_{ext}$ (known as plasma frequency) around its equilibrium solution. These envelope oscillations lead to a correlated emittance oscillations described by

$$\epsilon_{rms,cor} = \frac{1}{4} k_{ext} \sigma_{r,B} \left| \frac{\Delta I}{I} \delta_0 \sin(k_{ext} z) \right| \quad (1.30)$$

derived for a two slice model where ΔI is the current difference between two slices. The correlated emittance oscillations are sinusoidal and periodically return to zero, it means that correlated emittance is reversible. Properly tuning the length and the strength of the focusing field is possible to balance the coupling between longitudinal and transverse motion induced by space charge.

In order to keep under control the correlated emittance growth during acceleration, a proper tune of the focusing field and a proper position of the first accelerating structure will be described in the next chapter. From the introduction of the FEL requirements in the previous section an high quality bunch i.e. low emittance, low energy spread and high peak current is required. It is convenient to introduce a

fundamental bunch quality parameter called Brightness defined as the ratio between two times the peak bunch current I and the square of the rms normalized emittance $\epsilon_{n,rms}$

$$B = \frac{2I}{\epsilon_{n,rms}^2} \quad (1.31)$$

From the gain length definition 1.6, an high brightness beam is able to reduce the gain length in an FEL, reducing also the final cost of the undulators. Typically in an X-ray FEL: $I \approx \text{few kA}$ and $\epsilon_{n,rms} \approx \lambda/4\pi$ referring to slice values, as the ones proposed for LCLS-II [10]. Because the emittance can be interpreted as an internal beam pressure, an high brightness beam measure also the possibility to focus to a very small spot sizes as the ones required for the beam-plasma matching conditions in the plasma acceleration.

1.4 Free Electron Lasers

Since in Chapter 3 we will discuss the possibility to use a bunch produced by an high gradient C-band gun followed by an X-band linac to drive a Free Electron Laser (FEL) we briefly present this device (see Ref. [11]), pointing out some scaling laws useful for our case.

In classical electromagnetism, a charged particle radiates energy in the form of electromagnetic radiation when it accelerates. This effect is the principle behind many useful sources of radiation across a wide range of the electromagnetic spectrum. The free electron laser is one such source, which, due to a Doppler frequency up-shifting of emitted radiation by relativistic electrons, is particularly well-suited to generating short-wavelength X-rays. Electromagnetic energy may be extracted from the kinetic energy of a relativistic electron beam by propagating it along the axis of a periodic lattice of alternating magnetic dipolar fields, known as an ‘undulator’. This forces the beam to undulate transversely, thus causing the electrons to emit electromagnetic radiation. The fundamental wavelength emitted is proportional to λ_u/γ^2 , where λ_u is the undulation period, typically a few centimetres, and γ is the relativistic Lorentz factor of the electrons, which is typically several thousand for X-ray emission. The first experiments at Stanford in 1953 generated the first incoherent undulator radiation at visible and millimetre wavelengths. Typically in FEL interaction is present a density modulation (bunching) of the electron beam along its (longitudinal) direction of propagation, and radiation energy extraction from the axial kinetic energy of the beam. It was not until 1971 that Madey (see Ref. [12]), published a theory of the FEL that described a small gain process in a relativistic electron beam/undulator system, which he hypothesized could generate coherent X-ray radiation.

The first amplification and lasing from a FEL device was demonstrated in a small-gain infrared FEL oscillator system at Stanford a few years later (see Ref.[13]). A classical FEL description was produced by Bonifacio-Pellegrini-Narducci leading to the so called high-gain regime of FEL operation. In this high-gain regime, the radiation power increases exponentially as the electron beam and radiation co-propagate along the FEL undulator, and an initially small source, which may originate as noise, can be amplified by many orders of magnitude before the process saturates. In essence, the high-gain FEL interaction is a positive feedback process — the electrons emit radiation, which affects their position (phase) and thus causes them to emit with greater coherence. The effect is a collective (also called cooperative) process, and is a form of collective Thompson scattering. X-ray FELs operate in the Compton regime, in which space-charge effects are negligible.

In FEL devices a co-propagating radiation wavefront moves ahead of an electron. By

considering simple wave interference, only those wavelengths that propagate ahead of the electron by an integer number of wavelengths in one undulator period will constructively interfere after many such periods. These wavelengths, $\lambda_n = \lambda_1/n$ (where $n = 1, 2, 3, \dots$), are defined as being resonant, with other wavelength components tending to interfere destructively. The time taken for an electron propagating along the undulator axis, with mean speed \bar{v}_z , to travel one undulator period, $t' = \lambda_u/\bar{v}_z$, is the same time a resonant wavefront takes to travel the distance $\lambda_u + n\lambda_n$; that is, $t' = (\lambda_u + n\lambda_n)/c$. By these expressions, the following relation for the resonant wavelengths is obtained (see Ref. [14])

$$\lambda_n = \frac{\lambda_u}{n} \frac{1 - \bar{v}_z/c}{\bar{v}_z/c} \approx \frac{\lambda_u}{2n\gamma^2} (1 + a_u^2) \quad (1.32)$$

where a_u is the undulator parameter, that for a planar undulator is $a_u = K\sqrt{2}$ where $K \approx 0.9337B_0(T)\lambda_u(cm)$ where B_0 is the magnetic peak field. Only the fundamental and odd harmonic wavelengths of the radiation ($n = 1, 3, 5, \dots$) are emitted on-axis (see Ref. [14]). The produced wavelength can be tuned by changing either the electron energy (by varying γ) or the undulator parameter a_u .

We report now the scaling laws for 1 GeV low charge (30 pC) X-band RF linac driven FEL, that will be used in Chapter 4.

By the previous discussions the FEL process can be understood as a collective beam instability where billions of electrons cooperate to produce high peak power radiation within a narrow band around the resonant wavelength. A fraction of the electron kinetic energy is transformed in to electromagnetic energy until the process reaches saturation where the induced beam energy spread becomes too large and the resonant condition cannot be anymore satisfied. In order to enable the SASE instability to occur a number of conditions must be satisfied, most of them depending on the fundamental FEL parameter defined as:

$$\rho = \frac{1}{2\gamma} \left[\frac{\hat{I}}{I_A} \left(\frac{\lambda_u A_u}{2\pi\sqrt{\beta\epsilon}} \right)^2 \right]^{1/3} \quad (1.33)$$

where \hat{I} is the electron beam peak current, $I_A = 17$ kA is the Alfvén current, β the betatron wavelength and $\epsilon = \epsilon_n/\gamma$ the geometrical emittance being ϵ_n the normalized emittance. For a planar undulator $A_u = a_u[J_0(\xi) - J_1(\xi)]$, where J are the Bessel functions and the argument is $\xi = a_u^2/2(1 + a_u^2)$.

Assuming a uniform charge distribution within the electron bunch, the parameter ρ represents the efficiency of system such that the final saturation electromagnetic

power emitted by an electron beam is given by:

$$P_{sat} \approx \frac{1.6}{(1 + \eta)^2} \rho P_b \quad (1.34)$$

where $P_b = E_b I_b$ is the beam power and $\eta = f(\eta_d, \eta_\epsilon, \eta_\gamma)$ is a polynomial function that accounts for the contribution of 3D effects: radiation diffraction η_d , beam emittance η_ϵ and beam energy spread η_γ .

The undulator length required to achieve saturation, as predicted by the 3D model, is given by:

$$L_{sat}^{3D} \approx 20(1 + \eta)L_G^{1D} \quad (1.35)$$

where

$$L_G^{1D} = \frac{\lambda_u}{4\sqrt{3}\pi\rho} \quad (1.36)$$

is the 1D gain length. Equations 1.34 and 1.35 show that to maximize the extracted power within a reasonable undulator length, one has to get the highest possible FEL parameter compatible with the achievable electron beam parameters. In addition optimal FEL performances in terms of minimal radiation bandwidth and transverse coherence can be obtained when the beam energy spread satisfies the following condition:

$$\frac{\Delta\gamma}{\gamma} \leq \rho \quad (1.37)$$

and the beam normalized emittance is smaller of the radiation "emittance":

$$\epsilon_n \leq \gamma\lambda_r/4\pi. \quad (1.38)$$

Notice that equation 1.38 implies in our case that for optimal operation at a radiation wavelength of 3 nm the normalized emittance has to be smaller than 0.5 μm .

The difficulties to achieve such a high quality beam are partially mitigated by the fact that the radiation amplification process occurs on the scale of the cooperation length:

$$L_{coop} = \frac{\lambda_r}{4\sqrt{3}\pi\rho} \quad (1.39)$$

along a number of independent bunch slices of length $L_{slice} \approx 2\pi L_{coop}$, typically shorter than the bunch length, so that mainly slice parameters are important for the FEL process thus relaxing the conditions imposed by 1.37 and 1.38.

With a slice peak current of 3 kA and a beam slice emittance of 0.5 μm the computed value of the FEL parameters results to be $\rho = 1.43 \times 10^{-3}$, giving a slice length of $L_{slice} = 0.6\mu\text{m}$ and a undulator betatron function of 9.4 m (corresponding to a beam spot size $\sigma_x = 49 \mu\text{m}$). Assuming a beam with slice energy spread of 10^{-3} , thus satisfying condition 1.37, the corresponding extracted radiation power is about

2 GW with a saturation length of 17 m. The total number of photons emitted at saturation is approximately given by:

$$N_{ph} \approx 1.6 \frac{Q}{(1 + \eta)^2 \frac{\rho E_b}{h\nu_{ph}}} \quad (1.40)$$

showing the dependence on the total bunch charge Q .

Chapter 2

Photoinjector physics

The advent of high field radiofrequency photoinjector [15] [16] opened the way to colder and higher brightness electron beams. In order to obtain good beam quality parameters at the linac exit, a perfect control of the beam from its emission in the photocathode is necessary.

As we have seen in the previous chapter space charge degrades the bunch quality parameters causing an emittance growth. A proper tune of the accelerating field and phase in the RF gun, solenoid field and a proper position of the first accelerating section is necessary in order to perform an emittance compensation during acceleration.

The idea of an emittance compensation scheme for the space charge induced emittance growth in high brightness electron beams was proposed by Carlsten in Ref. [16]. We discuss the main beam physics aspects inside the photoinjector, taking into account the electron beam phase space distribution and its evolution under the effect of the RF field and space charge forces. From these consideration we introduce the emittance compensation concept using a solenoid, thanks to which it is possible to eliminate the linear part of the emittance growth due to the space charge forces when the beam is not yet relativistic. Furthermore, some other optimizations of this scheme were introduced, injecting the beam at its transverse waist in the first accelerating section and matching its spot size to the so called invariant envelope. The residual emittance after compensation can be of the order of the so called intrinsic emittance and to the emittance from the non linear space charge forces. We introduce some physical aspects of the particle emission from the cathode especially for the photoelectric and field emission, introducing the concept of microscopic roughness that contributes at the intrinsic emittance.

2.1 RF photo-gun

The idea of a Laser driven RF electron gun was firstly studied at Los Alamos National Laboratory and are currently under development new ideas in order to advance this device. With the advent of these devices was opened the possibility to realize low emittance, high current electron beam as the ones required for many application such as free electron lasers.

The basic idea is to illuminate a copper surface called photocathode with a time controlled laser, in order to extract electrons by photoelectric effect. The photon energy is $E_\gamma = h\nu$, the nucleus absorb the photon momentum transferring the energy to the emitted electron. This can be summarized by the reaction



where A represents the copper nucleus. The photoelectric effect requires that the photon energy has to be larger than the electron binding energy in copper.

Since space charge forces scale as $1/\gamma^2$, in order to keep immediately under control these forces in the emitted bunches, avoiding an emittance growth, the photocathode is embedded in an RF structure. The strong RF field in the cavity strongly accelerates particles to a relativistic energy.

The first use of a radiofrequency photoinjector was at LANL by Fraser, Sheffield and Gray (see Ref. [15]). In 1989 was introduced by Carlsten an emittance compensation scheme for high brightness beams, using a solenoid near the cathode [16].

The main advantages of a laser driven RF gun are that the time structure of the electron bunch can be controlled by the laser and that the electric field in RF cavities can be made very strong, so that the degrading effects due to space charge repulsion can be minimized. As we see in next chapters is under test the possibility to enhance the accelerating field in order to maximize the final beam brightness strongly reducing the emittance at the gun exit.

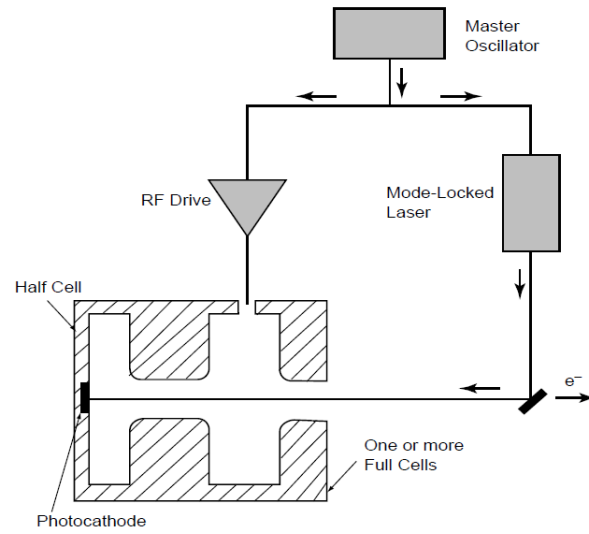


Figure 2.1. RF photoinjector design from Ref. [17]. The RF structure is filled by radio-frequency (RF) power from a klystron tube. The photocathode emits electrons when illuminated by a laser pulse. The strong RF electric field on the cathode surface immediately accelerates the electrons. The field reverses polarity by the time they reach the second cell of the gun for additional acceleration. A solenoid magnet (not shown) surround the gun. The same aperture provides the exit for the electrons and the entrance for the laser light.

2.2 RF effects on the longitudinal phase space distribution

The emitted unbunched electrons from the cathode perceive immediately a strong electric field so that the space charge effects can be minimized. A study of beam dynamics in an Rf gun needs to take into account the time variation of the RF field over the duration of the acceleration and over the duration of the electron pulse and the space charge repulsion. The so called slippage between beam and accelerating wave i.e. the variation of the RF phase is important at the beginning of the acceleration when the beam is not yet relativistic. These effects are well described in Ref. [18].

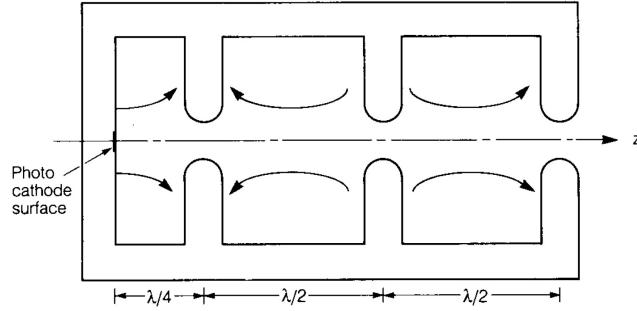


Figure 2.2. RF accelerating cells inside an RF laser gun. In order to increase at maximum the accelerating field perceived by the electrons emitted from the photo cathode, the first cell on the left is reduced to an half cell. From Ref. [18]

Considering the photocathode surface inside the first half RF cell, as in figure 2.2 the electric field on axis perceived by emitted electrons can be assumed as

$$E_z = E_0 \cos kz \sin(\omega t + \phi_0) \quad (2.2)$$

where E_0 is the peak field, $k = 2\pi/\lambda$ with λ the RF wavelength, c is the speed of the light, $\omega = ck$ and ϕ_0 is the starting RF phase perceived by the emitted electrons at $z = 0$ and $t = 0$.

It is convenient to introduce the following quantity ϕ

$$\phi = \omega t - kz + \phi_0 = k \int_0^z \left(\frac{\gamma}{\sqrt{\gamma^2 - 1}} - 1 \right) dz + \phi_0 \quad (2.3)$$

being γ the relativistic factor and where

$$\frac{\gamma}{\sqrt{\gamma^2 - 1}} = \frac{1}{\beta} = \left(\frac{1}{c} \frac{dz}{dt} \right)^{-1}. \quad (2.4)$$

The RF acceleration generates a γ variation given by:

$$\frac{d\gamma}{dz} = \frac{eE_0}{2mc^2} [\sin\phi + \sin(\phi + 2kz)] \quad (2.5)$$

The RF acceleration in the cavity is determined by equations 2.3 and 2.5. We assume that electrons leave the cathode with no kinetic energy, so that $\gamma = 1$ at $z = 0$. The equations 2.3 and 2.5 in a linac can be solved by neglecting the the second term in equation 2.5, that represents the backward-propagating wave (see Ref. [18]). Such approximation unfortunately is valid for electrons in long linac, where the effect of the reflected wave averages to zero.

To obtain an approximation of equation 2.5, we note that the quantity in the integral of equation 2.3 is significantly different from zero only near the cathode, where the emitted electrons are not yet relativistic and so the equation 2.5 can be approximated as

$$\frac{d\gamma}{dz} \approx \frac{eE_0}{2mc^2} \sin\phi_0 \quad (2.6)$$

in the cathode region.

Introducing the normalized vector potential α i.e. a dimensionless parameter that describes the accelerating strength of the RF field

$$\alpha = \frac{eE_0}{2mc^2k} \quad (2.7)$$

it is possible to express the relativistic factor depending on the injection phase ϕ_0 and the longitudinal position z as

$$\tilde{\gamma} = 1 + 2\alpha \sin\phi_0 kz. \quad (2.8)$$

In order to express the evolution of the phase ϕ during acceleration we can use approximation 2.6 in the equation 2.3 obtaining

$$\phi = \frac{1}{2\alpha \sin\phi_0} \left[\sqrt{\tilde{\gamma}^2 - 1} - (\tilde{\gamma} - 1) \right] + \phi_0. \quad (2.9)$$

It is possible to extract a proper γ solution during acceleration integrating the equation 2.5, using the phase approximation 2.9 and obtaining

$$\gamma = 1 + \alpha \left[kz \sin\phi + \frac{1}{2} (\cos\phi - \cos(\phi + 2kz)) \right]. \quad (2.10)$$

As shown by simulation results in Ref. [18] the approximated solutions 2.9 and 2.10 for γ and ϕ are in good agreement with the exact evolution into the RF cavity for γ

and only for a not too small ϕ_0 .

From the equation 2.9, we see that the phase ϕ has the asymptotic value ϕ_∞ that is

$$\phi_\infty = \frac{1}{2\alpha \sin\phi_0} + \phi_0. \quad (2.11)$$

As we will see in the next section the RF field contribution to the transverse emittance is minimized when ϕ_∞ is $\pi/2$, i.e. when the bunch exit from the RF cells on the wave crest.

From these considerations in order to minimize the transverse emittance value at the gun exit, the beam injection phase ϕ_0 has to be chosen such that

$$\left(\frac{\pi}{2} - \phi_0\right) \sin\phi_0 = \frac{1}{2\alpha} = \frac{eE_0}{2mc^2 \frac{2\pi}{\lambda}}. \quad (2.12)$$

After the study of the acceleration process inside the RF gun we want to evaluate the effects on the longitudinal phase space distribution introducing the longitudinal emittance. The spread in the phase $\Delta\phi$ is related to the spread of the longitudinal position by $\Delta\phi = -k\Delta z$, so that particles with positive $\Delta\phi$ are located in the trailing part of the electron bunch relative to those with negative $\Delta\phi$. In order to evaluate the longitudinal effect is convenient to refer at the longitudinal phase space defined by (z, p_z) , where p_z is the normalized dimensionless longitudinal momentum defined by $p_z = \beta\gamma$. For relativistic beams ($\beta \approx 1$) the longitudinal momentum can be approximated as $p_z \approx \gamma$.

Using the equation 2.11, the bunch compression factor can be evaluated as

$$\frac{\Delta\phi_\infty}{\Delta\phi_0} = 1 - \frac{\cos\phi_0}{2\alpha \sin^2\phi_0}. \quad (2.13)$$

From which bunches in general are longitudinally compressed during the RF acceleration process in the gun.

Considering the first half cell to estimate the distortion of the longitudinal phase space due to the RF field, we can consider the phase space distribution at the end of $(n + 1/2)th$ cavity that corresponds to a longitudinal position $z = (2n + 1)\lambda/4$. Using the approximated solution 2.10 for γ , at the end of the $(n + 1/2)th$ cavity we have

$$\gamma = 1 + \alpha[(n + 1/2)\pi \sin\phi + \cos\phi]. \quad (2.14)$$

Using the phase value at the extraction that minimizes the emittance $\phi = \pi/2$, the cosine term goes to 0. The first sine term gives rise to a characteristic final phase space distortion that looks like a rotated comma.

As in Ref. [18], the longitudinal emittance definition can be obtained projecting the

6 - D emittance in the longitudinal coordinates

$$\epsilon_z = \sqrt{\langle(\Delta p_z)^2\rangle\langle(\Delta z)^2\rangle - \langle(\Delta p_z)\Delta z\rangle^2} = \frac{1}{k} \sqrt{\langle(\Delta p_z)^2\rangle\langle(\Delta\phi)^2\rangle - \langle(\Delta p_z)\Delta\phi\rangle^2} \quad (2.15)$$

where $\langle p_z \rangle$ and $\langle z \rangle$ are the average values for p_z and z such that along the bunch $p_z = \langle p_z \rangle + \Delta p_z$ and $z = \langle z \rangle + \Delta z$

Assuming the electrons are relativistic at the end of the $(n + 1/2)$ th cavity, $p_z \approx \gamma$ and using equation 2.14 we obtain

$$\langle \gamma \rangle + \Delta\gamma = 1 + \alpha[(n + 1/2)\pi \sin(\langle \phi \rangle + \Delta\phi) + \cos(\langle \phi \rangle + \Delta\phi)]. \quad (2.16)$$

In order to minimize the emittance at the gun exit we can set $\langle \phi \rangle = \pi/2$. Expanding up to third term the previous equation 2.16 and considering γ_f the value of $\langle \gamma_f \rangle$ at the RF structure exit

$$\Delta\gamma = -\alpha\Delta\phi - \frac{1}{2}(\gamma_f - 1)(\Delta\phi)^2 + \frac{\alpha}{3!}(\Delta\phi)^3 + \dots \quad (2.17)$$

We can define for $\Delta\gamma$ and $\Delta\phi$ the rms quantities

$$\sigma_{\Delta\gamma} = \langle(\Delta\gamma)^2\rangle^{\frac{1}{2}} \quad \text{and} \quad \sigma_\phi = k\sigma_z = \langle(\Delta\phi)^2\rangle^{\frac{1}{2}} \quad (2.18)$$

and so from equation 2.17 the linear relations between the rms energy spread and the rms bunch length

$$\sigma_{\Delta\gamma} = \alpha\sigma_\phi = \alpha k\sigma_z. \quad (2.19)$$

Using the $\Delta\gamma$ expansion 2.17 in the longitudinal emittance definition 2.15, it is possible to obtain an expression for the longitudinal emittance contribution due to the time variation of the RF field

$$\epsilon_z^{RF} = \frac{1}{k}(\gamma_f - 1)\sqrt{\langle(\Delta\phi)^4\rangle\langle(\Delta\phi)^2\rangle} \quad (2.20)$$

that for a gaussian bunch distribution becomes

$$\epsilon_z^{RF} = \sqrt{3}(\gamma_f - 1)k^2\sigma_z^3. \quad (2.21)$$

2.3 RF acceleration effects in the transverse phase space

Now we take into account the RF acceleration effects in transverse dynamics using the Maxwell's equations. We will consider that the transverse momentum is impressed to the electrons only in the region at the cavity exit i.e. the RF accelerating field does not modify the electron transverse coordinates. At the cavity exit due to time variation of the RF field, transverse kicks at different longitudinal bunch positions are impressed.

Assuming that longitudinal electric field does not depend by the transverse coordinate r and by the angle θ , but is only a function of the longitudinal position z and time t i.e. $E_z = E_z(z, t)$. Using the Maxwell's equations we can obtain the radial electric field E_r and the angular magnetic field B_θ as

$$E_r = -\frac{r}{2} \frac{\partial}{\partial z} E_z \quad (2.22)$$

and

$$cB_\theta = \frac{r}{2c} \frac{\partial}{\partial t} E_z. \quad (2.23)$$

From these equations it is possible to extract the radial force acting on an electron of the beam as

$$F_r = e(E_r - \beta c B_\theta). \quad (2.24)$$

Considering p_r as the dimensionless radial momentum

$$p_r = \gamma \frac{1}{c} \frac{dr}{dt} \quad (2.25)$$

then the radial motion is well described by the equation

$$\frac{dp_r}{dt} = \frac{1}{mc} F_r. \quad (2.26)$$

Considering in the equation 2.24 a radial force F_r that derives from an expression of the electric field of the type

$$E_z = E(z) \cos kz \sin(\omega t + \phi_0) \quad (2.27)$$

and considering that the net transfer momentum to the electrons comes only when the particles cross the boundary between the cavity and the field free region, i.e the cavity exit, from the integration of equation 2.26 we obtain

$$p_r = \alpha k r \sin \phi \quad (2.28)$$

2.3. RF ACCELERATION EFFECTS IN THE TRANSVERSE PHASE SPACE 37

where ϕ is the RF phase at the gun exit. The equation 2.28 represents the transverse momentum transferred to the electrons and in cartesian coordinates it becomes

$$p_x = \beta\gamma x' = (\alpha k \sin\phi)x \quad (2.29)$$

where $x' = \frac{dx}{dz}$. From equation 2.29 for each phase ϕ there is a line with a different slope in the phase space (x, x') .

Referring to the normalized rms emittance $\epsilon_{n,rms}$ defined in equation 1.16 and considering equation 2.29 it is possible to introduce the RF transverse emittance contribution as

$$\epsilon_x^{RF} = \alpha k \langle x^2 \rangle \sqrt{\langle \sin^2\phi \rangle - \langle \sin\phi \rangle^2}. \quad (2.30)$$

Writing the phase as the sum of $\phi = \langle \phi \rangle + \Delta\phi$, with a small symmetrically distributed $\Delta\phi$ we obtain

$$\epsilon_x^{RF} = \alpha k \langle x^2 \rangle \sqrt{\left[\langle (\Delta\phi)^2 \rangle^2 - \frac{1}{3} \langle (\Delta\phi)^4 \rangle \right] \cos^2 \langle \phi \rangle + \frac{1}{4} [\langle (\Delta\phi)^4 \rangle - \langle (\Delta\phi)^2 \rangle^2] \sin^2 \langle \phi \rangle}. \quad (2.31)$$

The last equation for the emittance has a minimum for $\langle \phi \rangle = \pi/2$ i.e. when the beam exits from the accelerating structure on the RF wave crest. In that case the emittance is reduced to

$$\epsilon_x^{RF} = \alpha k \frac{\langle x^2 \rangle}{2} \sqrt{[\langle (\Delta\phi)^2 \rangle - \langle (\Delta\phi)^2 \rangle^2]} \quad (2.32)$$

that becomes for a gaussian bunch distribution

$$\epsilon_x^{RF} = \frac{\alpha k \langle x^2 \rangle \sigma_\phi^2}{\sqrt{2}} = \frac{\alpha k^3 \sigma_x^2 \sigma_z^2}{\sqrt{2}}. \quad (2.33)$$

The equation 2.33 shows that the RF emittance strongly depends by the transverse and longitudinal beam dimensions and increase with increasing both gradient and RF frequency. The equation 2.33 considers an instantaneous emittance growth i.e. it does not take into account the bunch's radial expansion due to the space charge forces, but well demonstrates the emittance scaling to the beam size.

It is fundamental to observe that extracting the beam on the emittance minimum condition $\langle \phi \rangle = \pi/2$, the transverse momentum p_r impressed to the bunch particles described by the equations 2.28 and 2.29 is maximum. In that case the rms angular beam divergence $\sigma_{x'}$ defined in the equation 1.13 is

$$\sigma_{x'} = \frac{\alpha}{\gamma} k \sigma_x \quad (2.34)$$

In order to minimize the emittance and at the same time take under control the beam divergence it is fundamental to focus the beam immediately after leaving the RF cavity. As we will discuss in the next sections, to do that a time independent linear force from a solenoid around the gun RF cavities is used.

2.4 Emittance growth due to the space charge forces

As we have seen in the Chapter 1, one of the space charge effects in the bunch evolution are longitudinal correlations inside the bunch that lead to consider a correlated emittance that cause an emittance growth. The region where the space charge forces have more effect is the area near the cathode, where the electrons are not yet relativistic and the fifth term of the envelope equation 1.22 is not negligible. An analytical expression for the space charge emittance growth have been derived by Kim in Ref. [18], considering all electrons move with the same velocity along the z axis, so that the space charge forces is purely electrostatic in the electrons reference frame and the bunch length is elongated by a factor γ .

In the calculation the space charge force effects on the momentum are weighted by a factor $1/(\gamma^2\beta)$, so that they are relevant where the electrons are not relativistic i.e. only in the first part of the RF gun. Considering a cylindrically symmetric charge distribution inside the bunch and calculating the momentum contribution due to the space charge field, it is possible to obtain an expression for the longitudinal and transverse space charge emittances as

$$\epsilon_i^{sc} = \frac{\pi}{4} \frac{1}{\alpha k} \frac{1}{\sin\phi_0} \frac{I}{I_A} \mu_i(A) \quad (2.35)$$

where $I_A = 17\text{kA}$ is the Alfvén current, I is the bunch peak current, and μ_i are dimensionless functions that distinguish the transverse ($\mu_i = \mu_x$) and longitudinal ($\mu_i = \mu_z$) space charge emittances and are defined as

$$\mu_x(A) = \sqrt{\langle \xi_x^2 \rangle \langle x^2 \rangle - \langle \xi_x x \rangle^2} \quad (2.36)$$

$$\mu_z(A) = \sqrt{\langle \xi_z^2 \rangle \langle \Delta z^2 \rangle - \langle \xi_z \Delta z \rangle^2} \quad (2.37)$$

where $A = \sigma_x/\sigma_z$ is the bunch aspect ratio and ξ is the normalized space charge field, that is proportional to the electrostatic space charge field E_{sc} and is defined as

$$\xi = \frac{4\pi\epsilon_0}{n_0} E_{sc}. \quad (2.38)$$

For example, as treated also in Ref [17], considering a beam with $\sigma_z \gg \sigma_x$ so that the bunch aspect ratio $A \rightarrow 1$ and $\mu_x \approx O(1)$, the analytical expression for the space charge induced emittance growth becomes

$$\epsilon_{n,x}^{sc} \approx \frac{AQ}{8\sqrt{2\pi}\epsilon_0 c \sigma_x E_0 \sin\phi_0} \mu_x(A) \quad (2.39)$$

where E_0 is the maximum electric field at the cathode surface, and ϕ_0 is the RF extraction phase.

Considering the transverse emittance growth due to the space charge forces, along a drift distance Δz , the emittance appears to be proportional to the bunch current and the drift distance and inversely proportional to the beam energy (Ref. [19] and [20])

$$\epsilon_{n,x}^{sc} \propto \frac{I\Delta z}{\gamma^2\beta^2}. \quad (2.40)$$

The inverse scaling with the beam energy in the equation 2.40 indicates that is desirable to accelerate the bunch very quickly after the electrons emission from the cathode surface. From these reasons photocathode within RF accelerating cavities have been developed.

Space charge effects as the emittance growth and as seen also in the previous chapter the space charge term of the envelope equation 1.22, in general are negligible for high energy beams.

In general the equations for the emittance growth from space charge and RF fields can be used to determine the starting beam parameters that minimize the emittance for a given charge.

2.5 Emittance compensation in photoinjectors for high brightness beams

After the invention of the RF photo-gun, the emittance compensation scheme of a correlated emittance contribution was proposed by Carlsten [16] with the use of a solenoid. Here the emittance growth was identified to be in the variation of the transversely defocusing space charge force with the longitudinal position within the bunch. Considering the bunch made by longitudinal slices, Carlsten argued the emittance compensation considering the transverse phase space. In fact considering this phase space during a drift the longitudinal slices, due to the varying space charge force, expand and emittance increase and it is reduced after a focusing lens. This emittance evolution can be found in simulations (see. Ref. [21]) and was experimentally demonstrated (see Ref. [22]), showing an emittance maximum coinciding with the maximum beam size and two emittance minima near the minimum spot size.

In the Carlsten's model the compensation process happen during the drift, in the Serafini-Rosenzweig's model (see Ref. [23]) the emittance compensation starts in the focusing channel. We have introduced in the previous chapter the Brillouin flow in a focusing channel (eq. 1.28) as a stationary solution in which the inner space charge forces are completely balanced by the external focusing. Considering the bunch made by different slices a small perturbation around the Brillouin flow leads to an oscillation of the beam envelope as shown in Figure 2.3.

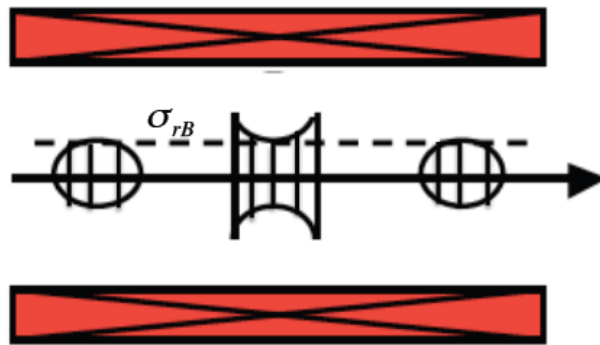


Figure 2.3. When a beam, or same beam slice, has a perturbation respect to the Brillouin flow $\sigma_{r,B}$ the focusing channel generates in the bunch, or in the mismatched slice, beam envelope oscillations.

As we have seen in the previous chapter the period length of the oscillation depends by the strength of the external force, so that also a periodic emittance oscillation appear.

Now it is shortly presented the Carlsten emittance compensation model. Reconnecting with the discussed invariant envelope, we discuss also the Serafini-Rosenzweig invariant envelope model, showing that is a bunch propagation mode able to damp the correlated emittance, providing emittance compensation canceling the space charge effects.

2.5.1 Space charge induced emittance compensation

There are many effects that contribute to the final transverse emittance like constructions tolerances or errors and operation errors. These effects include beam transverse offsets leading to transverse wakefields, accelerating cavities offsets and rotated quadrupole magnets. These effects are typically uncorrelated and we can take them into account adding them in quadrature.

The emittance growth contributions from the space charge forces and RF accelerating field are typical in an accelerated electron beam and do not come from misalignments or other errors.

The idea of an emittance compensation scheme in a photoinjector was firstly proposed by Carlsten Ref. [16]. This scheme minimizes the final emittance $\epsilon_{n,rms}$ at the end of the beam line, vanishing the space charge effects on the transverse emittance. This decrease in the rms normalized emittance $\epsilon_{n,rms}$ does not violate the Liouville's theorem, but take advantage from correlations in the beam phase space.

Emittance compensation is based on the assumption that after the photocathode and before electrons became relativistic there is a large emittance growth, as described in the previous sections, due to both space charge forces and RF accelerating fields. Consider an electron bunch with a smooth longitudinal charge distribution peaked at the bunch center and that is zero at the ends of the bunch and with a uniform radial distribution. If the beam is long enough that the resulting electric field inside the bunch is essentially radial, the resulting emittance comes from its correlated transverse phase space that looks like a rotated bow tie as in Figure 2.4.

A single axial bunch slice can be represented by a line in the transverse phase space such that the emittance of each slice is zero. If we integrate all the axial slices in transverse phase space we obtain the bunch transverse rms emittance.

The emittance will vanish if we differentially rotate the phase space lines corresponding to the different axial beam slices, so that they all stand at the same angle. This mechanism does not violate the Liouville's theorem because we are considering only a 2-D projection of the phase space, while the 6-D phase space density remains constant.

From these considerations the Carlsten idea was to introduce a lens after the electrons emission, taking advantage from the phase space correlations. Concretely the idea

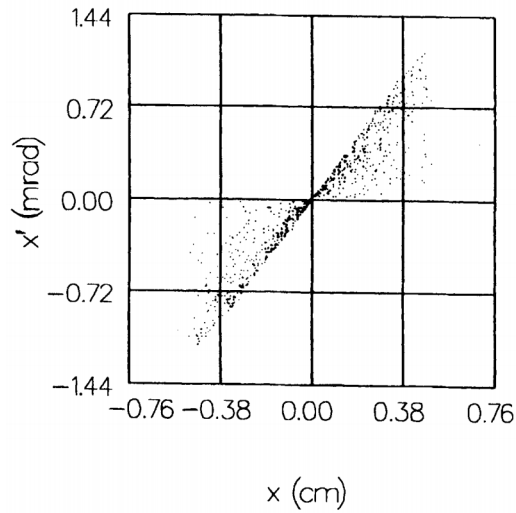


Figure 2.4. Typical correlated bunch phase space after a drift. From Ref. [19]

was to introduce a solenoid magnet after the first acceleration stage, so that a linear force acts on the beam.

Taking into account two particles on the edge of the bunch, one in the central axial edge and the second one on the axial end of the bunch (as shown in Figure 2.5), the compensation technique is well represented in Figure 2.6.

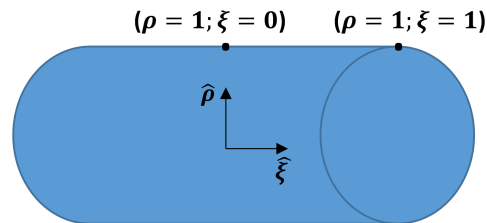


Figure 2.5. In order to demonstrate the emittance compensation we take into account two particles on the bunch edge. We study the evolution of their orbits in phase space, before and after the solenoid magnet.

The curved lines with arrows represent the particle orbits in the phase space, while the straight lines delimit the blue phase space region occupied by the beam that is proportional to the total beam emittance. The particles drift to the lens Figure 2.6-a. The bow tie is formed by longitudinal correlations. The solenoid is a lens that rotate the distribution Figure 2.6-b. Particle orbits evolve due to longitudinal nonlinearities in the drift after the solenoid and their phase space area shrink to zero Figure 2.6-c. Considering all slices after the solenoid, they rotate to the same angle at the same drift distance, so that the space charge emittance growth before the lens is well compensated.

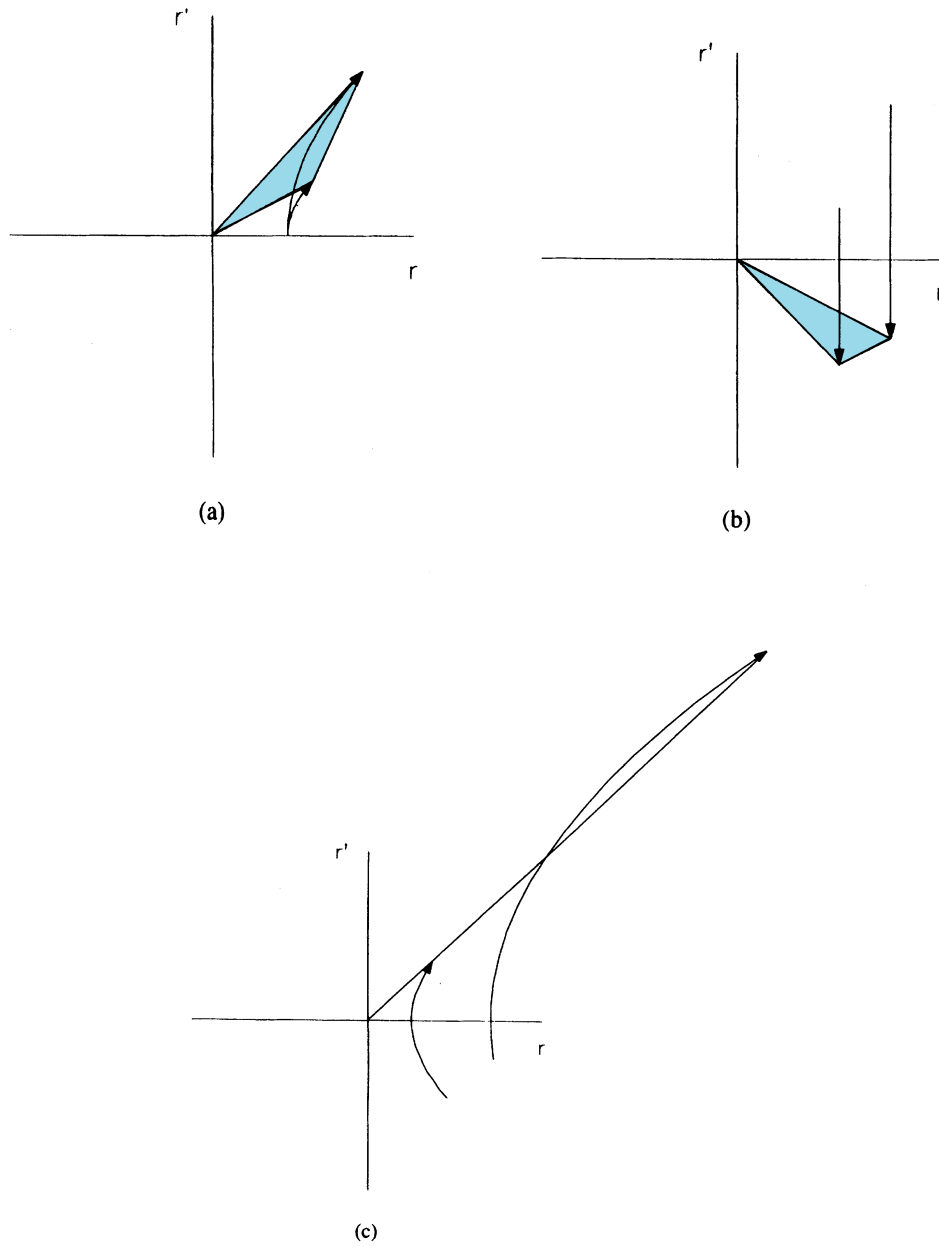


Figure 2.6. Phase space orbits evolution considering two particles on the bunch edge that after a drift (fig.a) they reach the lens (fig.b) and drift after the lens where the bow tie collapses on a line (fig.c) and the phase space area shrink to zero. From Ref. [19]

A simplified analytical model of the emittance compensation in Ref. [19] assumes that the inner space charge forces do not vary with time i.e. they are independent on the bunch position z along the beam line. The radial space charge force in a bunch is a function of the longitudinal position ζ and of the radial position ρ within the bunch, where $\rho = 1$ and $\zeta = \pm 1$ define respectively the radial edge and the bunch ends. We can write the normalized space charge force, that is proportional to the inner radial electric field and inversely proportional to γ^3

$$\Lambda(\rho, \zeta) = \frac{eE_r(\rho, \zeta)}{m\gamma^3\beta^2c^2} \quad (2.41)$$

where E_r is the radial electric field in the laboratory frame. Positioning a lens in the position $z = z_l$ with a focal length of

$$f = \frac{z_d^2}{2(z_l + z_d)} \quad (2.42)$$

where z_d is a position further downstream the lens.

After a drift z_d , from the lens position z_l , the ratio of the beam divergence to the radius is not a function of the space charge forces Λ or of the bunch internal coordinate ζ

$$\frac{r'(\rho, \zeta)}{r(\rho, \zeta)} = \frac{2(z_l + z_d)}{z_d(z_d + 2z_l)}. \quad (2.43)$$

This means that after a drift z_d from the lens the emittance growth has been reduced to zero because in phase space all points lie along a line at the same orientation.

As in Ref. [19], with an initial nondivergent beam of radius r_0 the space charge normalized emittance can be written as a function of the axial bunch position z_d and focal length f

$$\epsilon_{x,n}^{sc} = \frac{1}{2}\beta\gamma\sqrt{\langle\Lambda^2\rangle\langle\rho^2\rangle - \langle\Lambda\rho\rangle^2} \left(2r_0(z_l + z_d) - \frac{z_d^2 r_0}{f} \right). \quad (2.44)$$

This formula shows that the space charge emittance can vanish for arbitrary lens positions and drift distances, with the proper choice of the lens focal length f . After the emittance minimum the quadratic term in parenthesis leads to a rapid nonlinear emittance growth.

In a less simplified model we can assume that the space charge forces are time dependent along the beam propagation i.e. they vary in different z positions $\Lambda(\rho, \zeta, z)$, and also that the forces are radially linear in a sufficiently long beam. Considering only the constant linear terms in a Taylor expansion of the radial space charge forces it is possible to demonstrate (see Ref. [19]) a complete emittance compensation for a beam that exit from a lens and drift for a proper distance z_d .

This means that any nonlinear axial or radial contribution to the space charge forces is not canceled by this compensation.

From these considerations the emittance compensation works over an axial section of the beam where we can represent the radial space charge forces using a linear expansion. This is the case of a laminar beam i.e. the laminarity parameter ρ , defined in the equation 1.23, has to be much greater than one ($\rho \gg 1$). If the beam becomes non laminar the axial bunch length that can be compensated becomes very short. From these considerations the residual emittance is minimized if the beam laminarity is maximized.

The emittance compensation technique using an external solenoid after the gun accelerating cavities, is a well established technique thanks to which it is possible to generate high brightness beams.

There was also another interesting proposal (see Ref.[24]) to recover the minimum emittance for a bunch that is not injected in the optimum phase $\langle\phi\rangle = 90^\circ$. As we have seen in the previous sections the transverse emittance is minimized if the extracting phase is $\pi/2$, but this phase value is far from the minimum longitudinal emittance condition. So it is possible to inject the bunch in a RF phase that is optimized for the longitudinal emittance and after modify the transverse phase space using a second corrective cell. The correction can be made using an unsymmetrical cell downstream the gun accelerating cells and it is able to recover the minimum transverse emittance value.

2.5.2 Invariant envelope and double emittance minimum

After the advent of the emittance compensation scheme introduced by Carlsten, there were some other important discoveries that led to improve the emittance compensation scheme. In fact the Carlsten' description, explain the emittance compensation up to the emittance minimum before the accelerating structure where the beam is space charge dominated and the emittance continues its evolution. The Serafini-Rosenzweig (see Ref. [23]) description of the emittance compensation process considers the gun and linac section joined and calculating the beam matching conditions with the accelerating structure, in order to match the beam spot size reducing the beam normalized rms emittance.

After the emission the beam is space charge dominated, and it undergoes a strong acceleration and a subsequently fast transition from a non relativistic to a relativistic regime where the collective plasma effects are strongly diminished. Despite this plasma oscillations are still present in transverse plane and they cause emittance growth and distortions in the transverse phase space.

Serafini and Rosenzweig have shown that in a quasi laminar regime i.e. a space

charge dominated regime in which the effects of thermal emittance can be neglected, a mismatch between space charge forces and the external RF focusing field produces a slice envelope oscillations called plasma oscillations. These oscillations as we have seen also in the previous chapter, generate correlated emittance oscillations.

In order to damp these oscillations, balancing internal and external bunch forces, Serafini and Rosenzweig used the rms envelope equation 1.22, including the effects of linear space charge forces and of an external focusing provided by RF, acceleration and adiabatic damping in order to find an envelope analytical solution called invariant envelope

$$\sigma_{inv} = \frac{2}{\gamma'} \sqrt{\frac{I}{3I_A\gamma}} \quad (2.45)$$

where $I_A = 17kA$ is the Alfvén current and $\gamma' = \frac{eE_{acc}}{m_e c^2} \approx 2E_{acc}$ where E_{acc} is the RF accelerating field.

This solution has a plasma frequency $k_p = \sqrt{3/2}\gamma'/\gamma$ that is proportional to the RF focusing frequency, and it ensures that all slices evolve in transverse phase space with the same angle δ that does not depend by the beam current. As we have seen in the previous section the emittance growth from linear space charge forces is due to an angular spread of the slices in the bunch phase space.

In order to dump the plasma and emittance oscillations, the beam after the gun has to be injected into an accelerating section in its envelope waist ($\sigma' = 0$). It is also fundamental that the RF accelerating gradient has to be matched to the transverse beam size σ_x , to the bunch energy γ and to the peak current I according to the equation 2.45 we obtain

$$\gamma' = \frac{2}{\sigma_x} \sqrt{\frac{I}{3I_A\gamma}} \quad (2.46)$$

for a SW accelerating structure.

For a TW structure the matching condition for the accelerating gradient (see Ref. [21]) is

$$\gamma' = \frac{2}{\sigma_x} \sqrt{\frac{I}{2I_A\gamma}}. \quad (2.47)$$

These matching conditions preserve the beam laminarity and ensure a damping of the emittance and of the plasma oscillations during the beam acceleration inside the energy booster.

As these oscillations have an oscillation phase, the final emittance value depends by the plasma oscillation phase at the beam injection into the energy booster.

Ferrario discovered (see Ref. [21]) that using a proper injection phase it is possible to perform an emittance compensation that in principle reach the minimum emittance

value at the linac end. The Ferrario working point take advantage from the invariant

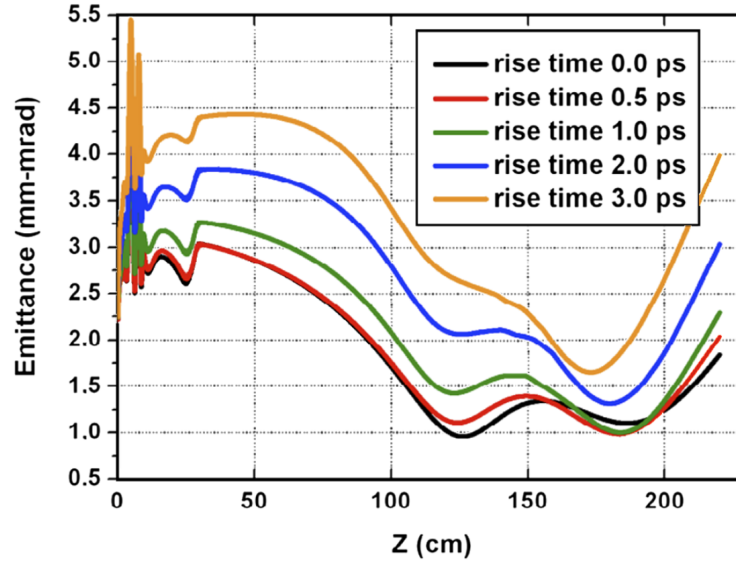


Figure 2.7. Normalized rms emittance oscillations in the drift after the RF gun and solenoid computed by Parmela. It is visible the double emittance minimum that collapse to one minimum if the beam rise time encreases. From Ref. [22]

envelope 2.45 and he found a working point optimized for a flat top beam that shows the so called double emittance minimum before the booster with only one relative maximum.

Simultaneously matching beam envelope and RF accelerating gradient into the accelerating structures respectively to the equation 2.45 and 2.47, the beam is injected in a plasma phase that corresponds to the relative maximum of the emittance. In this way the beam laminarity and emittance oscillations damping are satisfied while space charge forces are also damped too during acceleration.

Using this emittance compensation scheme, the emittance asymptotically decreases and the emittance minimum is reached at high beam energy. The double emittance minimum was found during the LCLS design and was directly measured at SPARC_LAB (see Ref. [22]).

It is interesting to observe that the double minimum is generated by beating between head and tail plasma frequencies caused by correlated chromatic effects in the solenoid. In fact the beam double emittance is clearly visible for a flat top beam, while it tends to collapse in only one minimum if the beam rise time increases, up to reach a gaussian beam (see Figure 2.7). Using a gaussian beam this effect is weaker since the slice current in the head and in the tail is vanishing.

If the beam is properly focused after the RF gun by a solenoid and during the acceleration, beam spot size and RF accelerating gradient are properly matched

and also the booster start is located in correspondence of the relative maximum of the emittance, then the emittance is well compensated and it decreases during the acceleration process as shown in Figure 2.8 for different rise times.

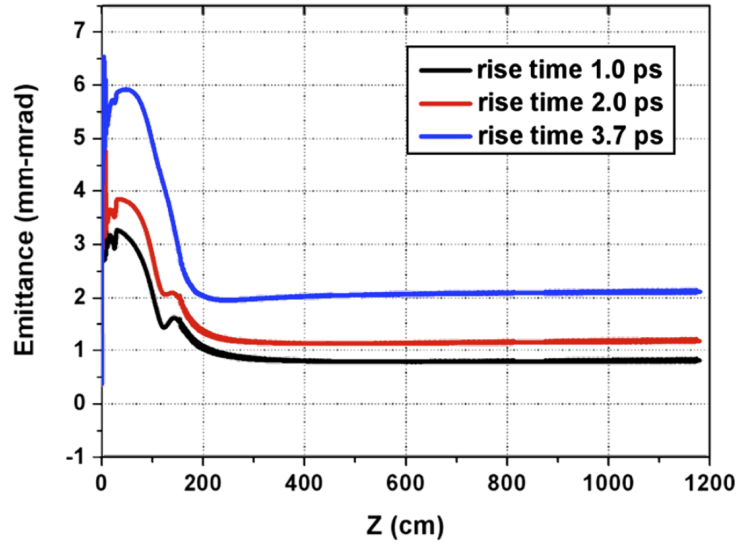


Figure 2.8. Normalized rms emittance damping along the energy booster as computed by Parmela. The first accelerating structure starts at $z = 1.5\text{m}$. From Ref. [22]

2.6 Particle emission from the cathode

As we have seen in the previous section the quality of an accelerated electron beam arises from a perfect control and matching of the beam parameters in the first part of the photoinjector where the beam is not yet relativistic. Another fundamental process to have a good quality beam in terms of emittance is the electrons photoemission from the cathode.

The transition from bounded electrons in the copper and free electrons is a strong process that requires an amount of external energy. In fact the electron density after emission is reduced in very short time by eight to nine order of magnitude (see Ref. [25]). The density of conduction band for metals is $n_e \approx 10^{22} - 10^{23} \text{electrons/cm}^3$, while in a cylindrical bunch of 6 ps long, 1 nC charge and a spot $200\mu\text{m}$ the electron density is $n_e \approx 1.1 \times 10^{14} \text{electrons/cm}^3$.

The thermal energy of the electrons inside the cathode is very low, in copper near the Fermi energy is 0.02eV at room temperature ($T = 300\text{K}$). The thermal energy as we will see is proportional to the transverse energy spread, so the electron emission energy define the lower limit of the beam emittance. This emittance lower limit is called thermal emittance if we refer to thermionic emission, but this concept can be extended to the other fundamental emission processes as photoelectric effect and field emission.

Electrons as fermions obey to the Fermi-Dirac distribution, so that the distribution of the occupied states is defined by

$$f_{FD} = \frac{1}{1 + e^{\frac{E-E_f}{k_B T}}} \quad (2.48)$$

where E_f is the Fermi energy, i.e. the energy of the higher level occupied by a fermionic system at zero Kelvin.

At high energies the tail of the Fermi-Dirac distribution has the same tail of the classical Maxwell-Boltzmann distribution

$$f_{MB} = e^{\frac{-E}{k_B T}}. \quad (2.49)$$

During the thermionic emission the cathode is heated to very high temperatures in order to promote emission from the high energy tail of the distribution. Photoelectric effect and field emission involve the excitation of electrons from below the Fermi energy and not only from the tail of the distribution.

In this analysis we refer to electronic emission from metallic cathode in which can be used the free electron gas model, emission from a semi conductor cathode has another treatment that will not be treated.

In order to understand the emission processes we can introduce the electric potential energy that is the sum of different effects near the cathode surface and it is given by

$$e\Phi = e\phi_{work} - \frac{e^2}{16\pi\epsilon_0 x} - eE_0x \quad (2.50)$$

where ϕ_{work} is the work function, the second term represents the image charge potential and the third term is due to the contribution of the applied electric field E_0 . Electrons can escape if their energies are higher than the barrier i.e. for energies greater than the work function they can tunnel the barrier with a probability different from zero. In the photo-emission and thermionic-emission processes we give energy to the electrons and they exceed the barrier and escape, in the field emission process the barrier is diminished by the external RF field and electrons can tunnel easily the barrier. So the effect of the applied field is to diminish the barrier, this phenomena is known as Schottky effect.

2.6.1 Thermionic emission

In order to escape an electron needs to have enough kinetic energy in the direction of the barrier to escape

$$\frac{mv_x^2}{2} > e\phi_{work} \quad (2.51)$$

it means that the escaping velocity has to be

$$v_x > \sqrt{\frac{2e\phi_{work}}{m}}. \quad (2.52)$$

In the thermionic emission it can be reached heating the cathode to an high temperature T and obtaining a thermionic current density (see Ref.[25])

$$j_{thermionic} = 2n_0e \left(\frac{2k_B T}{m} \right)^2 e^{-\frac{\phi_{work}}{k_B T}} = A\lambda_r T^2 e^{-\frac{\phi_{work}}{k_B T}} \quad (2.53)$$

where λ_r take into account that the electrons can be described as a wave so there is a probability to be reflected in the transition between the material and vacuum. So we can express $\lambda_r = (1 - r)$ where r is the proportion of reflected current. A is a universal constant equal to

$$A = \frac{-em}{2\pi^2\hbar^3} = 120 \frac{A}{cm^2 K}. \quad (2.54)$$

The equation 2.53 shows how thermionic current rises rapidly with temperature and with decreasing work function.

From Maxwell-Boltzmann distribution it is possible to obtain the velocity distribution

for the emitted electrons. In Figure 2.9 there is the energy distribution for electrons that obey Maxwell-Boltzmann statistics.

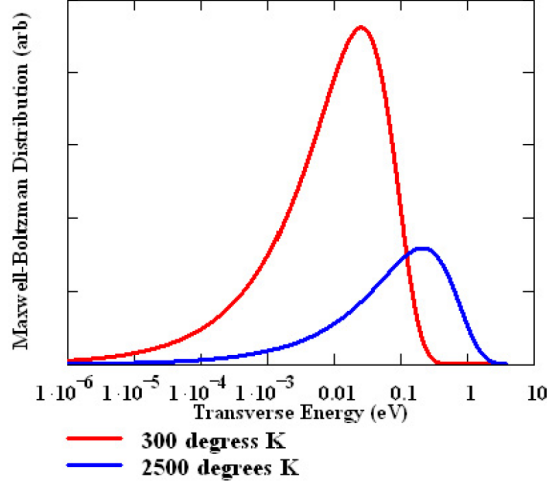


Figure 2.9. Maxwell Boltzmann electron energy distributions for two different temperatures 300K and 2500K. From Ref. [25]

If we calculate the emittance very near the cathode surface where the electrons flow is laminar, in that region the correlations between position and angle can be ignored and the normalized emittance can be written as

$$\epsilon_n = \beta\gamma\sigma_x\sigma_{x'} \quad (2.55)$$

where the rms divergence term can be expressed as

$$\sigma_{x',rms} = \frac{\langle p_x \rangle}{p_{total}} = \frac{1}{\beta\gamma} \frac{\sqrt{\langle v_x^2 \rangle}}{c} \quad (2.56)$$

so that the normalized emittance becomes

$$\epsilon_{n,rms} = \sigma_{x,rms} \frac{\sqrt{\langle v_x^2 \rangle}}{c}. \quad (2.57)$$

Considering the mean squared transverse velocity for a Maxwell velocity distribution

$$\langle v_x^2 \rangle = \frac{k_B T}{m} \quad (2.58)$$

that finally leads to the thermionic emittance of a Maxwell-Boltzmann distribution at temperature T, is

$$\epsilon_{n,rms} = \sigma_{x,rms} \sqrt{\frac{k_B T}{m c^2}}. \quad (2.59)$$

2.6.2 Photoelectric emission

As we have seen in the previous chapter photoelectric effect is a key point in an RF photoinjector. In this section we study the photoelectric emission from cathode and the fundamental quantities of this process. We want also calculate the photoelectric cathode emittance ϵ_{photo} and the Quantum Efficiency (QE) defined with respect to the incident laser energy

$$QE = \frac{n_e}{n_\gamma} = \frac{h\nu(eV)}{E_{laser}(Joule)} Q(C). \quad (2.60)$$

Where $h\nu$ is the photon energy, Q is the charge extracted by the laser and E_{laser} is the energy carried by the incident laser.

In order to better understand how photoelectric effect works inside the gun is useful to introduce the Spicer's three step model (see Figure 2.10) described and discussed in Ref. [25, 26, 27]. The first step is the photon absorption by the electron, then the electron is transported up to the cathode surface and if the energy is enough to overcome the barrier the electron can escape.

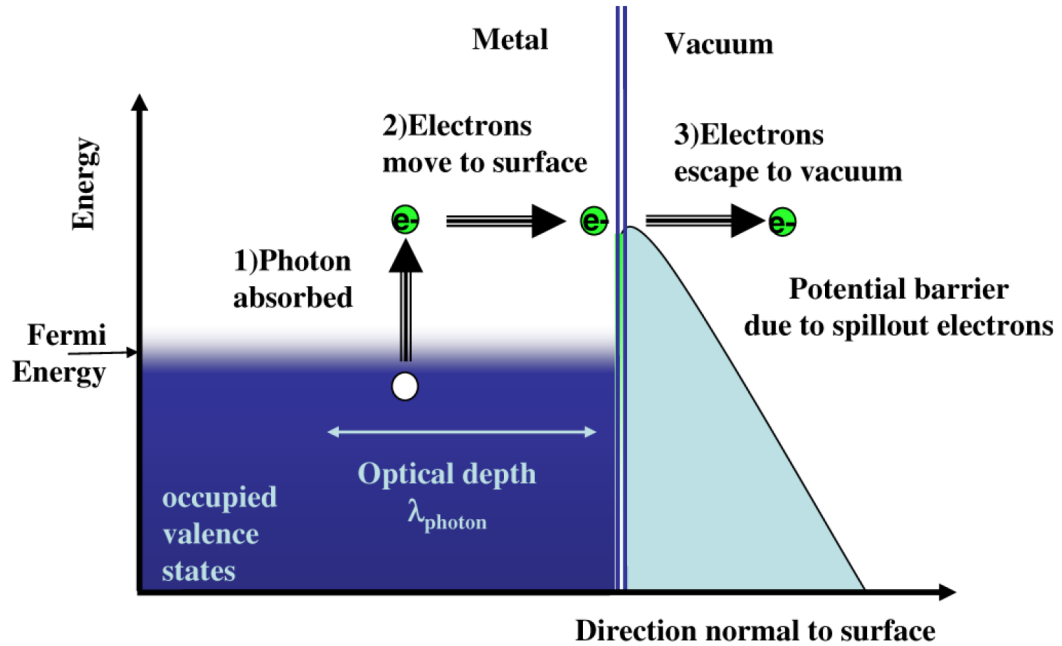


Figure 2.10. Spicer's three step model for photoemission. From Ref. [26]

- 1) Electron absorbs the laser photon
- 2) Electron transports to the surface
- 3) Electron escapes through the barrier

The Model assumes that the metal is treated as a conductor at $T = 0K$ i.e. no electrons are in the states above the Fermi energy and all states below the Fermi

energy are filled. Furthermore every absorbed photon excites one electron in the material, with an excitation probability that depends only on three parameters: photon energy, number of electrons in the occupied states and the number of available states in which the electrons can be excited.

The first step take into account the result of the Schottky effect that lower the barrier when a large external electric field is applied to the cathode. Typical values of the Schottky effect are ten's of an eV for an applied field of the order of 100MV/m. The work function for a copper cathode is $\phi_{work} = 4.6$ eV, so another effect of this barrier lowering is an increase of the quantum efficiency.

Considering that the photon energy is transferred to the electron that passes the barrier, the electron energy and hence the transverse energy spread and so photoelectric emittance are proportional to the photon energy. Therefore higher is the QE, higher is the photoelectric emittance.

After the photon absorption the electron moves to the surface in the step 2. In the transport there are electron-electron scattering that modify and redistributes the energy distribution. This process is typical in metal materials, while electron-phonon interaction acts on the electrons trough the lattice atoms in a slower time scale and is an important phenomena only for semiconductor cathodes. In fact in a metal cathode electron-electron scattering has an higher cross section compared to the electron-phonon scattering.

In order to escape the electron needs enough energy and need to have the proper direction toward the surface. The electron momentum perpendicular to the surface p_z need to satisfy

$$\frac{p_z^2}{2m} > E_{Fermi} + \phi_{work} - \phi_{Schottky}. \quad (2.61)$$

The longitudinal momentum is $p_z = p_{tot} \cos\theta = \sqrt{2m(E + \hbar\omega)} \cos\theta$, therefore the maximum angle of emission satisfies

$$\cos\theta_{max} = \sqrt{\frac{E_F + \phi_{work} - \phi_{Schottky}}{E + \hbar\omega}} \quad (2.62)$$

where E_F is the cathode Fermi energy and $\phi_{Schottky}$ is the reduction in the barrier due to the applied field. In Figure 2.11 are shown the relation between energy, momenta and angle at the inner cathode surface.

Before escaping electrons move in the metal and they can scatter, lose energy and do not escape the cathode. The mean free path for electrons excited 4 to 5 eV above the Fermi energy is 45 to 70 angstrom. Using an UV laser the absorption depth for a photon in copper is around 120 angstroms. From that follows that an electrons that absorbs a photon in the greatest depth can scatter two or three times before

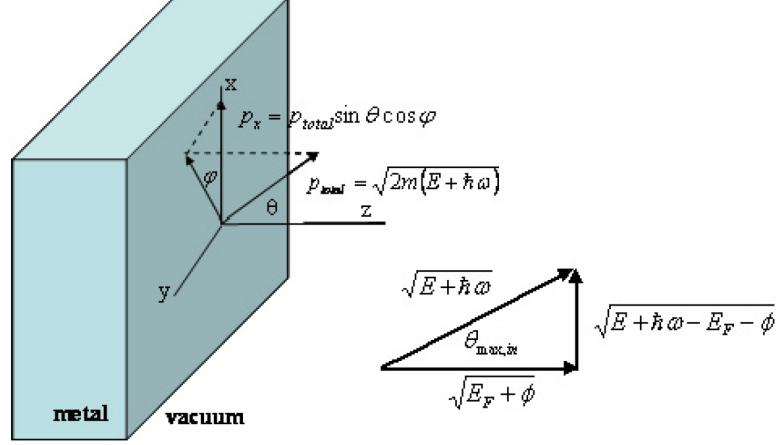


Figure 2.11. Maximum angle of emission and relations between energy and momenta at the inner cathode surface. From Ref. [25]

reaching the surface. After only one scattering, the electron loses too much energy to escape.

From these considerations and introducing an effective work function that takes into account the effect of the external RF field

$$\phi_{eff} = \phi_{work} - \phi_{Schottky} \quad (2.63)$$

the quantum efficiency is (see Ref. [28])

$$QE(\omega) = \frac{(1 - R(\omega)) E_F + \hbar\omega}{1 + \frac{\lambda_{opt}}{\lambda_{e-e}}} \frac{E_F + \hbar\omega}{2\hbar\omega} \left(1 - \sqrt{\frac{E_F + \phi_{eff}}{E_F + \hbar\omega}} \right)^2 \quad (2.64)$$

where $R(\omega)$ is the reflectivity, λ_{opt} is the photon optical depth and λ_{e-e} is the electron mean free path.

Before defining the emittance for the photoelectric emission it is possible to estimate the normalized beam divergence. While emittance is measured in meters \times radians the normalized divergence is measured only in radians. The normalized beam divergence can be written in terms of the mean square of the transverse momentum $p_x = \sqrt{2m(E + \hbar\omega)} \sin\theta \cos\phi$ obtaining (see ref [25])

$$\Delta_{photo} = \beta\gamma\sigma_{x',photo} = \sqrt{\frac{\hbar\omega - \phi_{eff}}{3mc^2}}. \quad (2.65)$$

Considering both transverse planes the normalized cathode emittance for the photoelectric emission is

$$\epsilon_{photo} = \sigma_x \sqrt{\frac{2(\hbar\omega - \phi_{eff})}{3mc^2}}. \quad (2.66)$$

With a fixed laser energy the photoelectric normalized divergence increases with the increasing of the RF applied field, as shown in Figure 2.12.

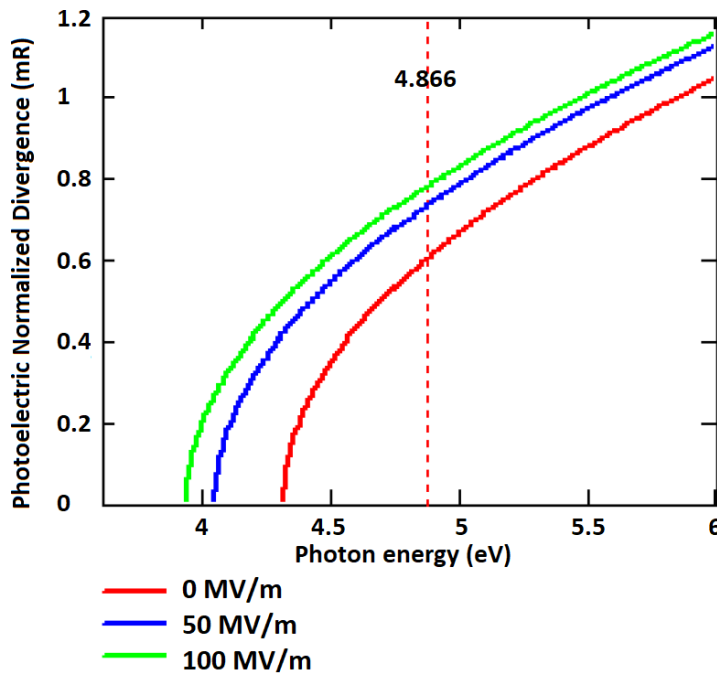


Figure 2.12. Normalized divergence as a function of the photon energy for an increasing applied field. An example of a 4.866 eV laser energy is reported. From Ref. [25]

As the RF field increases the QE increases too, so with an higher RF field it is possible to photo-extract the same charge with a lower laser spot on the cathode surface. From these consideration increasing the RF field and balancing the laser spot to the new accelerating gradient it is possible to keep under control the photo electric emittance growth.

2.6.3 Field emission

One of the effects of a strong increase of the RF field inside the gun is to better control the space charge force when the beam is not yet relativitic and also is to lower the barrier so that electrons can tunnel it achieving useful currents. A consequence of the very high RF field on the cathode surface is the field emission. Due to micro-imperfections and contaminants on the cathode surface the effective field can be strongly enhanced so that field emission occurs. The net effect on the

QE is negligible, because in some cathode areas near the imperfections the field is enhanced and in some areas is reduced.

From these considerations the cathode emittance depends on the surface roughness, so that become spatially dependent the microscopic photoemission in terms of the initial energy, the transverse velocity and the space charge density of the emitted electrons.

The field emission current density is given by

$$j_{field} = \int_a^b n(E_x, T) D(E_x, E_0) dE_x \quad (2.67)$$

where the supply function $n(E_x, T)$ is the flux of electrons that arrive up to the surface with an energy between E_x and $E_x + dE_x$, and for electrons was derived by Nordheim

$$n(E_x, T) = \frac{4\pi m k_B T}{h^3} \ln \left(1 + e^{\frac{E_x - E_F}{k_B T}} \right). \quad (2.68)$$

The barrier is the superposition of the work function, the image charge and the effect of the field RF field E_0 . The transparency function measures the transmission of the electrons through the barrier (see Ref. [25])

$$D(E_x, E_0) = \exp \left[\frac{-8\pi\sqrt{2m}}{3he} \frac{E_x^{\frac{3}{2}}}{E_0} \theta \left(\frac{\sqrt{e^3 E_0}}{\phi_{work}} \right) \right] \quad (2.69)$$

where θ is the Nordheim function that varies from 1 to 0 in the interval $0 < y < 1$ and can be approximated as $\theta(y) = 1 - 0.142y - 0.855y^2$.

The energy spectrum for field emitted electrons due to an external field E_0 and a temperature T is

$$N_{field}(E_x, E_0, T) = n(E_x, T) D(E_x, E_0). \quad (2.70)$$

The electron yield is exponential sensitive to the electric field, and only for field higher than 10^9V/m the amount of current is significant. Of course these so high fields can be achieved combining high voltage RF pulse and field enhancing from micro-imperfections and contaminants on the cathode surface. Figure 2.13 shows the field emission emittance trend for a planar emitter varying the external field.

The final effect of the roughness is also to increase the emittance, so that it depends on the amplitude n and spatial period d . It is convenient to introduce a roughness parameter

$$\xi = \frac{2\pi n}{d} \quad (2.71)$$

when this parameter approach the unity the intrinsic emittance increase about 30%, using an external applied field of 24 MV/m (see Ref.[29, 30]).

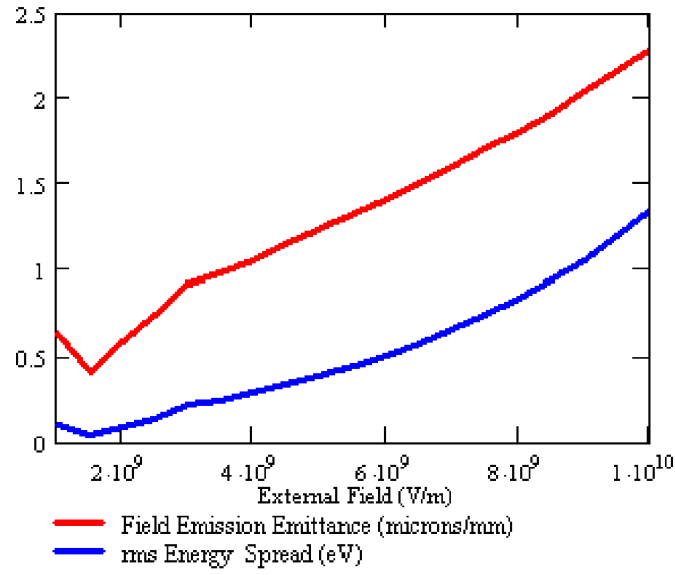


Figure 2.13. Trend of the transverse energy spread and emittance varying the applied field. From Ref. [25]

In an high field electron gun, field emission works with photoelectric effect to produce electrons, in fact, field emission reduces the barrier by means of the Schottky effect and increase the QE.

Chapter 3

Advanced High Brightness Photoinjectors

Nowadays the S-band (2.856 GHz) standing wave gun is a standard tool that is able to reach a peak field of about 120 MV/m, with an high repetition rate of about 100 Hz [31]. Most of these S-band gun are modified versions of the standard UCLA/BNL/SLAC 1.6 cells S-band RF gun [32].

As we have seen in the previous chapter to obtain high brightness beams, the layout (position and accelerating gradient of the first accelerating section, integrated solenoid field, ecc...) of a photoinjector is fixed to perform the emittance compensation scheme. A solenoid is located after the RF accelerating cells in order to keep under control the space charge effects, rotate the phase space reducing the initial space charge emittance growth.

The beam plasma oscillations induced by the solenoid enforce to inject the beam in the first accelerating section into its waist, such that the second emittance minimum moves to the photoinjector end. Furthermore the beam has to be matched to the so called invariant envelope inside the first accelerating section.

As pointed out the layout optimization for an RF photogun is very complicated and time consuming in terms of particle simulations. For example, the induced plasma oscillations depend by the bunch parameters like electron densities. Consequently the distance between cathode and first accelerating section has to be optimized, depending by the bunch parameters, in order to match the double emittance minimum and well compensate the emittance. A consequence of this is that each photoinjector layout has to be optimized in a useful range of beam parameters.

3.1 Accelerating peak field enhancement at the cathode surface

As we presented in the previous chapter the emittance compensation performed with a solenoid is able to remove only the linear effects of the space charge forces that cause the emittance growth, so that the remaining non linear space charge force effects induce an emittance growth that cannot be removed with a solenoid. From these considerations to reduce the space charge effects, it is necessary to control immediately the space charge forces after the electrons photoemission.

As seen in the calculation for the space charge emittance, the space charge force effects on the beam are damped by a factor $1/(\gamma^2\beta)$, so that they rapidly diminish with the energy increasing. One of the main effects of these forces in high brightness electron beams is the space charge emittance that, as shown in the equation 2.35, depends by the accelerating field by a factor $1/\alpha\sin\phi_0$.

These effects in general are relevant, if the beam is not yet relativistic, mostly between the photoemission process and the end of the first accelerating stage in the RF gun cavities. Of course this consideration depends by the energy at the exit of the accelerating gun cells and so by the accelerating gradient and the SW cells length. For example the space charge emittance growth, in equation 2.39, explicitly scales by a factor $1/E_0\sin\phi_0$, so that to control emittance growth becomes fundamental the strength of the field at the cathode surface that is the effective field perceived by electrons after their emission.

In the following sections we discuss some possibilities for achieving an accelerating field enhancement at the cathode surface, enhancing the peak field E_0 and/or enhancing the injection phase ϕ_0 modifying the cell length.

In the UCLA/BNL/SLAC 1.6 cells S-band (2.856GHz) photogun at SPARC_LAB, using a peak field $E_0 = 120$ MV/m an injection phase of about $\phi_0 \approx 30^\circ$ and an accelerating length of 0.1 m, the final Lorentz's gamma factor is $\gamma \approx 10 - 12$. In this gun the space charge forces diminish more than a factor 10^2 from the emission to the gun exit.

One of the main challenges for an RF gun is now to strongly decrease the final emittance avoiding the non linear space charge emittance growth. To do that it is important not only the electrons reach high energy after photoemission, but it is also fundamental to speed up that process to damp as soon as possible the space charge forces.

3.1.1 Peak field enhancement techniques

In order to enhance the field perceived by the electrons immediately after the photoemission, we can both increase the peak field E_0 and/or change the launch phase ϕ_0 between the RF and the bunch.

As we have seen in the previous chapter, the transverse RF emittance is minimized when the phase ϕ_∞ at the extraction is equal to $\pi/2$. Considering a not yet relativistic bunch, a slippage between the electrons and the relativistic wave occurs, so that the injection phase ϕ_0 has to be chosen following the equation 2.12

$$\left(\frac{\pi}{2} - \phi_0\right) \sin\phi_0 = \frac{1}{2\alpha} = \frac{eE_0}{2mc^2 \frac{2\pi}{\lambda}}. \quad (2.10)$$

So for a given geometry of the RF gun cells, once the accelerating field E_0 is fixed, only one value for the injection phase ϕ_0 minimizes the emittance, so that we have no chances to enhance the term $\sin\phi_0$ without losing the minimum emittance.

Modifying the length of the half cell it is possible to change the injection phase ϕ_0 , for example decreasing the half cell, due to a lower slippage between bunch and wave, it is possible to enhance ϕ_0 obtaining a $\sin\phi_0$ that approaches the unity. The drawback of this technique is that the effective accelerating length is reduced and the beam can exit from the gun with a lower energy, this means higher space charge forces.

For a fixed geometry of the gun cells it is possible to enhance the field on the cathode surface directly enhancing the peak field in the cavity E_0 . In this case electrons are immediately accelerated and the final energy increases. If the beam have to be manipulated for example using an RF compression (velocity bunching), the higher energy can be a drawback.

In fact in the velocity bunching, introduced by Serafini and Ferrario in Ref. [33], the bunch at the gun exit is injected in the first accelerating section, in a phase where the head experiences a decelerating phase while the tail is accelerated. The beam phase space rotates, and the bunch slips on the RF wave up to the crest and it is compressed. In order to allow the slippage between bunch and RF wave are necessary not strong relativistic beams.

A good compromise might be to increase the peak field E_0 and proportionally shorten the half cell such that E_0 and $\sin\phi_0$ increase both. In this case with a proper reduction of the RF length, the final beam energy can be equal respect the one obtained using the standard S-band gun, but particles perceive immediately a stronger accelerating field due to the increase of the both terms E_0 and $\sin\phi_0$. In fact due to the shorten RF length, the phase $\phi_\infty = \pi/2$ is reached before so that it is possible to inject the beam to an higher phase ϕ_0 and this means an higher $E_0 \sin\phi_0$.

Of course each gun is optimized according to the bunch request that must be used, and it is possible that for beams in which an RF compression is not requested, the higher energy could not be a drawback.

For example enhancing E_0 and shortening the cell, so that the integrated accelerating field is the same of the UCLA/BNL/SLAC 1.6 cells S-band photogun, it is possible to obtain the same bunch with an energy of about 5/6 MeV at the gun exit, preserving the Ferrario working point and the possibility to compress the bunch with an RF compression.

There were some attempts at SPARC_LAB in order to enhance the peak field, decreasing the RF pulse shape in the gun to avoid breakdown due to the combined effects of pulsed surface heating and large electric field. Another way, as we will see in next subsection, is the use of structures operated at cryogenic temperatures that allow higher gradients to be used.

The relation between RF pulse duration and peak field for example was measured at SPARC_LAB (see Ref.[34]). The SPARC_LAB gun after seven years of run, did not reach the nominal field value of 120 MV/m that corresponds to an RF peak level of about 10 MW dissipated in the gun using a $4\mu s$ pulse duration. The nominal beam energy at the entrance of the linac is 5.6 MeV. With nominal $4\mu s$ pulse length the operation was limited by a large breakdown rate and the maximum power inside the RF gun had to be significantly reduced, so that the measured energy at the exit of the gun went down to 4.5 MeV. Of course under these conditions the beam quality was spoiled because of the emittance degradation due to space charge effect inside the gun. By these reasons was studied the possibility to enhance the peak field E_0 , reducing the duration of the RF pulse so that the breakdown rate inside the RF cavities is reduced. Due to system limitations the RF can not shrink more and more, the minimum duration was calculated to be in a range of about $1/2\mu s$. As shown in Figure 3.1, the best result was obtained shortening the RF pulse up to $1\mu s$. After that optimization the beam quality was enhanced, obtaining a peak brightness improved of a factor 2.6.

Another option is to operate to an higher RF frequency. A first expression for the breakdown threshold in metals was obtained empirically by Kilpatrick in 1957 from experimental data. This expression relates the maximum electric field E before breakdown occurs in a cavity, with the RF frequency f considering the probability of field emitted electrons

$$f = 1.64E^2 e^{-\frac{8.5}{E}} \quad (3.1)$$

where f is measured in MHz and E in MV/m. This relation is known as the Kilpatrick criterion (see Ref. [35]). This formula was obtained studying parallel plates electrodes

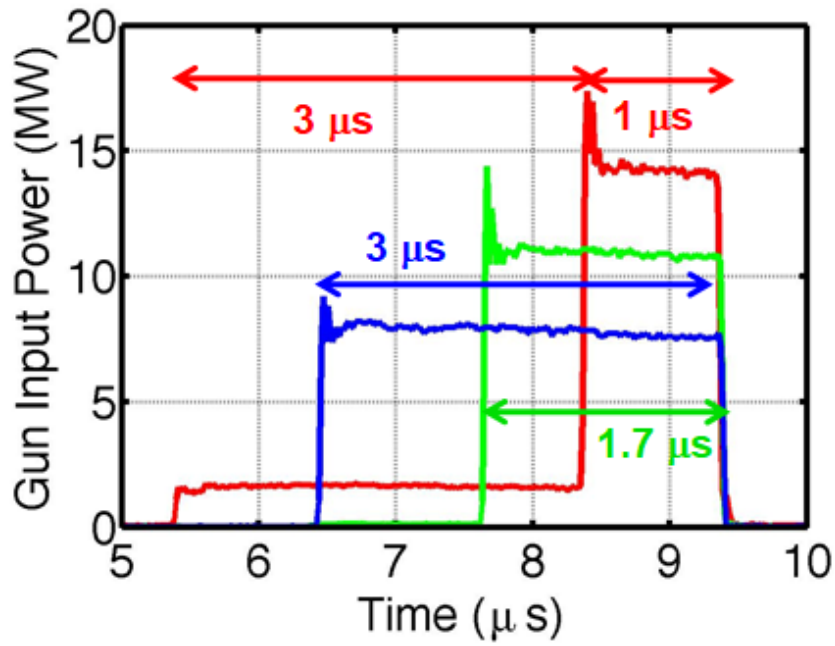


Figure 3.1. Different RF pulse durations was tried in gun at SPARC_LAB, in order to enhance the peak field E_0 . The blue line corresponds to 7.5 MW of dissipated power in the gun, that corresponds to $E_0 = 95$ MV/m and a final beam energy of 4.4 MeV. The green one corresponds to a power of 11 MW, a peak field of $E_0 = 115$ MV/m and a beam energy of 5.1 MeV. The red line corresponds to the best obtained result, a duration of the peak pulse of 1μ with a rise time of 3μ s. With this final configuration was reached a peak field of 130 MV/m, a dissipated power of 14 MW and a final beam energy of 6.2 MeV. In the last configuration the emittance growth due to the space charge forces are partially mitigated and the peak brightness increases of a factor 2.6. From Ref. [34]

with a gap, and so it is not a criterion for RF breakdown in accelerators, which have varieties of cavity shapes. Also the modern vacuum equipment and surface machining techniques are very different.

A most recent scaling law compared to the Kilpatrick criterion has been provided by Wang (see Ref. [36]) studying the field electron emission from microprotrusions in the cavity surface. Assuming that the microscopic field E in the cavity is enhanced by a factor β to an higher microscopic value E_m at the tip of the microprotrusion so that

$$E_m = \beta E. \quad (3.2)$$

The new criterion considered Cu S-band (frequency of 2856 MHz) cavities at SLAC, for a measured $\beta = 102$ and a field limit due to the breakdown of 300 MV/m. This criterion relates the frequency to the electric field as

$$f = 6.55 \times 10^{-3} \beta^{1.75} E^{1.25} e^{\frac{-6.68 \times 10^9 \phi^{1.5}}{\beta E}}. \quad (3.3)$$

where f is the RF frequency in MHz, E is the surface electric field limit in V/m, ϕ is the work function of the cavity material in eV and β is measured enhancement factor. Trends of the equation 3.3 are reported in Figure 3.2. For a fixed RF frequency the breakdown limit increases with the β decreasing.

The β parameter can increase respect the one at the beginning of the operation, so that the breakdown threshold decreases with time. This progress is represented in Figure 3.2 by a dashed horizontal line. Furthermore the physical meaning of the scaling of the breakdown limit with the frequency can be interpreted with the microwave scaling law, according to which a lower RF frequency needs larger cavities and so a larger area where breakdown can occur. From these consideration for a fixed β an higher RF frequency has an higher RF breakdown threshold.

Therefore various materials have been tested during the years in order to find the one with the higher damage threshold [37]. As it shown in the next section by a recent study the breakdown limit does not depend directly by the RF frequency, but by the pulsed heating, by the peak electric field and by the RF pulse length. By the frequency increase, it is possible to enhance the peak field considering for example shorter RF pulses. By the cells volume reduction we need less RF power too. Furthermore the fill time needed for resonantly inserting into, and extracting power out of, such standing wave device scales as $\tau_{fil} \propto f_{RF}^{-3/2}$. In X-band ($f_{RF} = 11.424$ GHz) very large field, up to 250MV/m, have been demonstrated (see Ref.[38], but with a smaller normalized vector potential $\alpha = 0.8$ and so without strong structure shortening, with respect to the S-band structure, it is difficult to increase the launch field ϕ_0 . Furthermore for a reduced X-band structure the focusing system needed

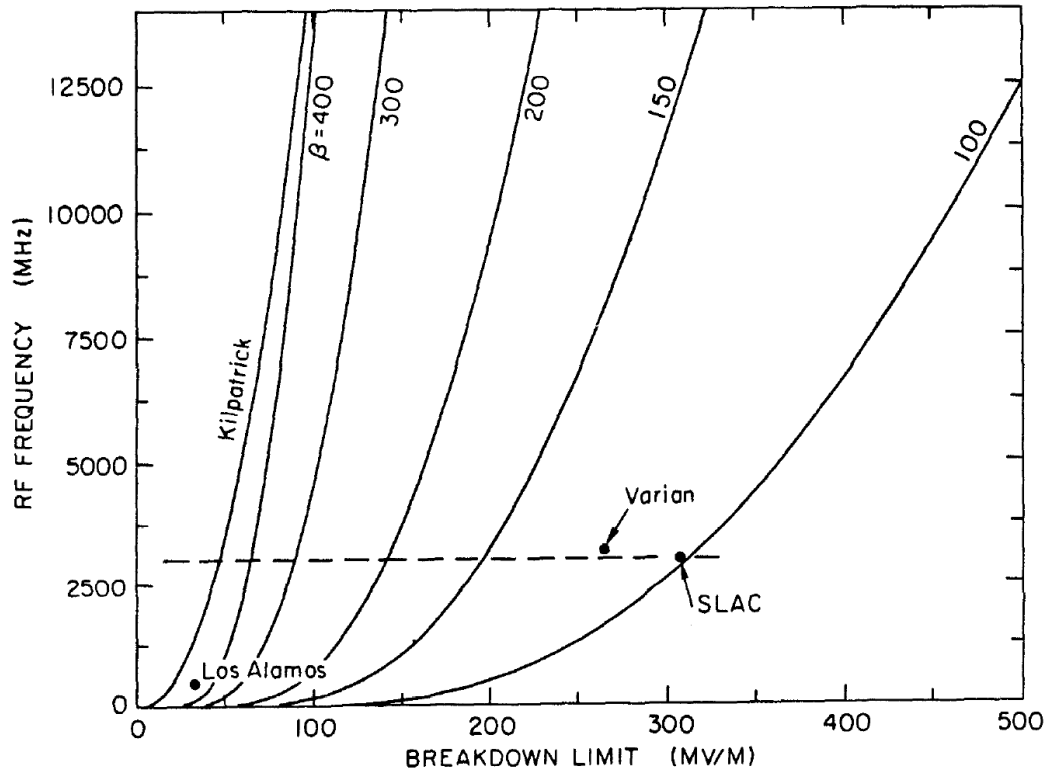


Figure 3.2. Breakdown limit (in MV/m) for different RF frequency (in MHz) for different values of the β parameter. The dashed line represents different breakdown limits for a fixed frequency of 2856 MHz, varying the β parameter. Due to the surface copper degradation caused by operation, the β parameter can increase with time respect the one at the beginning of the operation, so that the breakdown threshold decrease with time. From Ref. [36]

for the emittance compensation is more challenging.

In the next sections we present two new scenarios, the first one takes advantage by an high gradient S-band reduced half cell, operating at cryogenic temperatures and it is able to increase the brightness at least over an order of magnitude with respect to the present LCLS gun. Considering this gun I did simulations to reproduce some working point yet optimized and optimizing a new working point considering a very low charge beam of 0.1 pC.

The second scenario is completely new and takes advantage from an higher RF frequency 1.6 cells high gradient C-band (5.712 GHz) gun. I present the beam dynamics properly scaling lengths and fields, in order to maintain the Ferrario working point. In this configuration the beam peak brightness increases respect the state of the art, reaching a value of about $B \approx 5 \times 10^{16} A/m^2$.

3.1.2 Cryogenic operation in RF structures to increase the peak field

As we have seen in the previous sections to increase the beam peak brightness is necessary to augment the peak field at the cathode surface to immediately control the space charge forces that cause an emittance growth. An option to directly increase the peak field in the cavities is the cryogenic operation of copper structures (see Ref. [39]), this permits an higher breakdown threshold.

It was demonstrated (see Ref. [37] and [40]) that breakdown rate depends more on the peak magnetic field, through pulsed heating, than the peak electric field. In fact thermal stresses induced by RF pulsed heating cause microcracks and a consequent surface roughness augment that limit the maximum electric field. Therefore pulsed RF generates structure heating that limits the maximum electric field. The RF breakdown is a very complicated phenomenon that in order to be understood need different fields of physics such as structure of matter, plasma and surface physics and electromagnetism. Also another work (see Ref. [41]) correlates the breakdown rate with the peak pulse surface heating.

A possible mechanism that explains rise in cavity roughness and breakdown, was found studying a metallic surface subject to intense electric field and in presence of near surface void. Ref. [42] shows that under these conditions the nucleation of dislocations on the void surface occurs. These dislocations create a mass slippage along the material. In order to enhance the resistance to these dislocations are used copper alloys that have greater yield strength.

At SLAC was studied the possibility to strongly increase the peak field using these copper alloys (CuAg) and also operating at cryogenic temperatures that enhance more the yield strength. The results show the possibility to strongly increase the

peak field and the accelerating gradient in the cavities before breakdown occurs. Figure 3.3 and Figure 3.4 show the SLAC results using a single X-band cell, as predicted an harder alloy improves the peak electric field and the accelerating gradient. Furthermore using cryogenic temperatures ($T = 45$ K) the yield strength is strongly enhanced and it is possible to strongly increase the surface electric field up to reach $500\text{MV}/m$. As we have seen this is due to the increased yield strength and to the lowering of surface heating due to the diminished surface resistivity.

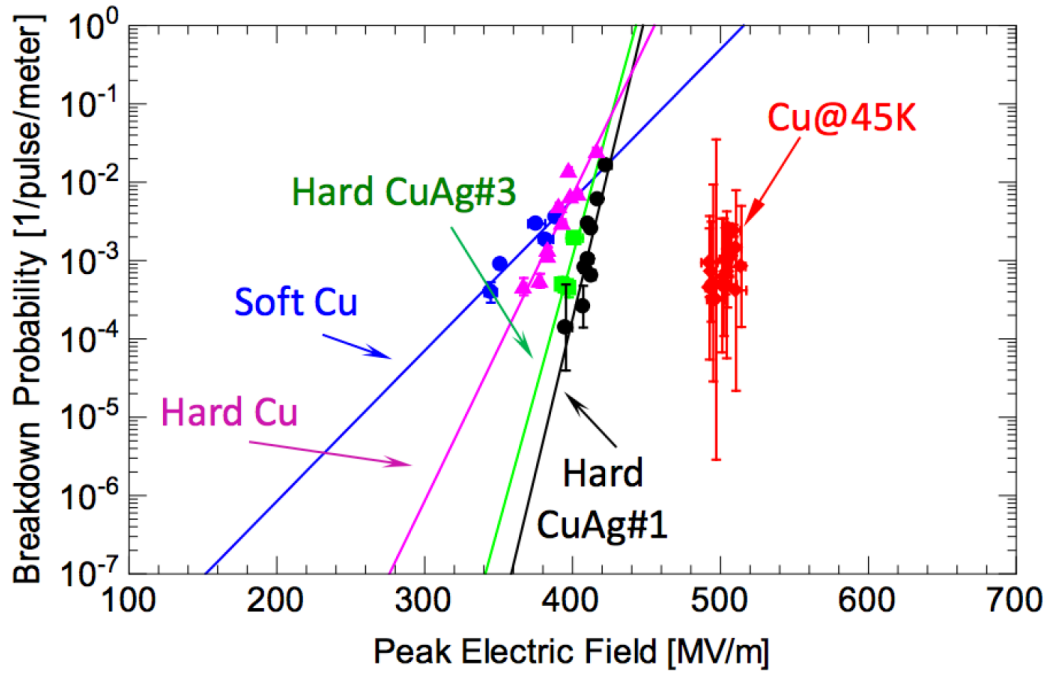


Figure 3.3. Breakdown probability as a function of the surface peak electric field. Recent experiments at SLAC using a single cell Xband, show that using a copper alloy it is possible to increase the peak electric field. Operating at cryogenic temperature ($T = 45$ K) the surface peak electric field is strongly enhanced up to reach $500\text{ MV}/m$. From Ref. [39]

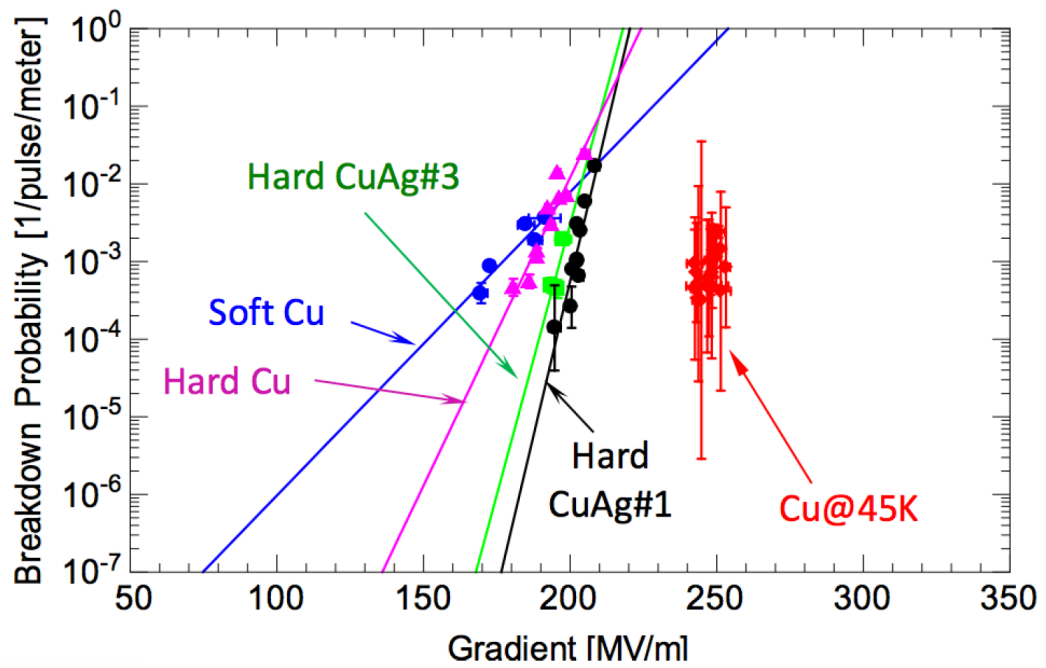


Figure 3.4. Breakdown probability as a function of the accelerating gradient using a single X-band cell, obtained at SLAC. From Ref. [39]

3.2 Ultra high field cryogenic RF S-band gun

A recent proposal for a very high performance S-band gun was made in order to obtain high brightness electron beams from an ultra high field cryogenic RF gun (see Ref. [39]). This device combines cryogenic temperatures of the cavities (27 – 40K) to reduce breakdowns and a reduced length of the half cell (1.45 cells). The peak field on axis can reach the value of 250 MV/m. The normalized vector potential associated with this accelerating field becomes extremely large in fact $\alpha = 4$. The S-band frequency was chosen in order to substitute the present S-band photoinjector at LCLS. The layout of this device is shown in Figure 3.5.

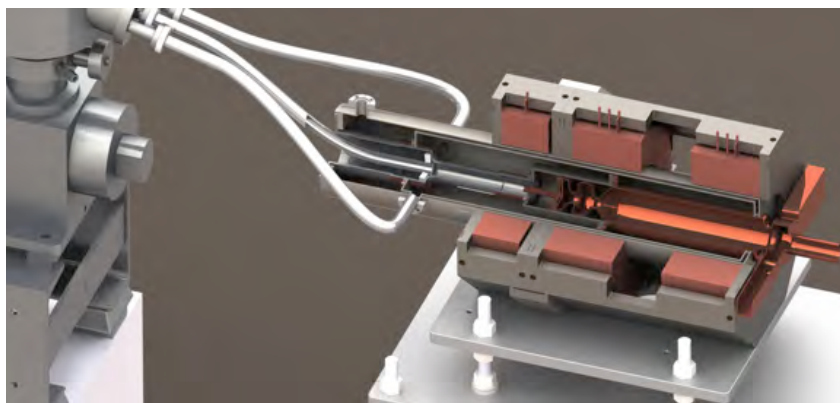


Figure 3.5. Design of the cryogenic S-band gun with 1.45 cells. On the left the cryostat and the cryocooler. From Ref. [39]

The main goal of this device is to increase the final beam brightness, to do that it is fundamental to minimize the intrinsic emittance. Considering an electrons emission temperature T that follows a Maxwell-Boltzmann distribution, the intrinsic beam brightness is

$$B = \frac{2I}{\epsilon^2} = \frac{2J_{max}m_e c^2}{k_B T}. \quad (3.4)$$

As we have seen in the previous chapter in the photoemission process, we have to consider a Fermi-Dirac distribution that leads to the normalized cathode emittance for the photoelectric emission defined in equation 2.66. This essentially means that $k_B T \propto (\hbar\omega - \phi_{eff})$. A definition of a the intrinsic beam brightness for electron photoemission is:

$$B = \frac{2I}{\epsilon^2} = \frac{3J_{max}m_e c^2}{\hbar\omega - \phi_{eff}} \quad (3.5)$$

where $\phi_{eff} = \phi_W - \phi_{Schottky}$.

As suggested in Ref. [26] tuning the laser photon energy closer to the effective metal work function of the material, it is possible to improve the intrinsic emittance. An attempt to lower intrinsic emittance was done (see Ref. [43]) tuning the energy of

a Ti:sapphire laser, to reduce the quantity $\hbar\omega - \phi_{eff}$. This work has led to an intrinsic emittance reduction of about 20%. As the cathode QE scales as (see Ref. [26])

$$QE \propto (\hbar\omega - \phi_{eff})^2 \quad (3.6)$$

the laser energy has to be sufficient to compensate the lowering of the QE, due to the cathode lower temperature.

A more effective approach to increase the electron beam brightness is to augment the current density, this can be achieved increasing the cathode peak field $E_0 \sin\phi_0$. The physical relation between these quantities can be clarified through the model of a short initial beam regime (blow out) (as described in Ref. [44], [39]), where the maximum current density obtained from a photocathode in 1-D approximation is

$$J_z \approx \frac{ec\epsilon_0(E_0 \sin\phi_0)^2}{m_e c^2}. \quad (3.7)$$

Using the 1-D approximation the limiting current in the blow out regime for a beam with cross section πR can be written as:

$$I_b \approx J_{z,b} \pi R^2 = I_0 \frac{\pi}{4} (\gamma' R)^2 \quad (3.8)$$

where $\gamma' = \frac{E_0 \sin\phi_0}{m_e c^2}$ and R is the beam radius. Significantly increasing the quantity $E_0 \sin\phi_0$ it is possible to increase the beam brightness, and as we have seen before there are several approaches to do that.

In the device in Ref. [39], it is used a reduced 1.45 cell π mode S-band photoinjector that takes advantage from cryogenic temperatures (27–40 K). The peak electric field is 250 MV/m and $\sin\phi_0$ approaches the unity, so that the electric field on the cathode surface $E_0 \sin\phi_0$ is four times larger than the one used in the UCLA/BNL/SLAC 1.6 cells S-band RF gun operating with a peak field of 120 MV/m. From these consideration, the intrinsic brightness is predicted to be 16 times larger respect the one in a 120 MV/m 1.6 cell S-band gun using the blowout regime. Due to the higher peak field compared to the one in the standard S-band gun, the beam exits the photoinjector with approximately twice energy.

The beam dynamics for a relatively high charge case (125 pC) was simulated using the software General Particle Tracer (GPT) (see Ref. [1] and taking into account a blowout regime with laser pulse parameters reported in Figure 3.6. To compensate the emittance a 20 cm long solenoid, equal to the SPARC_LAB one (see Ref. [22]) with peak magnetic field of about 0.5T was used. After the solenoid are placed three S-band sections to boost the beam energy.

Due to the higher energy at the gun exit, plasma oscillations have different evolution

Laser pulse length	35 fs FWHM,
Laser spot size (cut transverse Gaussian)	Hard edge at 262 μm , 1.6σ , (120 μm rms)
RF gun format	1.45 cell π -mode standing wave
Peak cathode electric field	250 MV/m
Launch phase	82 degrees
Focusing solenoid (SPARC-type) field	5.4 kG
Post-acceleration linac average field	20 MV/m

Figure 3.6. Laser parameters for the high charge, blowout regime. From Ref. [39]

along the beam line. Studying the double emittance minimum the first structure position is located at 1.7 m, so that the invariant envelope is reached and the emittance is well compensated along the beam line. Thermal emittance is fixed to be $0.1\text{mm} - \text{mrad}$. The beam energy at the gun exit is about 10.5 MeV and the current at the injector end is about 100A.

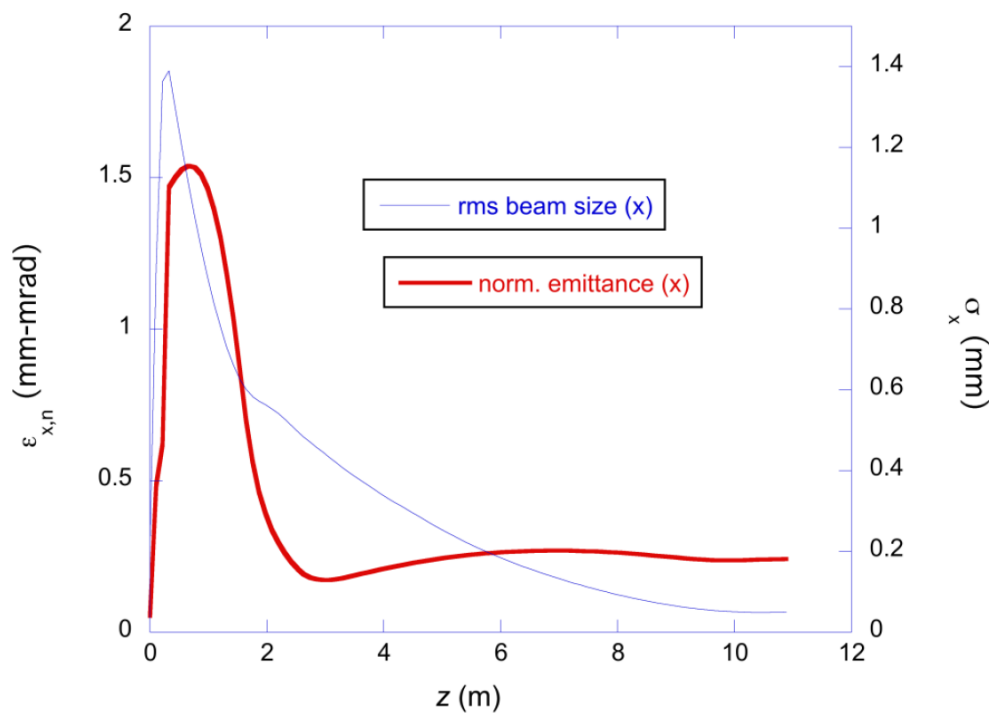


Figure 3.7. Spot size and emittance evolution along the linac. The emittance is well compensated focusing with a solenoid magnetic of 0.2 T. The final normalized rms emittance value is $\epsilon_{x,n} \approx 0.2\mu\text{m}$ From Ref. [39]

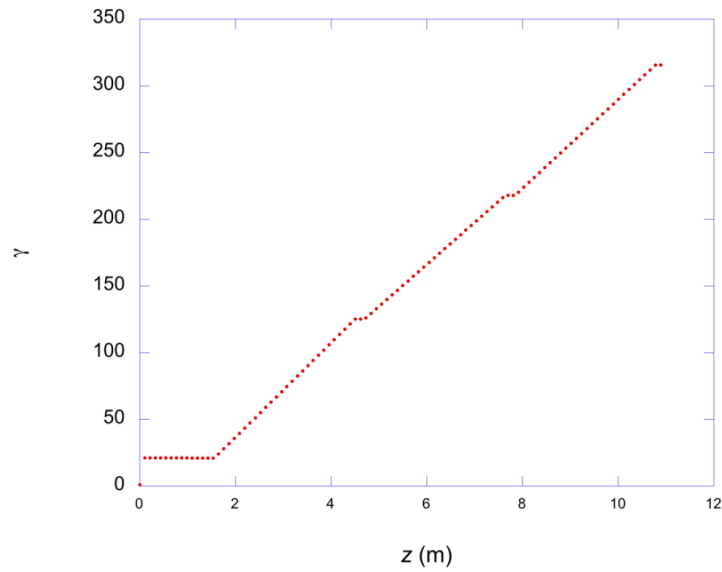


Figure 3.8. Trend of the beam energy along the photoinjector. In y axis there is the Lorentz' gamma. At the gun exit the bunch energy is approximately 10.5 MeV. In order to boost the energy, three S-band section (each one 3 m long) with an accelerating gradient of 20 MV/m are used. The energy after post acceleration is 161 MeV. From Ref. [39]

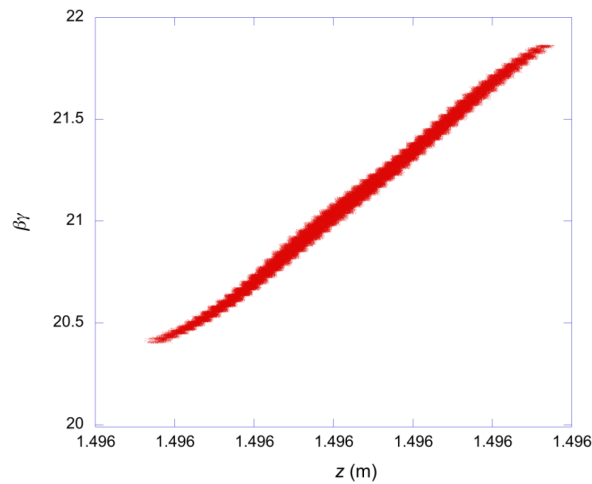


Figure 3.9. The phase space at the gun exit is highly linear, so that in principle is possible to perform a strong RF compression. From Ref. [39]

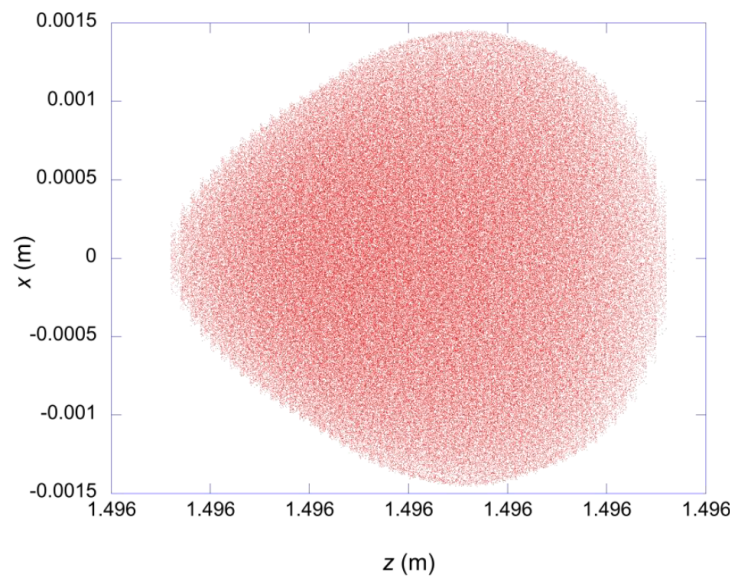


Figure 3.10. Projection on the x-y plane of the beam charge distribution in the 125 pC blowout regime. From Ref. [39]

In order to reduce the beam emittance to very low values another bunch configuration was tested, taking advantage from the so-called cigar-shaped beams (see Ref.[45]). In this configuration the laser transverse and longitudinal dimensions are related by $\sigma_x \ll \sigma_z$, so that the intrinsic emittance is reduced according to equation 2.66. In this regime, the extracted charge density by the cathode approaches the limit set by the saturation limit. In fact the value of σ_z has to be chosen at the point of full emission from the cathode such that $\sigma_z \approx \frac{1}{2} \left(\frac{eE_0 \sin \phi_0}{m_e} \right) \sigma_t^2$. In the emission process of such a beam, the image charge at the cathode surface spreads out during the "long" emission process so that the decelerating fields generated by image charges are diminished. From these considerations in the cigar regime a higher charge per unit area can be extracted and launched, and it is possible to reach higher peak currents and lower intrinsic emittances. From the analysis in Ref. [46] the space-charge limiting current in the cigar regime I_c considering a beam with cross section πR^2 is

$$I_c \approx I_A \frac{\sqrt{2}}{9} \left(\frac{E_0 \sin \phi_0 R}{m_e c^2} \right)^{\frac{3}{2}} = I_A \frac{\sqrt{2}}{9} (\gamma' R)^{\frac{3}{2}}. \quad (3.9)$$

Considering the ratio between cigar to blowout current we obtain

$$\frac{I_c}{I_b} \approx \frac{4I_A}{9\pi} \left(\frac{2}{\gamma' R} \right)^{\frac{1}{2}} \approx 0.2 (\gamma' R)^{-\frac{1}{2}}. \quad (3.10)$$

Taking into account the previous high charge case and an rms equivalent cylindrical

beam size of $220\mu\text{m}$, the factor $(\gamma'R)^{-\frac{1}{2}} = 3$ so that $I_c/I_b \approx 0.6$. This shows that considering an high charge beam the cigar regime is not convenient, because in order to keep constant the spot size and intrinsic emittance, the bunch length increases and the resulting peak current decreases.

A working point with very low charge ($Q=1.67\text{ C}$) was optimized in Ref. [39] using 2 ps full width long beam with an hard edge spot size of $20\mu\text{ m}$. In that case the factor $(\gamma'R)^{-\frac{1}{2}} = 10$ leads to $I_c/I_b \approx 2$ i.e. a current that is twice the one possibles using blowout.

This scenario was simulated with GPT using the gun and the solenoid. The solenoid generates a beam waist in $z = 2.2\text{ m}$ and the final compensated normalized emittance reaches the value of about $5 \times 10^{-3}\text{ mm mrad}$.

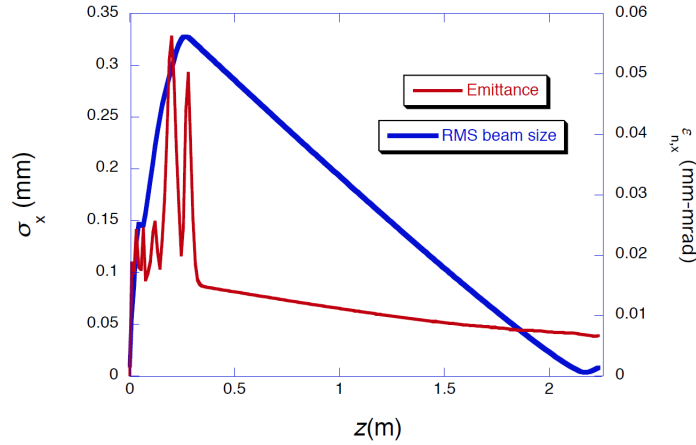


Figure 3.11. Spot size and emittance evolution after gun and solenoid. Emittance is well compensated up to reach the value of $5 \times 10^{-3}\text{ mm mrad}$. The first accelerating structure has to be placed in the beam waist at $z = 2.2\text{ m}$. From Ref. [39]

In the cigar regime the intrinsic emittance is reached at the end of the compensation process, the peak current is $I = 1.3\text{ A}$ that leads to a peak brightness of about $1.4 \times 10^{17}\text{ A/m}^2$.

I tested with GPT a very low charge ($Q = 0.1\text{pC}$) cigar regime, that can be useful for example to satisfy the stringent beam parameters requested to perform the Quantum Free Electron Laser (QFEL). After the gun and the solenoid two S-band section (each one 3m long), their phases are optimized to work in velocity bunching in order to strong compress the beam and boost the beam energy up to 30 MeV . The optimized position for the start of the first section is $z = 2.16\text{ m}$, where the beam has its transverse waist. Both accelerating sections are surrounded by solenoid equal to the SPARC_LAB ones (see Ref. [47]) that provide focusing during the bunch compression in order to control the transverse beam shape. The phases of both section are set to compress the beam using the velocity bunching.

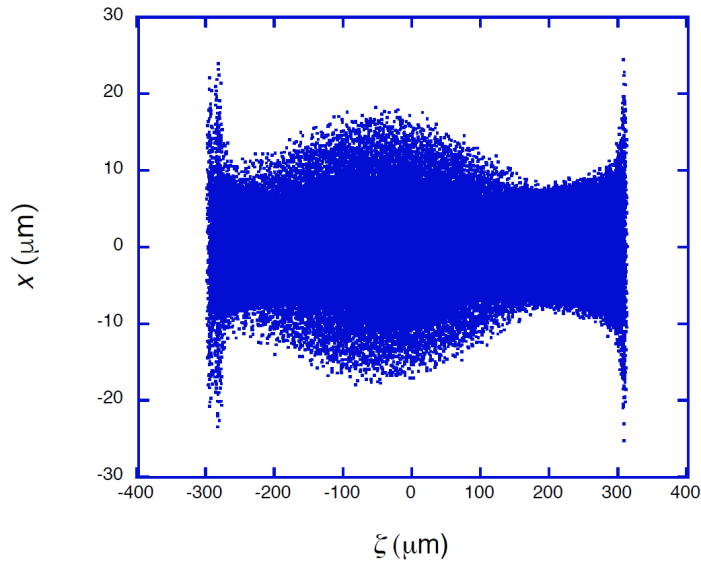


Figure 3.12. Charge distribution at the beam waist at $z = 2.2$ m, where the starting distribution is quite restored. On the x axis there is the longitudinal bunch coordinate, while in the y axis there is the bunch transverse coordinate. From Ref. [39]

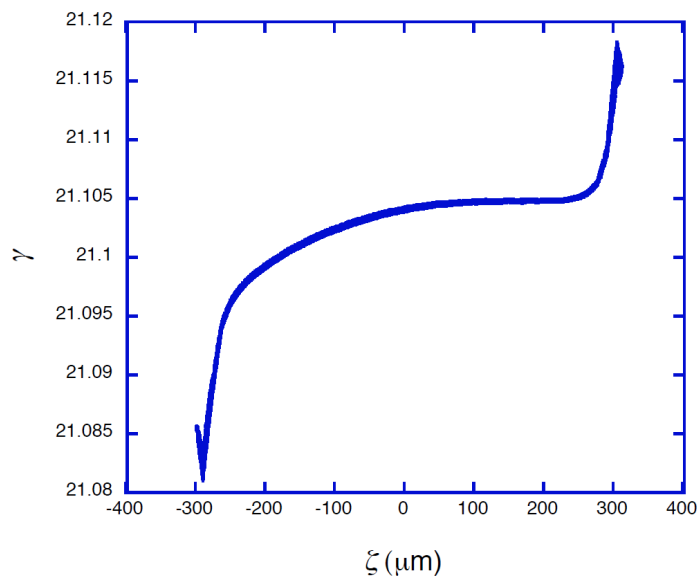


Figure 3.13. Longitudinal beam phase space distribution at the beam waist, on the y axis there is the Lorentz' gamma. Due to the bunch length the distribution acquires some non linearities. From Ref. [39]

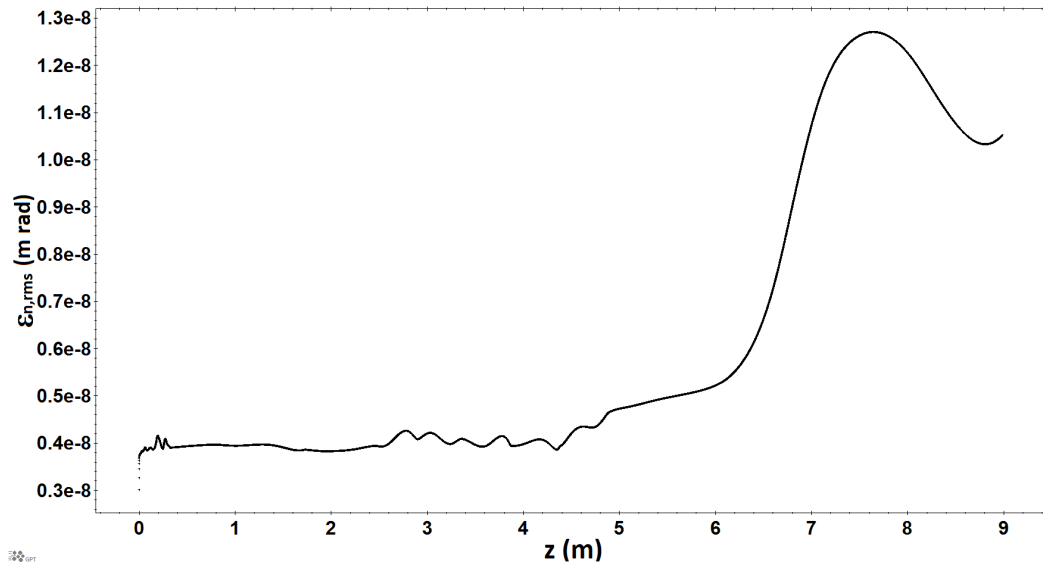


Figure 3.14. Trend of the normalized rms emittance along the photoinjector. The final $\epsilon_{n,rms}$ is over 11 nm. In order to obtain a very short beam, the solenoid around the second section is powered with a lower current so that an emittance growth during the compression in the second section occurs.

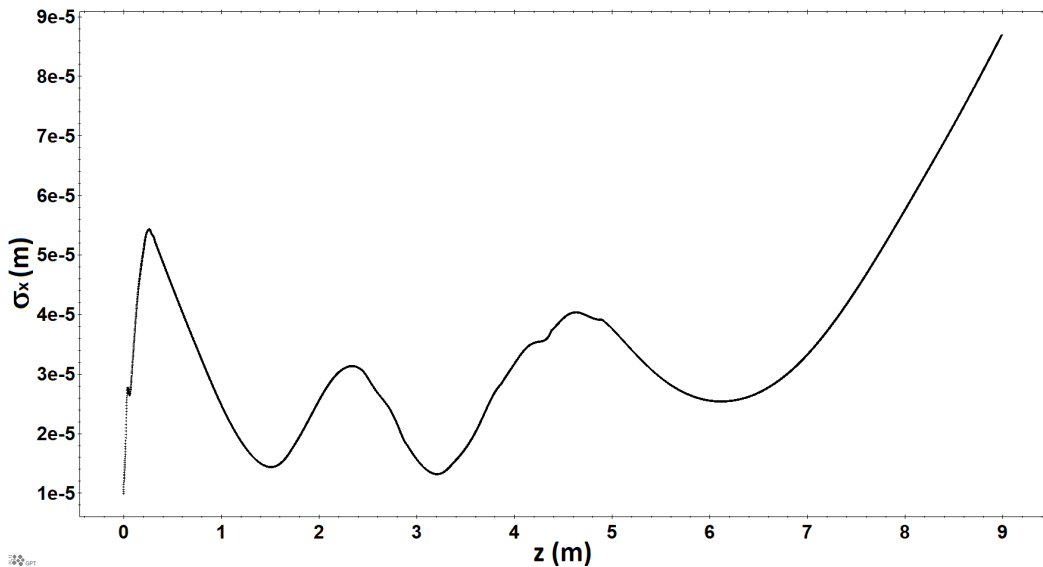


Figure 3.15. Trend of the beam spot size along the photoinjector.

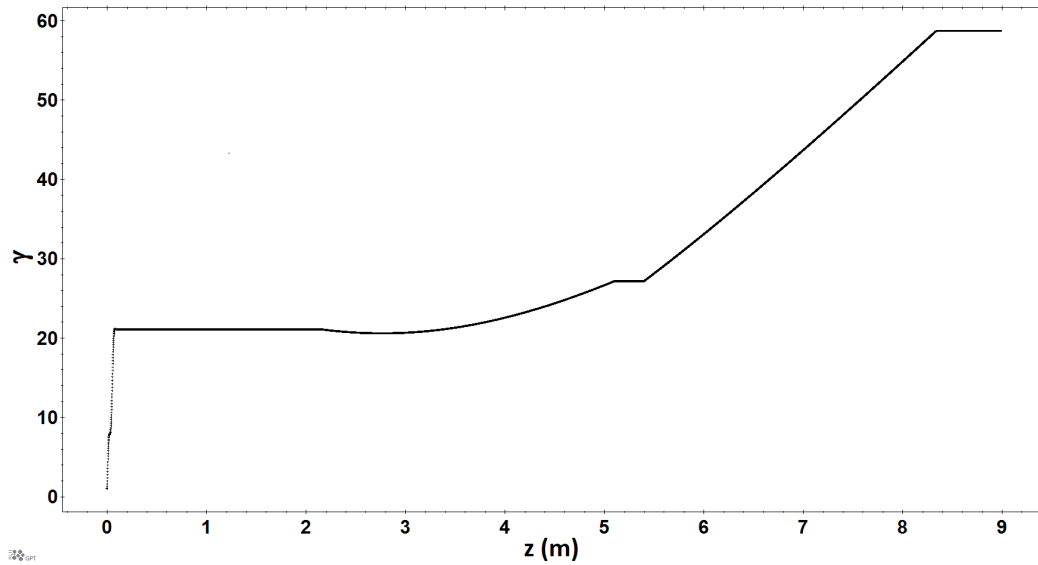


Figure 3.16. Trend of the beam energy along the photoinjector, using a very low charge beam (0.1 pC) with a cigar shape. The phases of both section are set to compress the beam using the velocity bunching. In the first section electrons enter with a lower energy so that they can slip and compress more on the RF wave. This means that they are injected farther with respect to the wave crest. This higher beam slippage means a lower energy gain. Due to the higher bunch energy, electrons are injected in the second section closer to the RF wave crest, so that they gain more energy compared to the first section.

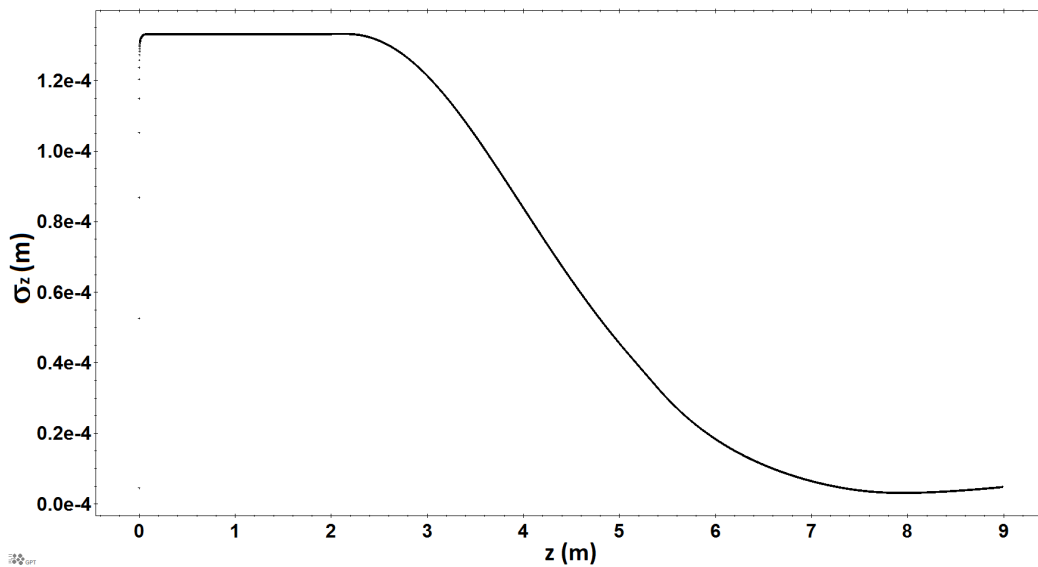


Figure 3.17. Trend of the rms bunch length σ_z along the photoinjector. In the y axis there is the rms bunch length that, due to the velocity bunching performed in the two sections, is compressed by a starting value of $\sigma_z \approx 130\mu$ m up to reach a final value of $\sigma_z \approx 3\mu$ m. In the horizontal axis the longitudinal bunch positions are reported.

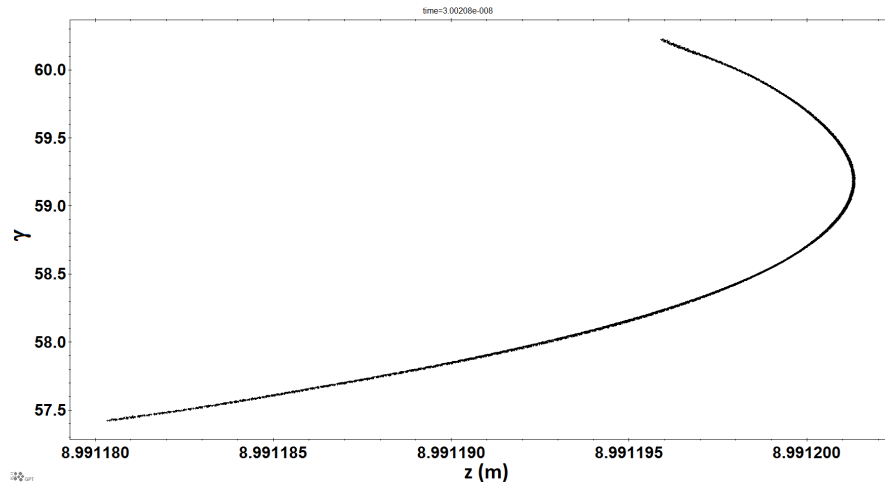


Figure 3.18. Longitudinal phase space at the end of the photoinjector, on the y axis there is the Lorentz' gamma and on the x axis there are the longitudinal bunch positions.

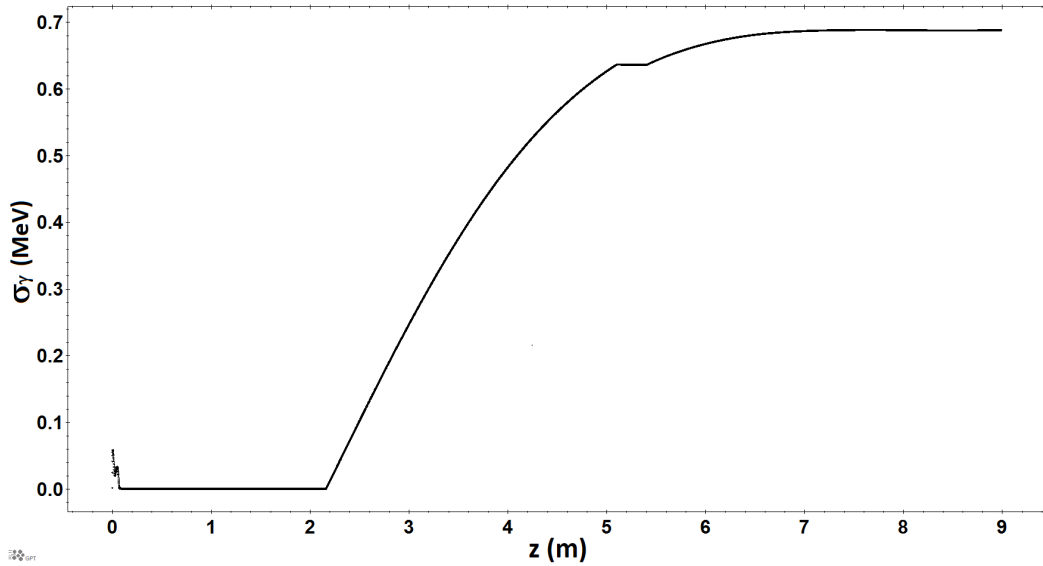


Figure 3.19. Trend of the σ_γ along the beam line. In the horizontal axis there are the longitudinal bunch positions. The final normalized energy spread is about $\sigma_\gamma/\gamma \approx 1 \times 10^{-2}$.

As shown in Figure 3.16 and in Figure 3.17 the bunch is injected in an optimized compression phase near the zero crossing, so that the beam slips and is strong compressed by the RF wave and the energy gain is very low. Being the beam too much relativistic compared to the usual beam that exits from the standard S-band gun the slippage is not so strong and a little deceleration is necessary inside the first section. In the second section due to the higher electrons energies the slippage between bunch and RF wave is lower and the beam is injected in the optimized phase of $\phi = \phi_{crest} - 75^\circ$. In order to reach a very short final beam of $\sigma_z = 3\mu\text{m}$ the magnetic field from the solenoid around the second section is reduced. Due to this limited phase slippage and to a reduced magnetic field, the energy spread in Figure 3.19, the beam spot size in Figure 3.15 and the emittance in Figure 3.14 increase in the second accelerating section.

The longitudinal phase space reported in Figure 3.18, presents a typical comma shape. This means that the maximum compression is almost achieved and some device (see Ref. [48]) that linearizes the longitudinal phase space is necessary.

These beam parameters can be useful to guide an experiment on QFEL where the beam parameters nowadays are challenging. Table 3.1 reports a possible list of beam parameters needed to perform a QFEL experiment. In the right column are reported the results of the GPT simulation. In red are reported the parameters to improve to perform a possible experiment. To match the beam spot size, a not yet simulated final focus is necessary, using for example the SPARC_LAB high gradient (520 T/m) permanent magnets.

Although the high gradient in a RF photogun is an advantage that allows to control rapidly the space charge forces, and hence the irreversible increase of the emittance by nonlinear forces, the higher gradient presents some problems that are currently being studied. The main one seems to be that the copper surface subject to high electric field generates an higher field emission current (dark current). As seen in the previous sections the net effect of the electric field on the cathode surface is to diminish the barrier ϕ_W through the Schottky effect so that we have defined an effective barrier potential $\phi_{eff} = \phi_W - \phi_{Schottky}$.

Nowadays a possible solution seems to be to apply a layer coating on the copper surface, and different materials subject to high field are under study.

Table 3.1. A possible list of beam parameters for a QFEL experiments from Ref. [49]. The right column reports the GPT simulation results, in red are the parameters to be optimized to perform the experiment.

BEAM PARAMETERS	THEORETICAL REQUEST	GPT SIMULATION RESULTS
Beam energy γ	51.98	59
Bunch charge Q [pC]	0.1(Changeable)	0.1
Normalized rms emittance ϵ_n [mm mrad]	0.01	0.01
rms beam spot size σ_x [μm]	0.63	80
rms beam peak current I [A]	10	10
rms beam length σ_z [μm]	3.0(Changeable)	3.1
Energy spread σ_γ/γ	10^{-5}	10^{-2}

3.3 High gradient, higher frequency and Ultra-High brightness C-band gun

As we have seen in the previous sections there are various possibilities to enhance the peak field in a SW gun. Because the limit is the breakdown induced by heating magnetic field pulse, as we have seen another more obvious solution is the operation at cryogenic temperatures, that in S-band allow to achieve a peak electric field of 250 MV/m. The higher peak field in the S-band device described in the previous section produces higher energies of the electrons at the gun exit. These higher energies can be a drawback in the case we need very short bunches obtained with the velocity bunch technique. In fact, considering an higher charge respect the last one (0.1 pC) of the previous section, by simulation with GPT, to obtain an high compression with the velocity bunching, initially we need to decelerate the bunch so that it becomes less relativistic and slips more easily along the wave. This deceleration, and in general a slower slippage on the wave, generates an higher bunch energy spread because bunch particles explore different accelerating fields for a longer time. Of course an higher energy does not represent any problem in linacs where the velocity bunching is replaced by a magnetic chicane that is able to compress the bunch also at higher energies.

A possible solution to keep higher peak fields and which allows at the same time to have a final beam energy of 5 – 6 MeV, as in the case of the well known UCLA/BNL/SLAC 1.6 cells S-band RF gun, where the beam dynamics and working points are known, is to replace the S-band frequency with a C-band one. In fact setting the cavities geometry at 1.6 cells, the accelerating length in a C-band gun is the half of an S-band one, because the RF wavelength λ_{RF} is the half ($\lambda_{RF,C}(5.712\text{GHz}) = \lambda_{RF,S}(2.856\text{GHz})/2$) and also the cavity length scales with the same factor two. Keeping the peak accelerating field of $E_0 = 240\text{MV/m}$ i.e. exactly of a factor two compared to the standard S-band gun, the integrated accelerating field in this C-band gun will be exactly the same of a UCLA/BNL/SLAC 1.6 cells S-band one operating at 120 MV/m.

From the Wang criterion in equation 3.3 fixing the β of the cavity, by an increase of the RF frequency it is possible to increase the peak electric field before a breakdown occurs. As also we have seen in the previous section, increasing the frequency it is possible to reduce the pulse length and so by doubling the RF frequency it is possible to reach higher accelerating field. Besides, searching for an higher frequency, the C-band technology nowadays is better known and less challenging compared to the X-band one. Furthermore a C-band gun can be integrated with an high gradient C-band linac, maintaining also the possibility to correct the longitudinal emittance

using an higher frequency X-band structure after the gun[48].

In collaboration with UCLA, SLAC, LANL we are developing an RF gun that takes advantage from an higher RF frequency of 5.712 GHz. We assume to reach a peak field of $240MV/m$, using for example cryogenic temperatures as in the previous section, and we are interested in beam dynamics studies to investigate the advantages of that gun.

3.3.1 Gun parameters and starting point for the optimization

I studied the perspectives on achievable beam quality and beam brightness using this high gradient C-band gun. Taking into account a relatively high charge beam of $Q = 100pC$, the parameters to be set are the laser parameters, the starting RF phase in order to have the beam on the wave crest at the gun exit, an optimal design for the solenoid that compensate the emittance reducing also the fringe field on the cathode surface, the solenoid magnetic field and by the beam plasma oscillations the optimal position for the first linac structure.

The working point was optimized to immediately control the beam space charge forces and compensate the emittance along the linac. For final emittance values in the nanometers scale, can be also relevant the contribution from the magnetization emittance i.e. the contribution to the emittance that came from the residual solenoid field on the cathode surface that gives to the particles an angular momenta.

A residual solenoid magnetic field on the cathode surface can generate a transverse momentum to the emitted particles with the net effect to increase the bunch emittance (see Ref. [50]). This so called magnetization emittance term can be estimated with the Busch's theorem. In fact upon particles leaving field they have an rms transverse momentum

$$\sigma_{p\perp} \cong \frac{qB_0}{2}\sigma_x. \quad (3.11)$$

This can be translated to a normalized transverse emittance contribution of

$$\epsilon_{n,magn} \approx \frac{\sigma_{p\perp}}{mc}\sigma_x \cong \frac{qB_0}{2mc}\sigma_x^2. \quad (3.12)$$

Simplifying the formula we obtain

$$\epsilon_{n,magn}(mm \ mrad) \approx 0.3B_0(mT)\sigma_x^2(mm^2). \quad (3.13)$$

At the end of the optimization, it is important to evaluate how much is the magnetization emittance contribution to the final normalized rms transverse emittance.

I have simulated with GPT such gun, the solenoid and in order to boost the energy up to 150 MeV I inserted two TW C-band structures as the SPARC_LAB ones (see

Ref.[51]). The magnetic and electric field maps have been made running SUPER-FISH.

After a conditioning phase at SPARC_LAB, the peak accelerating gradient of these TW C-band structure was 36 MV/m, operating with a repetition rate of 10 Hz, a pulse length of 165 ns, an input power in the structures of 38 MW and obtaining a breakdown rate lower than 2×10^{-5} breakdowns/ms (see Ref [51]).

Another recent result obtained at SACLA push the peak accelerating gradient for a TW C-band structure over the 50 MV/m (see Ref. [52]). To push the beam exactly to 150 MeV and to make the photoinjector more compact, I increase the accelerating gradient up to 57 MV/m.

Since in the LCLS S-band gun particles are accelerated to the same energy of the C-band high gradient gun, as a starting point I considered the attempt to optimize the S-band LCLS photoinjector to lower charge. In fact this photoinjector was optimized to work with a very high charge beam of 1 nC (see Ref. [53], [21]), but nowadays it works with relatively lower charge, typically 250 pC as in Ref. [4]. An attempt to optimize the LCLS photoinjector to lower charges was done using a genetic optimizer and the beam dynamics was simulated with ASTRA in Ref. [54]. The investigation was done to optimize the injector layout by varying the bunch charge in the range 0 – 1 nC and simulating a gaussian transverse laser profile on cathode and a longitudinal flat top.

The results show that for lower charge the optimized position of the first linac structure increases, up to reach a distance of around 2.5 m for a 100 pC beam. This is because lower charges correspond to lower electron densities and to lower plasma frequencies. An emittance optimization varying the bunch length with different shapes was done, fixing the bunch charge to 200pC. It shows the possibility to reach the 95% projected emittance value of about $0.1\mu\text{m}$ (reaching the intrinsic emittance) using a flat top shape rms bunch length of about 1 mm.

To increase at maximum the beam peak brightness we need to achieve the photoemission saturation i.e. maximum charge extraction per unit of area, making the space charge forces at the extraction of the same order of the accelerating RF electric field. In this regime the saturation charge for a cigar beam corresponds to (see Ref.[46])

$$Q_{sat} = \frac{\sqrt{2}}{9} I_A \left(\frac{eER}{mc^2} \right)^{\frac{3}{2}} t_{laser} \quad (3.14)$$

where $E = E_0 \sin\phi$ is the electric field at the cathode surface, R is the laser radius and t_{laser} is the laser duration. The transverse dimension in the cigar regime requires (see Ref. [46])

$$R < \frac{t_{laser}^2 e E_0}{2m}. \quad (3.15)$$

By the 200 pC S-band optimization, the optimal beam and laser parameters are: the FWHM laser duration has to be about 12 ps and a laser radius from equation 3.15 of about 0.25 mm. Simulations show that at the injector exit for a 200 pC beam the maximum cathode brightness is reached in the cigar regime and not for the pancake one.

3.3.2 High gradient C-band gun optimization

Taking advantage from the genetic optimization in the previous subsection, I search for a completely new working point in a C-band gun with a peak field of 240 MV/m. Considering that the peak field on the cathode surface is double respect the S-band 120 MV/m scenario, as a starting point I scale the laser parameters to the higher peak field, according to the charge saturation equation 3.14 in the cigar regime. The transverse beam dimension was scaled following the equation 3.15. Of course this is a starting point because the genetic optimization considered a different peak field on the cathode surface, in fact as we will see in the next section the optimal injection phase ϕ_0 leads to a little higher field on the cathode surface compared to the double one that we expect. Furthermore the genetic optimization was done using only 10k macro particles.

The layout that I have simulated in GPT is made up by the cathode inserted in the high gradient 1.6 cells C-band with a peak field of 240 MV/m, the electric field map was done running SUPERFISH and the result is in Figure 3.20.

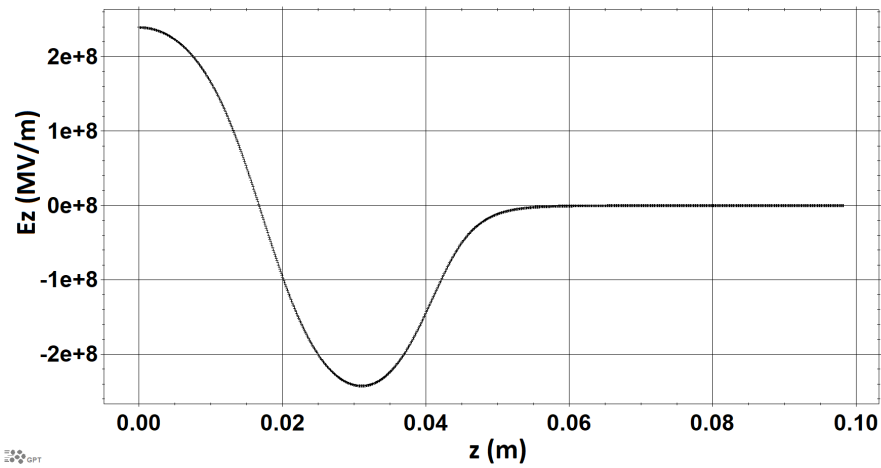


Figure 3.20. Field map for the longitudinal electric peak field E_z used in GPT simulations for the 1.6 cells C-band gun. The peak field is set to $240\text{MV}/\text{m}$. In $z = 0\text{ m}$ is placed the cathode, the photoemission process with Schottky effect is simulated including space charge forces effects.

To compensate the emittance I used the design of the solenoid that will substitute the present one at SPARC_LAB. This solenoid was designed for the SPARC_LAB

3.3. HIGH GRADIENT, HIGHER FREQUENCY AND ULTRA-HIGH BRIGHTNESS C-BAND GUN87

S-band gun and is made by two coils and will reduce the magnetic field on the cathode up to 3.6 G supplying the coil with 150 A. The current in the coils was varied, optimizing the magnetic field to reduce the beam emittance. The design of that solenoid was optimized to minimize the residual magnetic field on the cathode surface, has a reduced length of 174 mm and a bore diameter of 76 mm. The project parameters are reported in Figure 3.21. In order to adapt this S-band design to the C-band gun the magnetic field maps were obtained running SUPERFISH, reducing the length of a factor two and doubling the magnetic field with respect to the S-band case.

	INPUT DATA		OUTPUT	
IRON YOKE DATA	Lenght (mm)	174.00	B(T)	0.2335
	Bore Diameter (mm)	76	I(A)	150
	End Plate Thickness (mm)	24	Lmag (mm)	250.00
	Number of inner separation septum	1	IB(T m)	5.84E-02
	Inner separation septum diameter (mm)	82		
	Inner separation septum thickness (mm)	28		
	Iron shield thickness (mm)	24		
	Mag En. (J)	140		
Rise current time (ms)	10000			
COIL DIMENSION & ELECTRICAL INTERFACE	N*I (Ampere*Turns)	28800	Height Z cross section (mm)	35.00
	N (number of coils)	2	Width R cross section (mm)	90.00
	N (tums per coil)	96	L cond (m)	0.62
	Coil inner diameter	106	J (A/mm ²)	7.47
	Coil width R (number of turns)	6	Jsimulation (A/mm ²)	4.571
	Coil height Z (number of tums)	16	Rtot (Ω)	0.118
	Width single conductor (mm)	5	L (mH)	0.012
	Height single conductor (mm)	5	Votage (V)	17.84
	Conductor hole diameter (mm)	2.5	Power (kVA)	2.7
	Scond (mm ²)	20.09		
	Shole (mm ²)	4.91		
ρ @60°C (Ω*mm ² /m)	0.02			
WATER COOLING	Number of pancake per pole	3	Thermal loss per pancake (W)	441.3
	Number of Tum per pancake (Z)	2	Water flow pancake (l/s)	0.007
	Number of Tum per pancake (R)	16	Water flow TOTAL (l/s)	0.042
	ΔT water (°C)	15	Water velocity (m/s)	1.43
	h (m/m)	1.88	H (m)	37.06
			ΔP (bar)	3.71

Figure 3.21. Project parameters for the new solenoid at SPARC_LAB, that is able to reduce the magnetic field on the cathode surface up to 3.6 G powering the two coils with opposite direction currents of 150 A.

After a drift where the beam plasma oscillations occur the first TW C-band structure is located. This structure is composed by 81 cells and is about 1.4 m long, with an accelerating gradient of 57 MV/m. After another drift of 0.2 m, a second C-band structure starts.

The RF launch phase ϕ_0 in the gun is set to minimize the RF contribution to the transverse emittance. From the equation 2.31 it happens when the beam exits the

gun in a RF phase of $\phi = \pi/2$. The RF phases in the accelerating sections are set to maximize the beam energy.

In figure 3.22 is reported the solenoid magnetic field map obtained running SUPERFISH and imported in GPT, using a current that flows in the same direction in the coils.

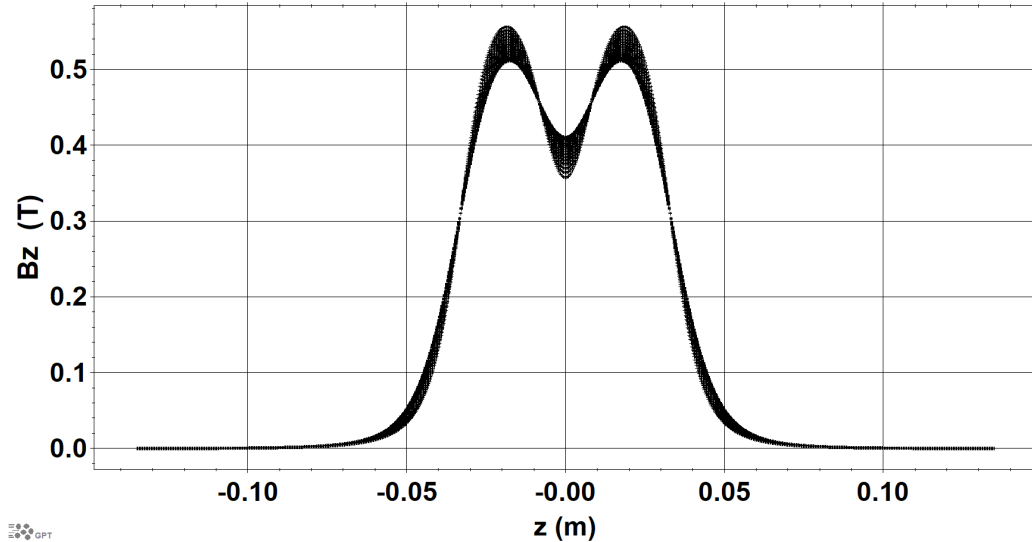


Figure 3.22. Trend of the longitudinal magnetic field in the solenoid, supplying the coils with a current of $I = 150$ A flowing in the same direction.

Furthermore multiple scans with 30k macro particles in GPT were performed in order to optimize different parameters. The first ones are the laser parameters, according to the saturation charge in the cigar regime, optimal transverse and longitudinal parameters were found to maximize the beam brightness. Furthermore the first accelerating section was moved in different longitudinal positions to optimize the beam injection performing an emittance compensation, as was in the case of the Ferrario working point for the S-band gun in Ref [21].

3.3.3 High gradient C-band gun working point

Once the previous optimizations have led to an emittance minimum at the linac end, all the parameters have been re-optimized in a lower variability range using a higher number of 100k macro particles. Finally the optimized working point has been tested with a larger number of particles of 350k macro particles, and parameters have been re-optimized in an even smaller variability range.

I present the final optimized working point simulated with 350k macro particles. With a charge of $Q = 100$ pC the laser on cathode has the following parameters: the laser duration is a flat top of 5.8 ps, a gaussian transverse shape of $\sigma_x = 151\mu m$, the

3.3. HIGH GRADIENT, HIGHER FREQUENCY AND ULTRA-HIGH BRIGHTNESS C-BAND GUN89

laser energy was set to 4.66 eV corresponding to a $\lambda_l = 266.7nm$. The optimal launch phase is $\phi_0 = 38^\circ$ that correspond to an extraction phase from the gun of $\approx \pi/2$. The field on the cathode surface is $E_0 \sin \phi_0 \approx 145MV/m$, that is more than a factor two respect the 120 MV/m S-band gun using a $\phi_0 \approx 30^\circ$. The intrinsic emittance of this cigar beam was set to $\epsilon_{intrinsic} = 25nm$. The current in the coils is set to 117 A, leading to an increase of the magnetic field of a factor two compared to the one in Figure 3.22. The optimal longitudinal position for the first C-band section was set to $z = 1.02$ m. The longitudinal beam phase space after the gun is reported in Figure 3.23.

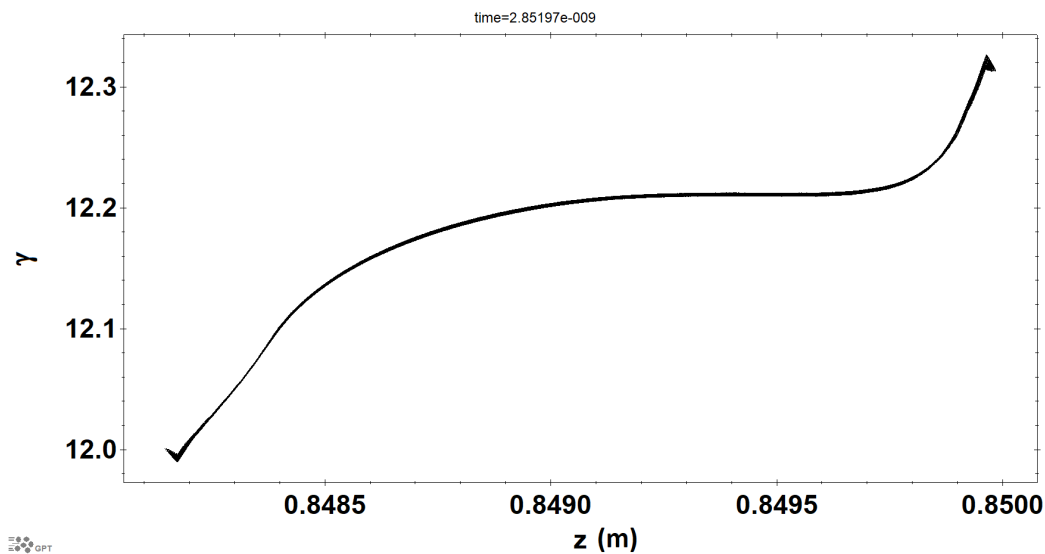


Figure 3.23. Beam phase space before the first accelerating structure. On the x axis are reported the particle longitudinal positions z (m) and in the y axis there are the Lorentz's gamma factors.

In Figure 3.24 are reported trends of the beam energy E (MeV) and beam energy spread σ_E (MeV) along the photoinjector.

The final beam energy is $E \approx 150$ MeV, and the normalized energy spread σ_E/E is about 0.2%. Due to the long bunch length and since the output of simulation is in time, the bunch entering and exiting sections generate a step in the energy spread trend. In order to avoid inaccurate solutions of the particle motion, the maximum step size integration was set to 5×10^{-14} s.

Trends of the rms normalized transverse emittance $\epsilon_{n,rms}$ and of the spot size σ_x are reported in Figure 3.25. As shown the beam is injected in the first C-band section in the transverse beam waist, that correspond to a relative maximum of the emittance. In this way the second emittance minimum is reached at the photoinjector end, it means the transverse emittance is compensated. The final transverse emittance value is $\epsilon_{n,rms} \approx 55nm$.

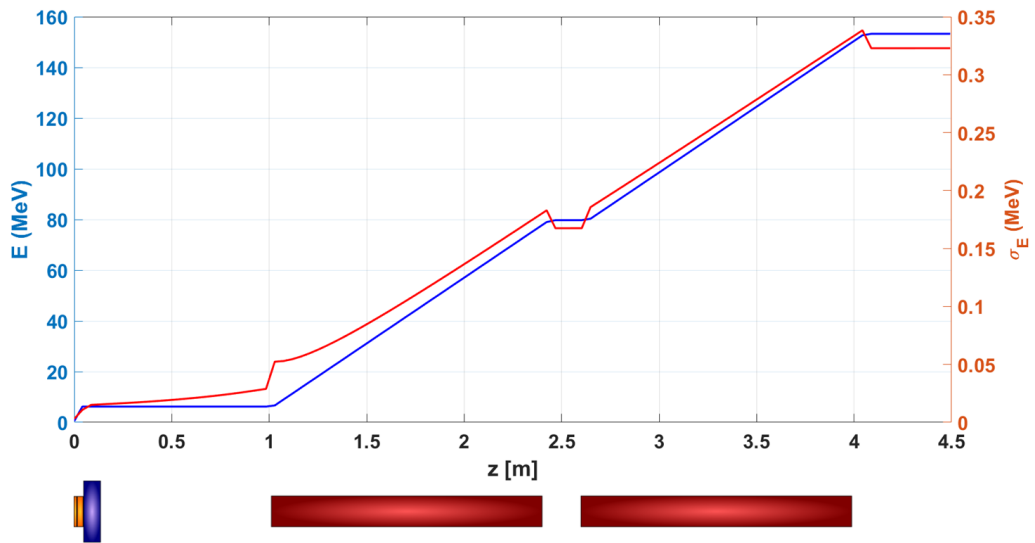


Figure 3.24. Trends of the beam energy and beam energy spread along the photoinjector. In blu is reported the energy growth, and the red line is the relative energy spread, where σ_E is the rms beam energy distribution. The normalized energy spread σ_E/E at the photoinjector end is about 0.2%. Below is reported the photoinjector layout. From the left: RF 1.6 C-band cells, solenoid, two C-band structures.

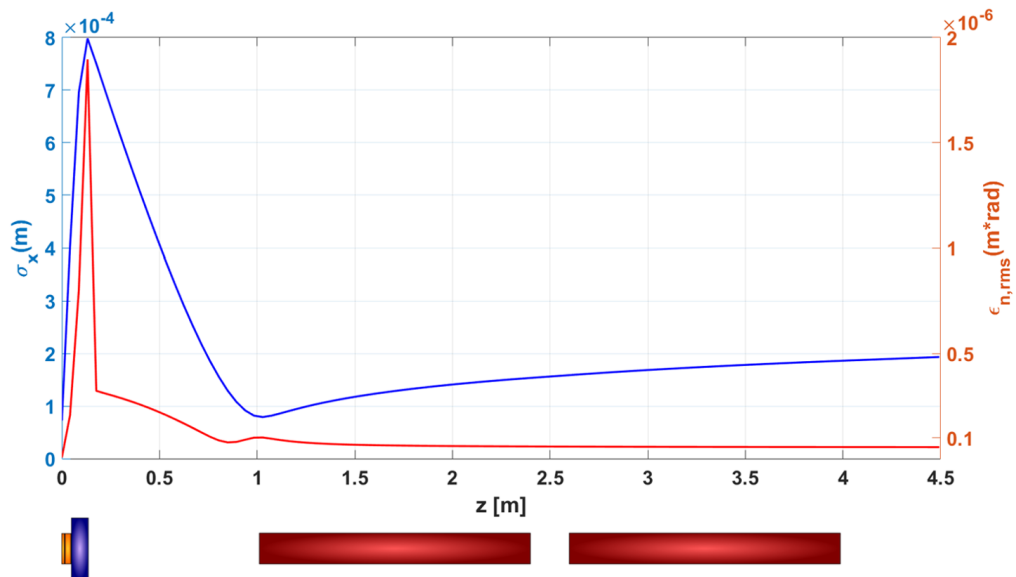


Figure 3.25. Evolution along the photoinjector of the spot size σ_x in blu and of the normalized rms transverse emittance $\epsilon_{n,rms}$ in red. Below is reported the photoinjector layout.

3.3. HIGH GRADIENT, HIGHER FREQUENCY AND ULTRA-HIGH BRIGHTNESS C-BAND GUN91

Figure 3.26 shows the evolution of the rms bunch length during acceleration along the photoinjector, after the photoemission process there is an initial elongation due to the space charge forces. This process continues slower until the bunch enter the first accelerating structure, where the beam becomes relativistic and space charge effects diminish rapidly.

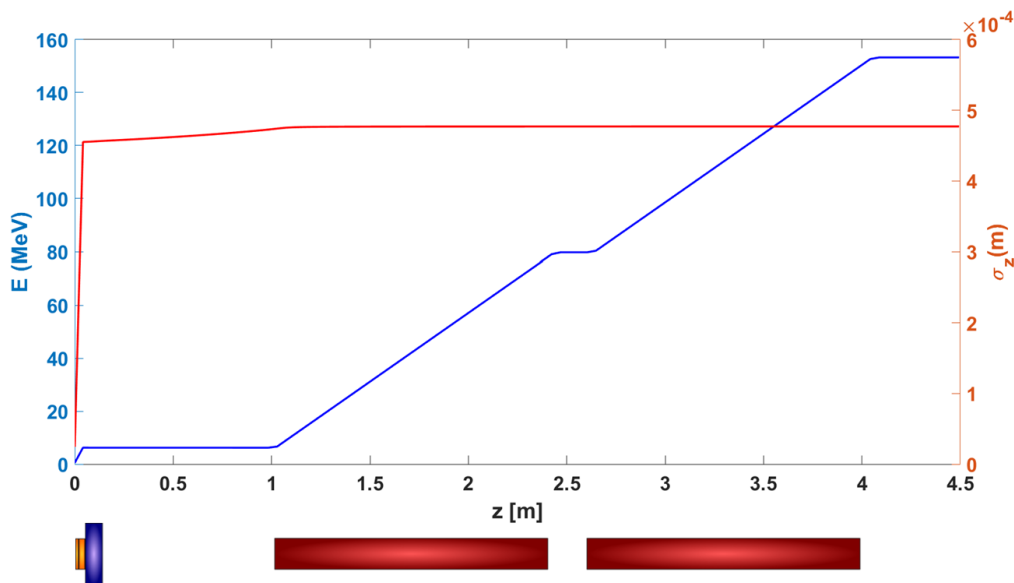


Figure 3.26. Evolution along the photoinjector of the bunch length σ_z (m) in red, and of the bunch energy E (MeV) in blu. Below is reported the photoinjector layout.

The final rms bunch length is $\sigma_{z,rms} \approx 4.7 \times 10^{-4}$ m that corresponds to ≈ 1.5 ps and to a peak current of $I \approx 64.1$ A. This leads to a final brightness of $B = 2I/\epsilon_{n,rms}^2 \approx 4.2 \times 10^{16} A/m^2$. Considering the final particle distribution in Figure 3.27 we can obtain a FWHM bunch length that leads to a final beam brightness of $B_{FWHM} \approx 5.1 \times 10^{16} A/m^2$.

Transverse and longitudinal beam phase spaces at the photoinjector end ($z \approx 4.5$ m) are reported respectively in Figure 3.28 and in Figure 3.29.

Using the simplified equation 3.13 we can estimate the magnetization emittance, the solenoid used in the simulation was powered with $I = 177$ A this leads to a residual magnetic field on the cathode surface of $B = 0.83$ mT, using the transverse laser spot of $151 \mu\text{m}$ we obtain a magnetization emittance contribution of $\epsilon_{n,magn} \approx 5.7$ nm. Summing in quadrature this term to the final emittance means that is a negligible contribution.

A solenoid field map with no residual magnetic field on the cathode surface was produced with SUPERFISH and another optimization of the working point was performed with GPT, leading to about the same final emittance value of 55 nm.

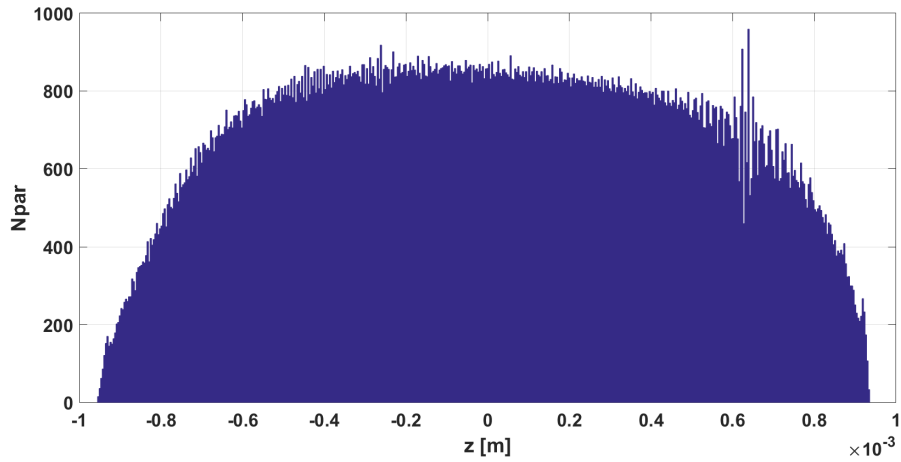


Figure 3.27. Particle beam distribution at the end of the photoinjector. In the x axis there are the longitudinal particle coordinates, where $z = 0$ m is set at the bunch center. In the y axis there is the number of the particles for each bin.

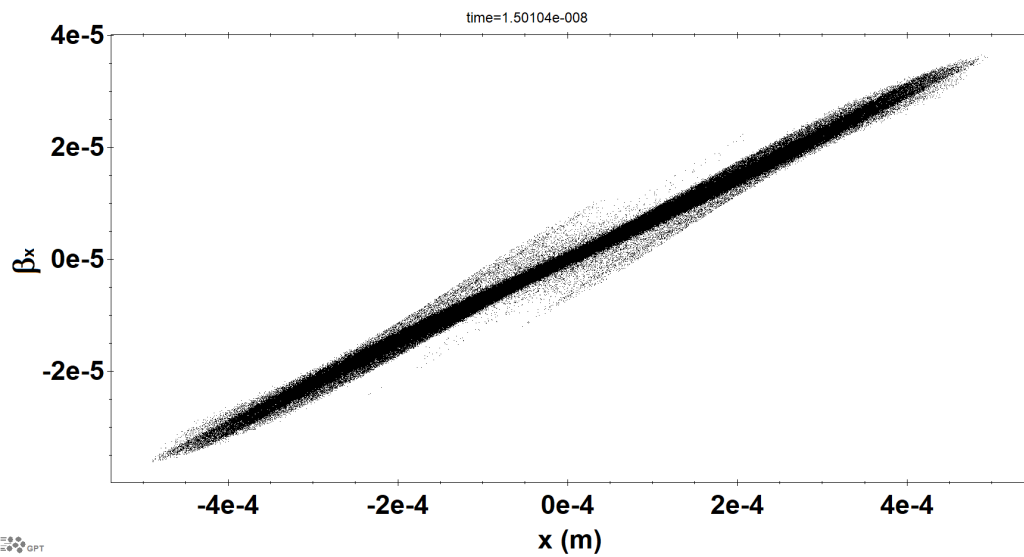


Figure 3.28. Beam transverse phase space at the photoinjector end. In the x axis are reported transverse particle positions while in the y axis are reported the transverse velocities normalized by the speed of light.

3.3. HIGH GRADIENT, HIGHER FREQUENCY AND ULTRA-HIGH BRIGHTNESS C-BAND GUN93

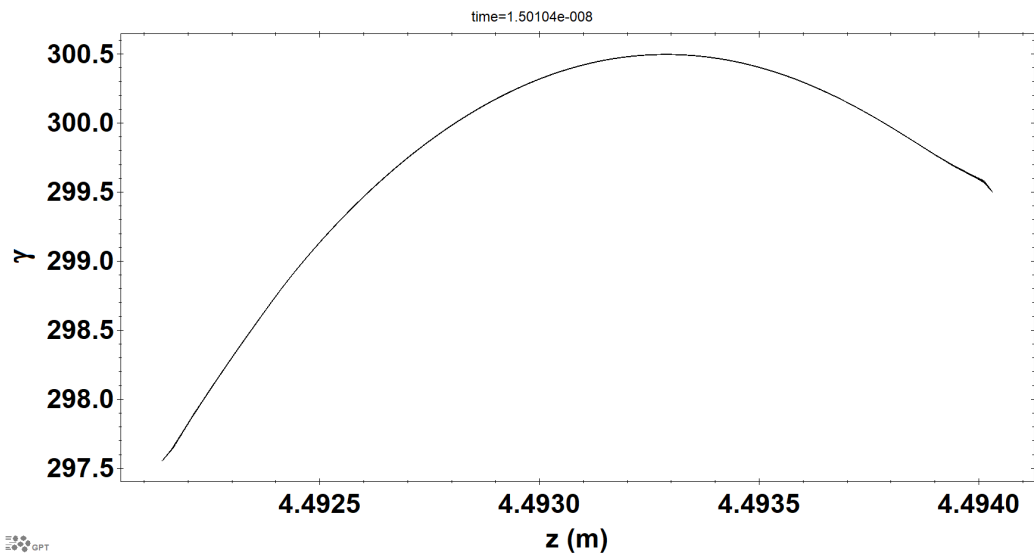


Figure 3.29. Beam longitudinal phase space at the photoinjector end. In the horizontal axis are reported longitudinal particle positions while in the vertical axis are reported the Lorentz's gamma factors.

This means that using this solenoid no bucking coils are necessary to reduce the magnetic field on the cathode surface.

3.4 A possible SPARC_LAB upgrade

Recently there was a proposal to upgrade SPARC_LAB with a new linear accelerator able to push the beam energy over the GeV scale. The proposal will bring to built a new facility called EUSPARC, and it will realized in the framework of the project European Plasma Research Accelerator with eXcellence In Applications (EUPRAXIA) and the european project Compact Light. Eupraxia will be a new infrastructure that envisages the realization of a new user facility that will add the plasma acceleration to the RF technology, and will produce coherent light for users with an FEL. The requests of the EUSPARC and EUPRAXIA projects are very similar in terms of beam parameters produced by the RF linac.

Both facility requires an high quality beam produced by a compact high gradient RF accelerator, up to reach a final beam energy of about 1 – 1.5 GeV. Once extracted from the conventional accelerator the beam will be injected in a plasma channel, where stronger accelerating field (of the order of GV/m) will push the beam energy up to 3 GeV. After the plasma channel this high energy and high quality beam will be send to an FEL to produce light with a wavelength of the order of about 3 nm to study for example ultrafast processes in the so-called water window.

Some parameters on plasma channel and on the FEL device are under study considering different cases. The beam parameters produced by the conventional RF accelerator are quite fixed considering a witness beam of 30 pC. The higher gradient RF accelerating structures will be probably X-bands (11.424 GHz) with a gradient over 70 MV/m, to reach a final energy of about 1 – 1.5 GeV. The required peak current is 3 kA, i.e. a rms bunch length of $3\mu\text{m}$, with an rms energy spread lower than 1%. The final rms normalized transverse emittance must not exceed $1\mu\text{m}$.

In order to test the performances of the high gradient C-band gun in these contests I have designed a possible beam line using GPT. It is a very preliminary test in which I used three different RF frequencies in the linac. The photoinjector is made by a C-band gun followed by three S-band sections (each ones is 3 m long with an accelerating gradient of 20 MV/m). The three S-band structures are embedded in solenoids to control the beam transverse shape during the velocity bunching. As a starting point the blowout regime [44] was used to reach an higher peak current. The optimization for laser parameters, solenoid magnetic field and the position of the first accelerating section was performed as in the previous section, but to reach the peak current of 3 kA minimizing also the transverse emittance.

The final laser parameters are: a gaussian bunch length of 21 fs with a truncation at 1.5 sigma, a gaussian transverse spot of $175\mu\text{m}$, using a laser energy of 4.66 eV. The optimized launch phase was set to $\phi_{launch} = 33^\circ$ that leads to an electric field on the cathode surface of $E_0 \sin\phi_0 \approx 130 \text{ MV/m}$. The first accelerating section starts

at $z = 0.77$ m

The phases of the first two S-band sections are optimized to compress the beam as much as possible, using the velocity bunching. In order to strongly compress the bunch two phases are optimized to perform both velocity bunching and also to create an energy chirp in the phase space i.e. a proper spatial energy correlation between head and tail. After the second section the bunch is drifted in vacuum for 73 cm in order perform a ballistic bunching, transforming the spatial energy correlation into spatial compression. This further compression allows to compress even more avoiding an emittance growth. The beam phase space before the first accelerating section is reported in Figure 3.30.

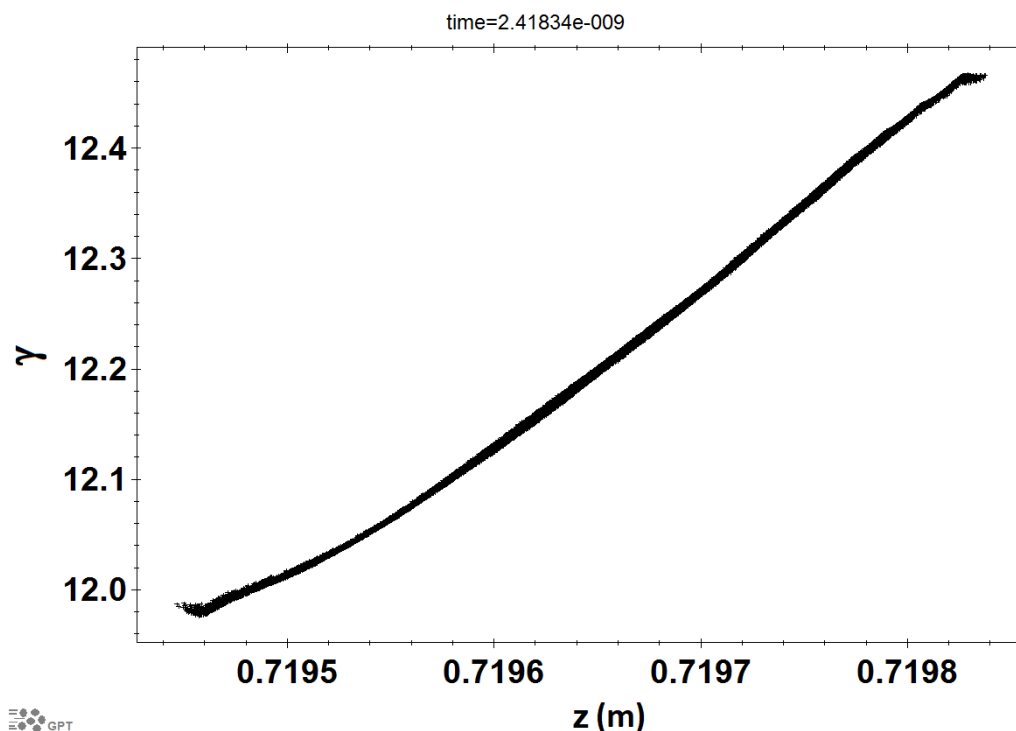


Figure 3.30. Beam phase space before the first accelerating section.

Due to the bunch position on the RF wave, during the velocity bunching the phase space inside the first accelerating section starts to rotate as in Figure 3.31.

Figure 3.32 shows the spatial energy correlation along the bunch at the end of the first accelerating section. Having the bunch tail an higher energy compared to the bunch head, the spatial energy correlation becomes a spatial compression along the drift so that the bunch is further compressed.

Up to the end of the ballistic bunching the bunch compression is performed avoiding bunch particles cross over in the so called laminar velocity bunching regime, as discussed by Bacci in Ref. [55], so that the bunch has reached the maximum

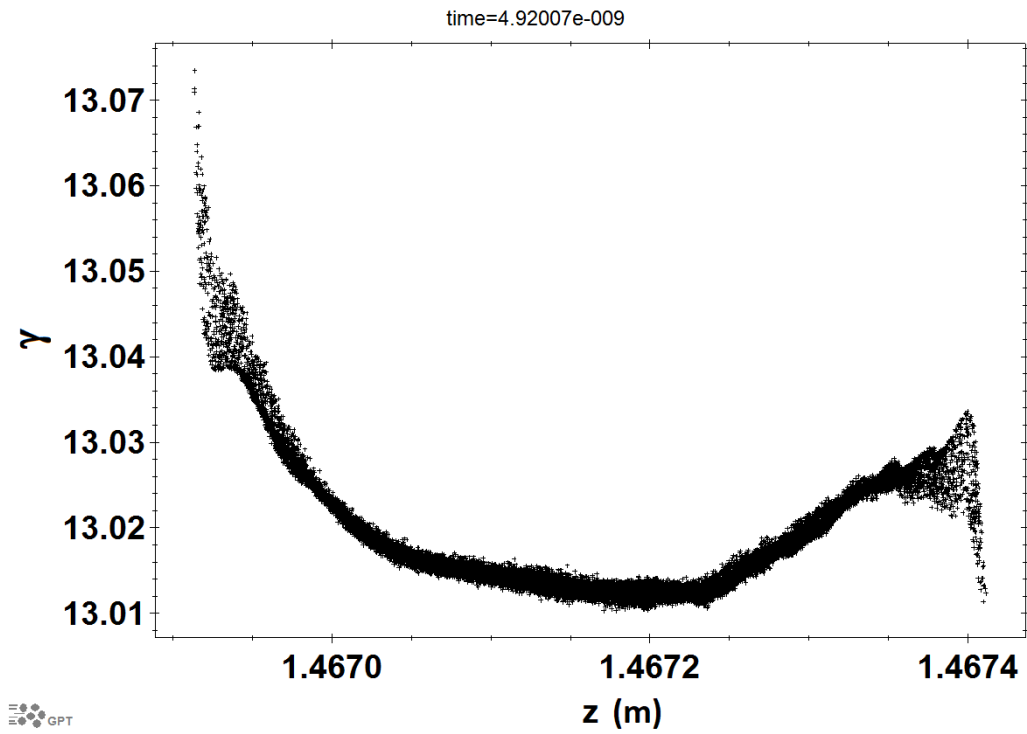


Figure 3.31. Beam phase space during the velocity bunching in the first accelerating section. The phase space is rotating to start the bunch compression.

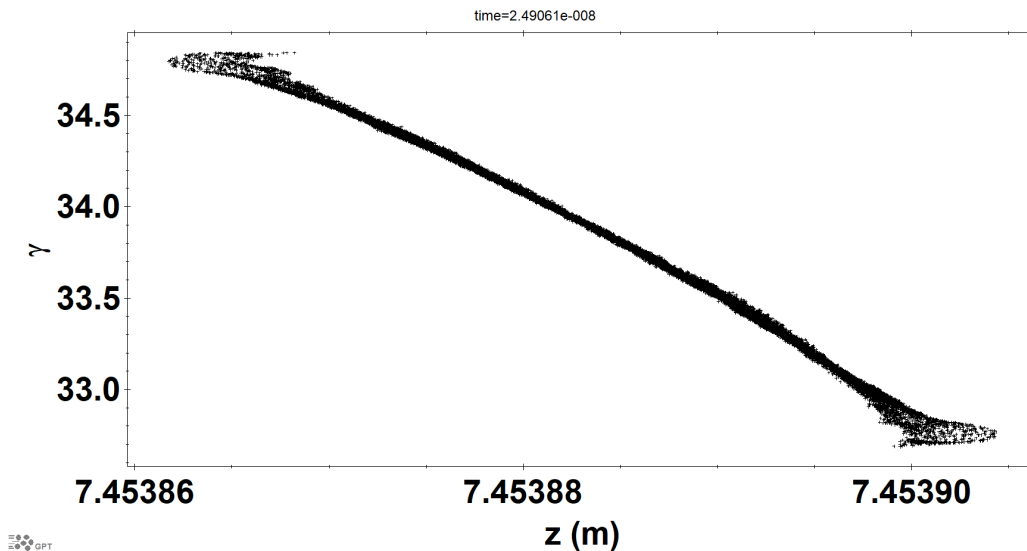


Figure 3.32. Beam phase space at end of the second velocity bunching stage where the beam is yet RF compressed and presents a spatial energy correlation.

compression. The phase of the third accelerating section is set on the wave crest, and this structure is located where the bunch maximum compression occurs, reducing the decompression due to the space charge forces. The optimized drift between the second and the third section is 73 cm.

Varying the bunch charge the drift space necessary to perform the ballistic bunching may vary, so that it can be useful to fill the drift space with SW cells, so that they can ON/OFF separately depending by the bunch longitudinal waist.

Figure 3.33 shows the phase space at the end of the photoinjector where the beam has reached ≈ 75 MeV.

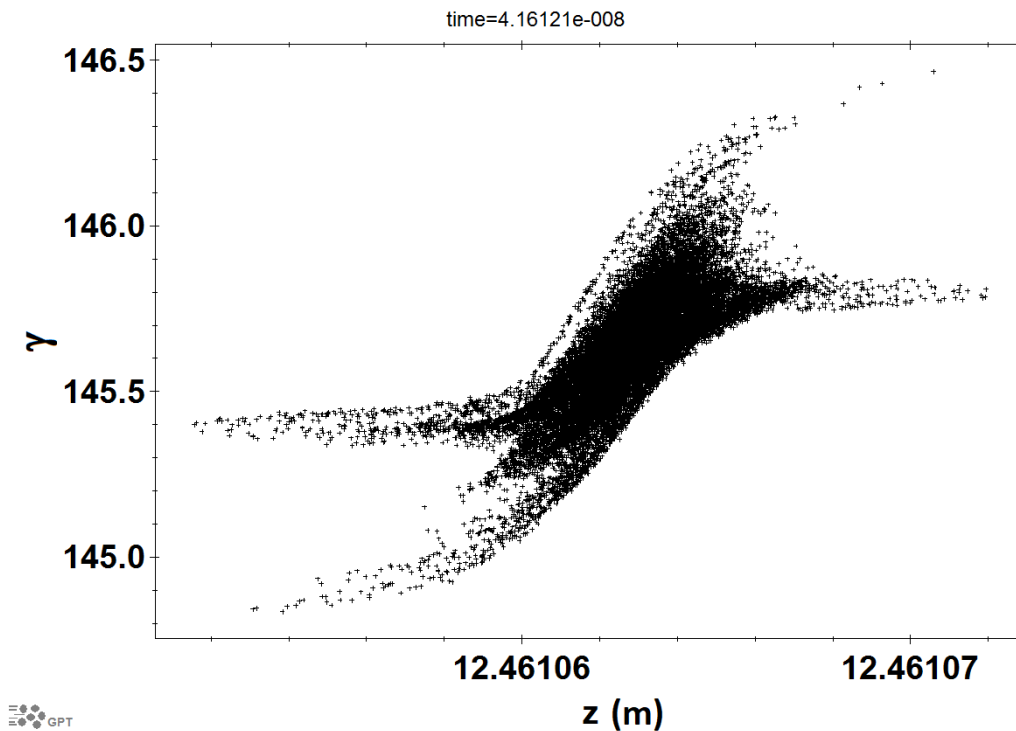


Figure 3.33. Beam phase space at end of the photoinjector where the beam has reached the maximum compression and an energy of ≈ 75 MeV.

The X-band booster is made by 24 X-band modules, each module has 70 cells and a total length of 62 cm, the accelerating gradient is $70\text{MV}/\text{m}$. The distance between each module is alternated to 20 cm and 30 cm in order to insert diagnostics. Figure 3.34 shows trends of the beam energy and of the beam energy spread along the linac.

Figure 3.35 shows trends of the rms bunch length $\sigma_{z,rms}$ (m) along the linac and of the relative rms peak current I (A). The final rms bunch length is $2.6 \mu\text{m}$ that leads to a peak current of about ≈ 3.5 kA.

The beam energy at the linac end is about 1.1 GeV and the normalized energy spread σ_E/E is about 0.1%.

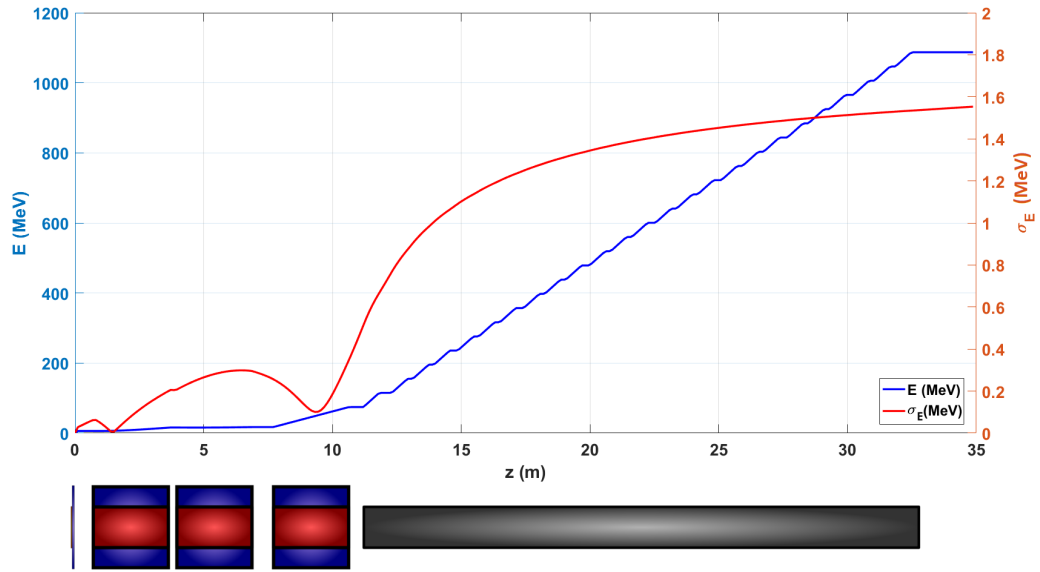


Figure 3.34. Trends of the beam energy E (MeV) and of the beam energy spread σ_E (MeV) along the linac. The final beam energy is about 1.1 GeV and the final normalized energy spread σ_E/E is about 0.1%. Below is reported the linac layout. From the left: RF 1.6 C-band cells, solenoid, three S-band structures surrounded by solenoid and the black section represents the 24 X-band modules.

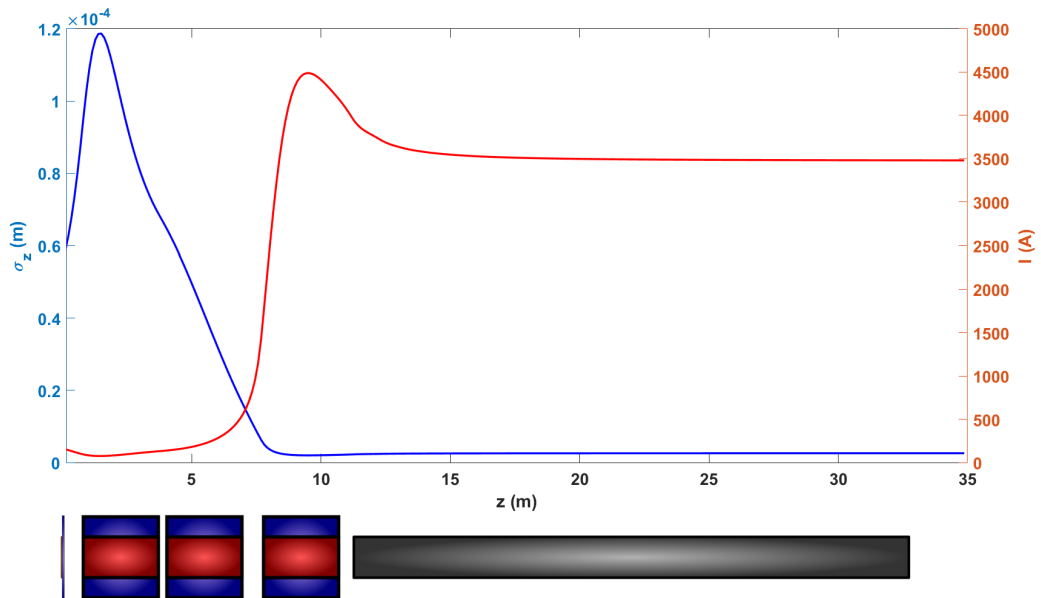


Figure 3.35. Trends of the rms bunch length $\sigma_{z,rms}$ (m) along the linac and of the relative rms peak current I (A). Below is reported the linac layout. From the left: RF 1.6 C-band cells, solenoid, three S-band structures surrounded by solenoid and the black section represents the 24 X-band modules.

Figure 3.36 shows trends of the beam emittance and of the beam spot size, the final emittance is ≈ 280 nm that leads to a rms beam brightness of about $B \approx 9 \times 10^{16}$ A/m². By this figure is evident that the second section solenoid generates plasma oscillations in the bunch. At this point the bunch behavior presents the same characteristic that we expect at the gun exit, but with an higher plasma frequency. From these consideration the X-band booster starts in the relative maximum of the emittance, corresponding to the beam waist, so that the emittance is well compensated along all the X-band linac.

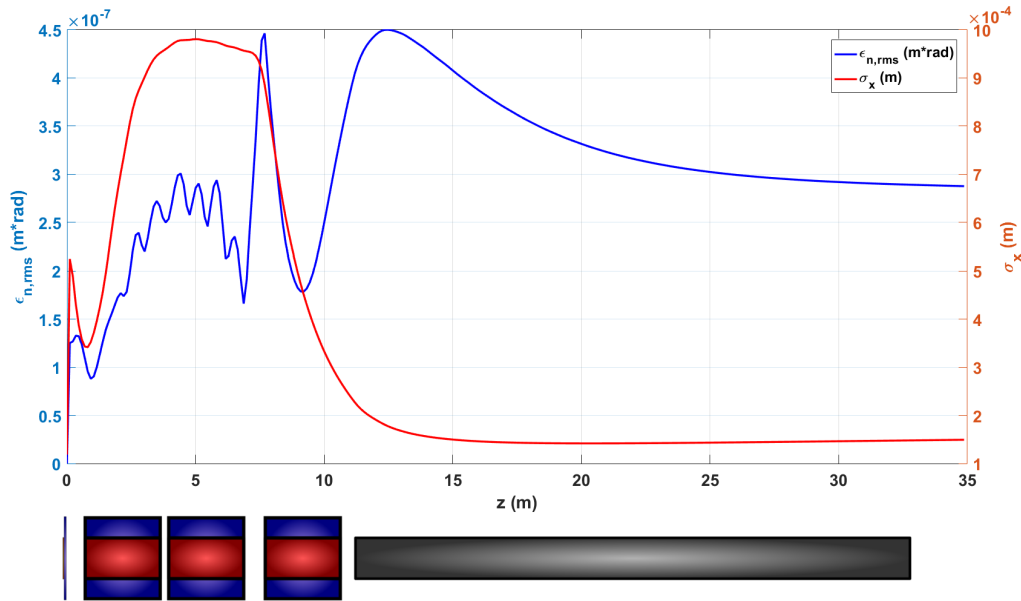


Figure 3.36. Trends of the normalized rms emittance $\epsilon_{n,rms}$ (m rad) along the linac and of the rms beam spot size σ_x (m). Below is reported the linac layout. From the left: RF 1.6 C-band cells, solenoid, three S-band structures surrounded by solenoid and the black section represents the 24 X-band modules.

Considering that the final ≈ 1 GeV beam will be injected in the FEL to produce photons with wavelength of 3 nm, we have to consider for the final beam a slice length of $\approx 0.6 \mu\text{m}$. In Figure 3.37 is reported an histogram of the particle beam distribution at the end of the linac, in which each bin has a length of $\approx 0.8 \mu\text{m}$ so that each bin can represent a beam slice. Considering the slice with more particle, it has a charge of 3.3 pC that leads to a slice peak current of $I_s = 1.3$ kA.

Currently is under test in this linac layout a cigar shaped bunch, instead of the blowout regime and a photoinjector with only one frequency (C-band) followed by the X-band booster.

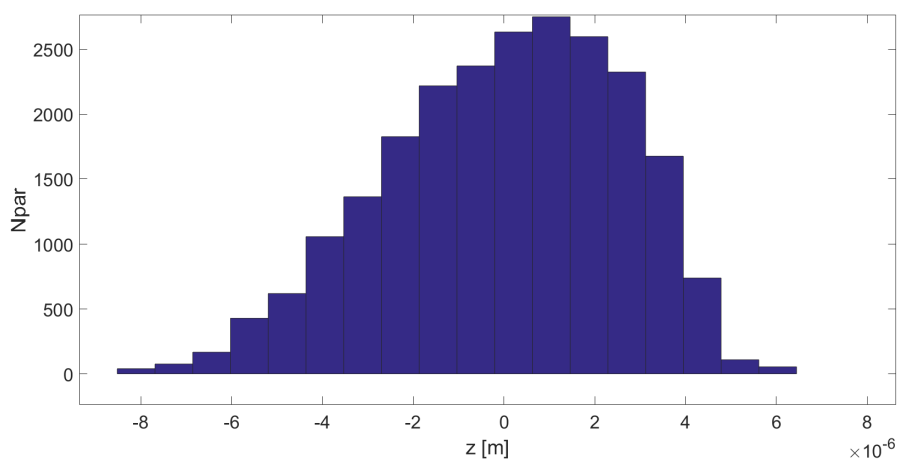


Figure 3.37. Particle beam distribution at the end of the linac. In the y axis there is the number of the particles for each bin. The length of each bin is set to be equal to the slice length.

Chapter 4

SPARC_LAB Photoinjector optimizations

The generation of high brightness electron beams by RF photoinjector allowed the realization of a large variety of FEL. One of the fundamental parameter to keep under control in the creation of high brightness electron beams, in order to preserve the beam quality, is the beam emittance.

As seen an RF photoinjector is composed by an RF gun followed by accelerating sections that push the beam to a relativistic energies where the space charge effects are not anymore relevant. Furthermore as we have seen in the previous chapter, it is fundamental the use of a solenoid at the gun exit in order to control the space charge force effects and to compensate the beam emittance.

The alignment of that solenoid with the beam line is a key point in order to avoid possible kicks of the beam. In fact in an region where the beam has a low rigidity, one of the effects of a misaligned solenoid is a kick of the beam, with the consequent use of steering magnets and a consequent emittance growth. As it shown in this chapter another effect of an off-axis solenoid field on the beam is to produce different beam spot sizes on the two transverse planes x and y (asymmetric beam).

When the beam is injected in a plasma channel to perform plasma acceleration, very stringent beam transverse matching conditions are requested. As it happens at SPARC_LAB, the beam final focus can be produced using high gradient (520 T/m) permanent magnet quadrupoles. If the beam transverse shape is far from a circular profile it will be very difficult to match simultaneously the transverse beam spot sizes. In fact when a beam enters in a triplet of quadrupoles with different sizes in transverse planes, these two different spot sizes perceive a different magnetic field in the quadrupoles resulting in different beam transverse waists in different longitudinal positions.

For example considering the SPARC_LAB beam, the transverse matching conditions

are of the order of $2 - 3\mu\text{m}$ using a plasma density of $n_0 = 10^{16}\text{cm}^{-3}$, a transverse normalized emittance less than $1\mu\text{m}$ and a bunch energy of about 130 MeV. By this very stringent transverse matching conditions it is fundamental to have equal spot sizes to perform an equal focusing in both planes.

By machine operations at SPARC_LAB the effects of the gun solenoid misalignments, like offset and different beam shapes after the gun solenoid are evident, so that we are forced to use orbit correctors after the gun. Considering that the coils of the SPARC_LAB solenoid are powered with a current that flows in opposite directions in order to avoid particle rotations, I developed an algorithm to study the misalignments for a solenoid that works in this opposite current configuration.

A dedicated experimental run was performed to acquire the beam spot sizes and the centroid positions in the flag before the first accelerating section, varying the currents in the coils of the gun solenoid. Using GPT and applying this algorithm, the vertical and horizontal misalignments were found, and the experimental data were reproduced. The found misalignments are about ≈ 1 mm in the horizontal plane x and ≈ 0.5 mm in the vertical plane y . By GPT simulations aligning the solenoid to these value we can improve the orbit displacement of 99.4%.

Considering also that possible beam kicks are generated by laser on cathode misalignments, residual solenoid misalignments or accelerating section misalignments, the beam can still arrive in the final focus with different spot sizes. To create a bunch as near as possible to a circular shape, I studied the possibility to insert Printed Circuit (PC) skew quadrupoles inside the gun solenoid. By GPT simulation creating a 100 pC bunch with a difference in spot sizes of about 14%, using these devices, it will be possible to reduce the differences in the shape up to 1%, reducing also the difference in the emittances in the two transverse planes from 14% up to $\approx 5\%$. After these simulation results, is under study the possibility to insert these devices in the new SPARC_LAB solenoid, described in the previous chapter, that will replace the present one.

4.1 Particle motion in a solenoid

The beam focusing in a solenoid is due to the coupling of particle velocities \vec{v} with the component \vec{B}_\perp of the magnetic fringe field and after with the longitudinal field component \vec{B}_z . The coupling of the particle velocities with the magnetic field is described by the Lorentz Force: $\vec{F}_L = q\vec{v} \times \vec{B}$. At the end of the solenoid particles rotate and are focused.

The longitudinal magnetic field generated by a solenoid with N coils powered with a current I , a total length L and a coil thickness $a_2 - a_1$ can be estimated by (see Ref.[56])

$$B_z = \frac{\mu_0 I N}{2L(a_2 - a_1)} \left[(z + L/2) \ln \left(\frac{a_2 + \sqrt{a_2^2 + (z + L/2)^2}}{a_1 + \sqrt{a_1^2 + (z + L/2)^2}} \right) + \right. \\ \left. - (z - L/2) \ln \left(\frac{a_2 + \sqrt{a_2^2 + (z - L/2)^2}}{a_1 + \sqrt{a_1^2 + (z - L/2)^2}} \right) \right]. \quad (4.1)$$

In general solenoid magnets (and rotated quadrupoles) introduce a coupling in the beam transverse planes. Considering only linear terms, the equations of motion for a charged particle in a field produced by a solenoid are (see Ref. [57])

$$\begin{aligned} x'' &= \frac{e}{p} B_z y' + \frac{1}{2} \frac{e}{p} B'_z y \\ y'' &= -\frac{e}{p} B_z x' - \frac{1}{2} \frac{e}{p} B'_z x \end{aligned} \quad (4.2)$$

these equations exhibit clearly coupling terms. Chromatic effects originate from the momentum factor e/p which is different for particles with different energies.

Considering a uniform magnetic field, $B'_z = 0$, the trajectory of the particles have the form of an helix parallel to the axis of the solenoid. It is convenient to replace all derivatives with respect to z by derivatives with respect to time, using the particle velocity v , and replace $\frac{d}{dz}$ with $\frac{1}{v} \frac{d}{dt}$. In a uniform solenoid field the equation of motion are

$$\begin{aligned} \ddot{x} &= \frac{e}{p} B_z v \dot{y} = \omega_L \dot{y} \\ \ddot{y} &= -\frac{e}{p} B_z v \dot{x} = -\omega_L \dot{x} \end{aligned} \quad (4.3)$$

where the Larmor frequency ω_L is defined, considering a beam energy E , as

$$\omega_L = \frac{e B_z}{p} v = \frac{e c^2}{E} B_z. \quad (4.4)$$

The solutions of the equations of motions are

$$\begin{aligned} x(t) &= x_0 - \frac{v_t}{\omega_L} \cos \omega_L t \\ y(t) &= y_0 - \frac{v_t}{\omega_L} \sin \omega_L t \end{aligned} \quad (4.5)$$

from which the particle perform an helix during the propagation. The amplitude of the oscillating term in the equation 4.5 is the radius of the helical path that is

$$\rho_h = \frac{p_t}{eB_z} \quad (4.6)$$

where $p_t = \gamma m v_t$ is the transverse momentum of the particle. The longitudinal motion is unaffected by the magnetic field, so that $\dot{v}_z = 0$. The time in which a particle perform one helical period is $T = 2\pi/\omega_L$.

The equations of motion 4.2 are derived considering paraxial rays i.e. $v \approx v_z$. Of course this is a strong assumption, that in general is not useful because the solenoid usually need to focus particles that have a divergence. Considering the equations of motion 4.2 without paraxial approximation, the solution are more complex.

Because the particles rotate in the solenoid we can consider, a rotation of the coordinated system may help to simplify the solution of the differential equations. By the introduction of coordinates rotation of an angle ϕ , that depends by the longitudinal coordinate z , in complex notation it can be represented by

$$R = (x + iy)e^{-i\phi(z)}. \quad (4.7)$$

Unifying equations 4.2 to form a single differential equation and applying the rotation 4.7 it is possible to obtain a simple equation of motion for the rotating particle system

$$R'' + \frac{1}{4} \left(\frac{e}{p} B_z \right)^2 R = 0. \quad (4.8)$$

Expressing $R = v + iw$, where v, w represent the particle coordinates x, y it is possible to obtain two uncoupled equations

$$\begin{aligned} v'' + \frac{1}{4} \left(\frac{e}{p} B_z \right)^2 v &= 0 \\ w'' + \frac{1}{4} \left(\frac{e}{p} B_z \right)^2 w &= 0. \end{aligned} \quad (4.9)$$

By the introduction of the rotation of the coordinates through the term R , we have reduced the coupled differential equation of motion 4.2, to the form of uncoupled equations of motion that exhibit focusing in both planes. At the solenoid entrance

$\phi = 0$ so that $v_0 = x_0$ and $w_0 = y_0$. Considering a solenoid length L the particle motion, described by the coordinate v, w , can be interpreted as the superposition of a focusing term described by a quadrupole with a strength $k_s = \frac{1}{4} \left(\frac{e}{p} B_z(L) \right)^2$ and a rotation of the coordinate system by an angle $\phi(L)$ thus reverting to cartesian coordinates (x, y) .

Usually solenoid magnets are aligned on the beam axis, so that the beam do not experience the effects of particular perturbation terms as multipole field effects.

Considering a real beam that has an energy spread, a divergence of the particles and that moves off the solenoid axis, perturbative effects like multipole field effects become relevant. The equations of motion in that case shows an enormous complexity, as shown in Ref. [57]. In fact using a curvilinear Frenet-Serret coordinate system, it is possible to obtain two equation of motions for charged particles that have an energy spread and that move off-axis in a magnetic field. Unfortunately these equations considering an expansion up to third order, show an enormous complexity (see Ref. [57]). From these considerations it appears very difficult to estimate solenoid misalignments using analytical formulas and so a qualitative approach, using experimental data, has to be found.

4.2 The SPARC_LAB gun solenoid

The SPARC_LAB gun solenoid was designed and originally tested in the Particle Beam Physics Laboratory at UCLA university and it is made up of 4 coils independently powered. The first and the last 2 coils are powered with a currents that flow in opposite directions. In this way the particles in the middle of the solenoid begin to reduce their rotation and do not rotate at the exit of the magnet. In Figure 4.1 on the left the SPARC_LAB gun solenoid, on the right it is schematically represented what happens to a particle that entering in this solenoid is focused but at the exit does not have a rotation. By this due to the focusing without a final rotation, the particle at the solenoid end can be represented on line that passes on the entry position of the particle and on the solenoid center.

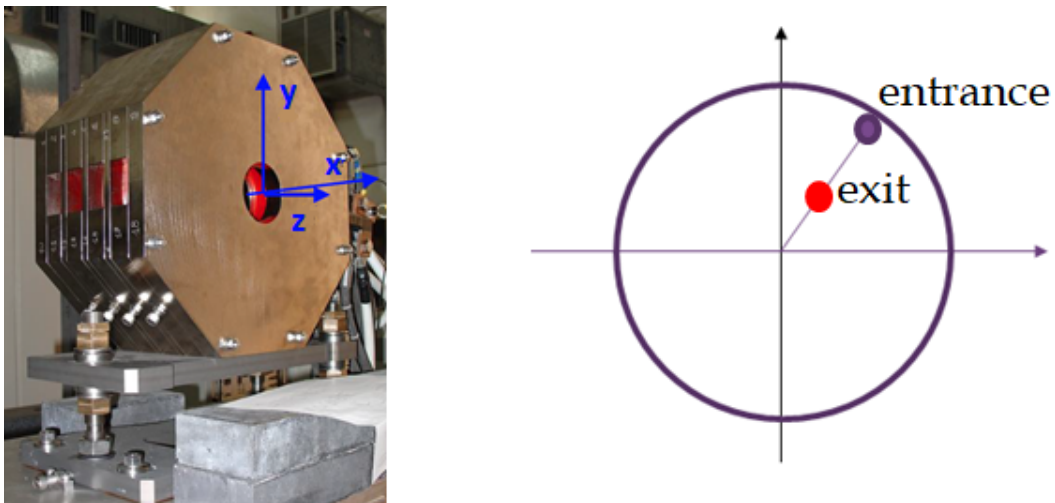


Figure 4.1. On the left The SPARC_LAB gun solenoid, made by 4 coils. The first and the last two coils are powered with currents that flow in opposite directions. The result of this configuration is a bunch that is focused but particles do not rotate at the solenoid exit. On the right a schematic representation of a particle that entering in this solenoid (the circle in the picture) is focused, but at the end does not rotate. We can schematically represent this phenomena displacing the focused red particle at the solenoid exit, on a line that passes between the particle entry position and the center of the solenoid.

By experimental data at SPARC_LAB, effects of gun solenoid misalignments are evident. In fact measuring the beam spot sizes and the beam centroid positions on a YAG flag before the first accelerating section, we measure a beam centroid displacement varying the currents (and so the magnetic field) in the coils. Furthermore the beam presents different spot sizes in the x and y planes.

As seen at the end of the previous section, analytical formulas that describes the particle motion for a beam that enters off-axis are too much complicated to be useful. The kicks that a bunch experiences in an off-axis solenoid can be qualitatively

interpreted considering the bunch made by longitudinal slices as in Figure 4.2. Considering for example a vertical solenoid misalignment, excluding the rotation effects, every vertical bunch slices entering the solenoid perceive a different transverse field B_{\perp} and subsequently a different coupling with the longitudinal field B_z inside the solenoid. As shown qualitatively in Figure 4.2 in a bunch that enters off axis in the y plane, the top slice (the red one in the figure) perceive an higher transverse fringe field compared to the bottom one and so a different coupling with the particle velocities ($v \times B_{\perp}$). Subsequently every slices acquire a different transverse acceleration and velocity v_{\perp} in the x plane, that leads to a different coupling with the longitudinal field ($v_{\perp} \times B_z$). The net effect is an higher focusing for the external slice, or if the focusing is highly different they can reverse as in figure. The effects that we can measure after that off-axis solenoid are the beam focusing, a displacement of the bunch centroid and different beam spot sizes if the misalignment is higher in one transverse plane with respect to the other one. Of course as we have seen at SPARC_LAB these effects are amplified increasing the current in the coils and so the magnetic field components B_{\perp} and B_z .

Some studies as in Ref. [58] report methods to align solenoids, considering a current that flows in the coils in the same direction.

I present a new beam-based alignment method using GPT to estimate the misalignments of the gun solenoid at SPARC_LAB where the coils are powered with an opposite current.

First of all we have to consider that beam kicks can be generated both by solenoid misalignments in the transverse planes and by a solenoid tilt. Considering that by experimental data we are not able to separate misalignments with respect to a solenoid tilt, an evaluation of kick effects due to misaligned and to tilted solenoid was done using GPT.

Taking into account the 100pC bunch that we had during the dedicated run, the GPT simulation was optimized to re-create the same bunch up to the region ($z \approx 15m$) where we can measure the bunch length using an RF deflector and we have measured a beam emittance of $\epsilon_{n,rms} = 0.9\mu m$, a bunch length of $\sigma_z = 320\mu m$ and a spot size of $\sigma_x = 500\mu m$. The real laser spot on the cathode used during the run was imported as a digital picture in GPT, considering an intrinsic emittance of $0.7\mu m$. The best resolution to align the solenoid is about $100\mu m$ and for misalignments below that threshold we can not improve the alignment. To estimate how much is the beam kick from a transverse gun misalignment with respect to the tilt one, I evaluated with GPT both cases to make a comparison. Firstly I misaligned in GPT the gun solenoid of $100\mu m$ in the transverse y direction, as shown in the left of Figure 4.3. After that the tilted solenoid configuration was tested, considering

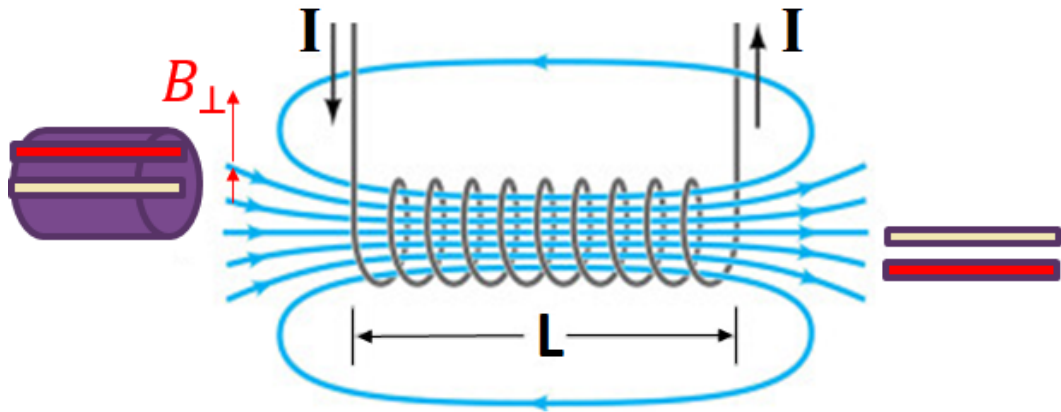


Figure 4.2. It is possible to consider a beam that enters off-axis the solenoid, as formed by longitudinal slices that perceive a different B_{\perp} and so a different coupling ($v \times B_{\perp}$), depending on their transverse position. Subsequently every slices acquire a different transverse acceleration and velocity v_{\perp} that leads to a different coupling with the longitudinal field ($v_{\perp} \times B$). For example due to the fringe magnetic field the top red slice in figure perceives an higher transverse field, and so acquiring an higher transverse velocity, it will interact more with the longitudinal magnetic field inside the solenoid. The net effect is an higher focusing compared to the bottom yellow slice, or if the focusing is highly different they can reverse as in figure. The effects that we can measure after that off-axis solenoid are the beam focusing, a displacement of the bunch centroid and different beam spot sizes if the misalignments is higher in one transverse plane with respect to the other one. Of course as we observed at SPARC_LAB these effects are more evident increasing the current in the coils and so the magnetic field components B_{\perp} and B_z .

the worst case of a tilt of $\pm 100\mu\text{m}$ of both solenoid ends, as shown in the right of Figure 4.3.

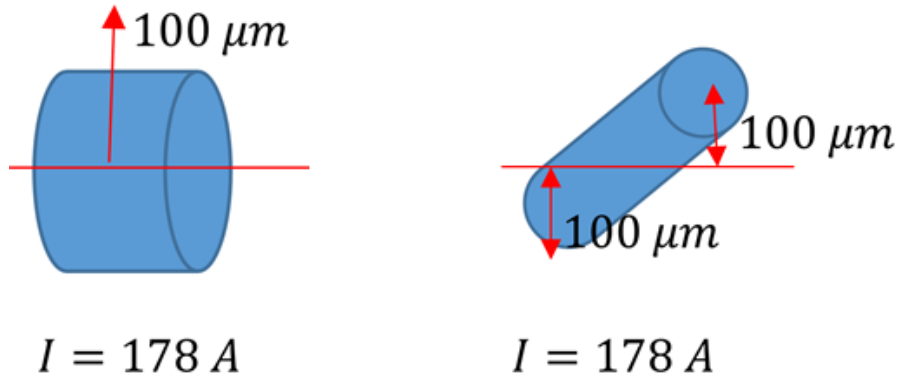


Figure 4.3. In order to estimate the effects of a misaligned solenoid and of a tilted one, GPT simulation were done using the beam that we had during the run and moving and tilting the solenoid in the vertical according considering that the best alignment value that we can obtain is $100\mu\text{m}$ and we can not correct misalignments below this value.

Considering the bunch centroid coordinate $(x_c; y_c)$, simulation results show that the bunch centroid receives a kick and show a centroid displacement in the opposite direction with respect to the misalignment. In fact in the simulation measuring the beam in correspondence of the first SPARC_LAB flag at the position $z = 1.181\text{m}$, while $x_c \approx \text{cost}$, the bunch centroid displacement in the y axis is $y_c \approx 600\mu\text{m}$.

The simulation results of the tilted solenoid show a six time lower bunch centroid displacement. In fact as it shown in Figure 4.5, the bunch centroid receives a kick that produces a bunch centroid displacement of $y_c \approx 100\mu\text{m}$ while $x_c \approx \text{cost}$.

Considering that the main effect on the beam is generated by a transverse misalignments, and also that it is possible to remove the tilt without a beam based alignment, the alignment method was done to estimate the solenoid displacement in the vertical and horizontal directions.

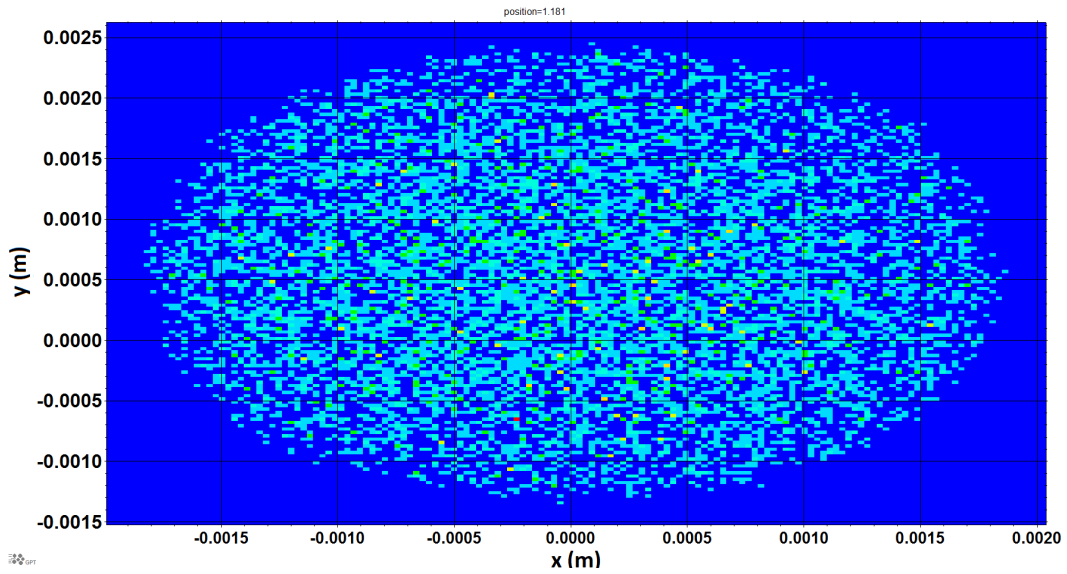


Figure 4.4. Particle density of the transverse beam spot at the position $z = 1.181\text{m}$, by GPT simulation moving the solenoid in the y direction. A $100\mu\text{m}$ misalignment in the y axis, generates a bunch centroid displacement in the opposite direction of about $y_c \approx 600\mu\text{m}$, while $x_c \approx \text{cost}$.

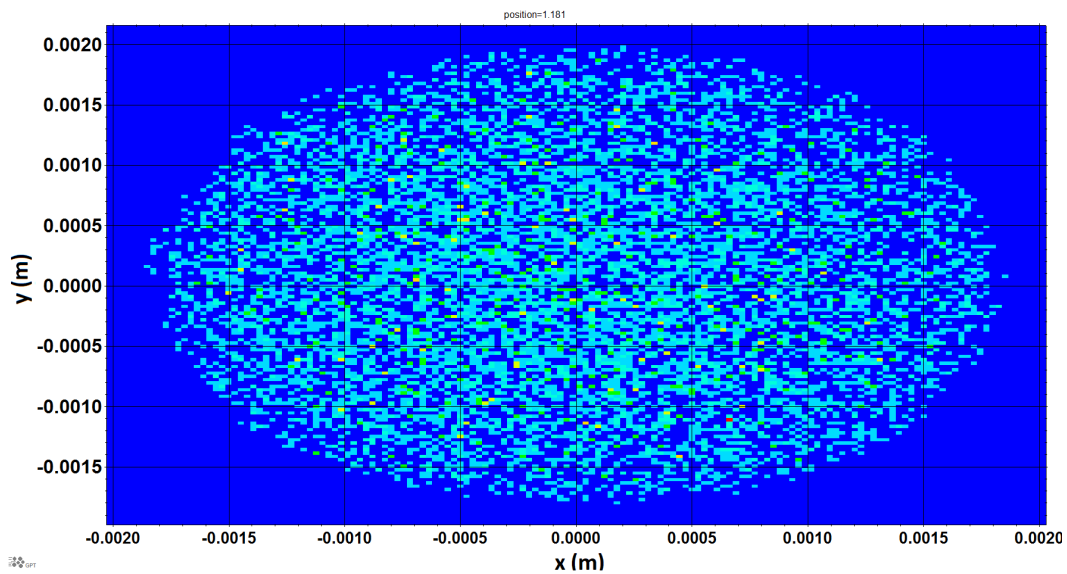


Figure 4.5. Particle density of the transverse beam spot at the position $z = 1.181\text{m}$, by GPT simulation tilting the solenoids ends of $\pm 100\mu\text{m}$ in the y axis. This kind of misalignment generates a displacement of the beam centroids of about $y_c \approx 100\mu\text{m}$, while $x_c \approx \text{cost}$.

4.3 Beam based alignment at SPARC_LAB

To estimate the gun solenoid misalignments it is necessary to place a reference frame on the beam line, and on this frame the misalignments are estimated. To do that a dedicated run at SPARC_LAB was done, performing scans of the gun solenoid current. The effects of the current scans on the beam spot sizes were measured on a YAG flag at the position $z = 1.181$ m.

Powering only one or two solenoid coils at the same time, it was not possible to focus the beam enough to see it on the flag, so that we need to consider to power all coils at the same time i.e. considering the solenoid as a single component.

Magnetic field measurements on the gun solenoid were done in Ref.[59], varying the current in the coils between 0 – 300 A and measuring the longitudinal magnetic field B_z as reported in Figure 4.6. As expected by the theory in the previous sections and by equation 4.1, the magnetic field on the longitudinal axis linearly increases with the current in the coils.

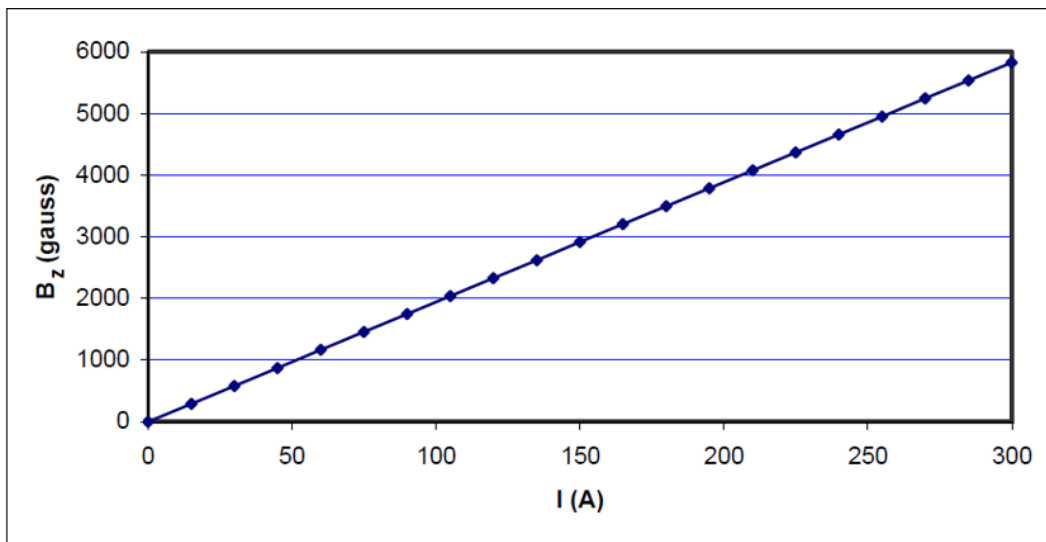


Figure 4.6. Magnetic field measurements on the SPARC_LAB gun solenoid were done varying the current in the coils between 0 – 300A with current steps of 15 A and measuring the magnetic field on the longitudinal axis B_z with a resolution of 0.05 Gauss. From Ref. [59].

A linear fit of the data in Figure 4.6 provides a scaling law of the longitudinal magnetic field with the current that is

$$B_z(\text{Gauss}) = 19.43(\text{Gauss } A^{-1})I(A). \quad (4.10)$$

During the dedicated run at SPARC_LAB the current in the coils has been varied

in a range between 180 – 220 A, with a step current of 2 A. In this range as it shown in Figure 4.6, we have a linear increase of the magnetic field with the current. On the YAG flag the beam spot sizes have been measured and by off-line analysis have been estimated the bunch dimensions and the bunch centroid positions. In Figure 4.7 are reported on the left the bunch dimensions and on the right the bunch centroid positions considering the transverse horizontal plane x . For the transverse vertical plane y the same data are reported in Figure 4.8.

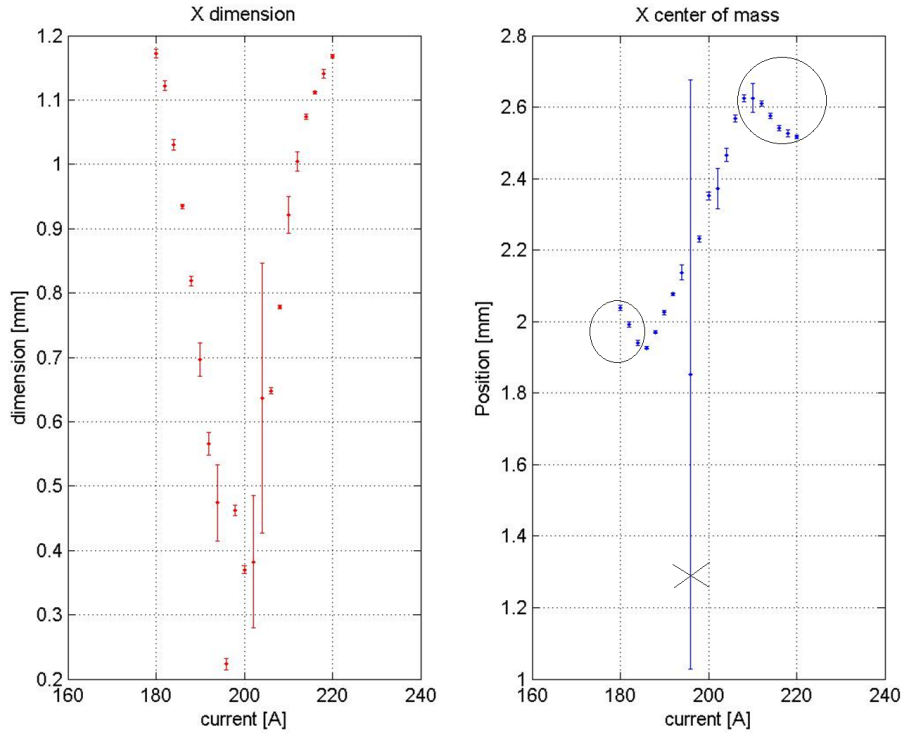


Figure 4.7. Off-line data analysis of the gun solenoid scan at SPARC_LAB, varying the current in the coils in the range 180 – 220 A. The beam spots was measured in the first YAG flag in the longitudinal position $z = 1.181$ m. On the left the bunch dimensions on the x axis measured in the flag, on the right the correspondent bunch centroid positions on the x axis. In the current ranges 180 – 186 A and 208 – 220 A the beam waist is respectively after and before the flag, so that the external bunch particles have been cut off the flag. During the scan a discharge in the gun occurred while the current was set to $I = 196$ A. These data are marked on the right figure, and were not taken into account in the analysis. Fitting linearly the bunch centroid position data it is possible to obtain the unperturbed centroid coordinate x_0 for $I = 0$. The line of the linear fit has an angular coefficient of $m_x = 0.031241$, and by the fit $x_0 = -3.91047$ mm.

For low current values, between 180 – 186 A, the beam is not well focused on the target flag so that external bunch particles have been cut off by the flag. For high current values, between 208 – 220 A, the beam was focused before the flag, so that after the waist due to their divergences the external bunch particles have been

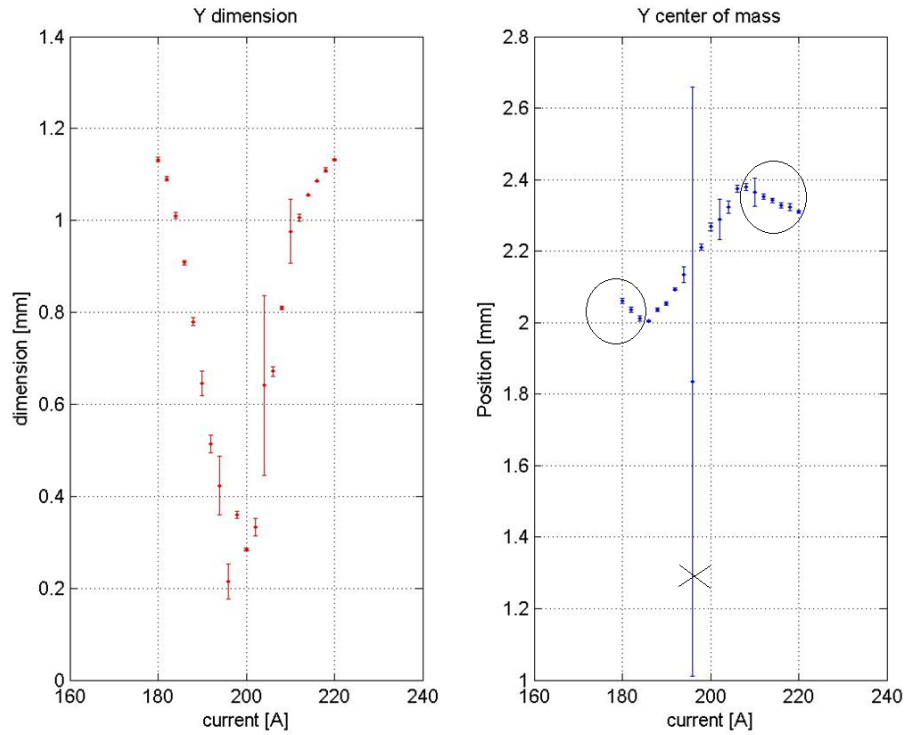


Figure 4.8. Off-line data analysis of the gun solenoid scan at SPARC_LAB, varying the current in the coils in the range 180 – 220 A. The beam spot was measured in the first YAG flag in the longitudinal position $z = 1.181$ m. On the left the bunch dimensions on the y axis measured in the flag, on the right the correspondent bunch centroid positions on the y axis. In the current ranges 180 – 186 A and 208 – 220 A the beam waist is respectively after and before the flag, so that the external bunch particles have been cut off the flag. During the scan a discharge in the gun occurred while the current was set to $I = 196$ A. These data are marked on the right figure, and were not taken into account in the analysis. Fitting linearly the bunch centroid position data it is possible to obtain the unperturbed centroid coordinate y_0 for $I = 0$. The line of the linear fit has an angular coefficient of $m_y = 0.018782$, and the by the fit $y_0 = -1.50250 = \text{mm}$.

cut off the flag. These solenoid current values were not taken into account in my analysis.

Fitting linearly the bunch centroid position data, we can obtain for $I = 0$, the centroid coordinates without solenoid perturbations i.e. the bunch reference line (x_0, y_0) , that are $x_0 = -3.91047\text{mm}$ and $y_0 = -1.50250\text{mm}$. The angular coefficients of the linear fits are $m_x = 0.031241$ and $m_y = 0.018782$ mm.

The bunch centroid considering the solenoid current $I = 0$, represents the bunch reference line where we can position the unperturbed reference frame in respect to which we estimate the solenoid misalignments.

Since the magnetic field increase linearly with the current, according to the experimental data, due to the misalignments the bunch centroid coordinates x_c, y_c increase linearly too. This is schematically represented in Figure 4.9 where, starting from the coordinates (x_0, y_0) , the bunch centroid moves on line increasing the current.

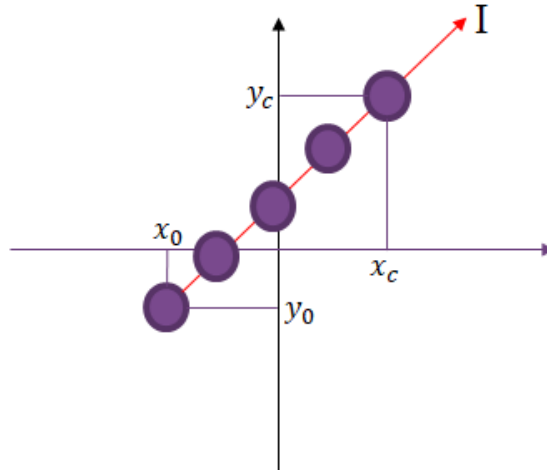


Figure 4.9. Schematic representation of the linear displacement of the bunch centroid increasing the current in the coils I . The centroid coordinates (x_c, y_c) linearly increase with the current. Starting from the unperturbed orbit, that corresponds to the position (x_0, y_0) , the beam centroid moves on a line.

Since the unperturbed centroid coordinates (x_0, y_0) where we set the reference frame, does not correspond to the $(x = 0, y = 0)$ of the YAG flag, to calculate the centroid displacement in the unperturbed reference frame, it is necessary to take into account the absolute values $(|x_0| + |x_c|, |y_0| + |y_c|)$.

In Figure 4.10 are reported the experimental results (x_c, y_c) as measured at SPARC_LAB in the YAG flag reference frame, varying the solenoid current ISOL. (x_0, y_0) represents the coordinate of the unperturbed frame with respect to the flag frame, while $(|x_0| + |x_c|, |y_0| + |y_c|)$ are the beam displacements coordinates in the

unperturbed reference frame.

<i>ISOL</i> (A)	x_c (mm)	y_c (mm)	x_0 (mm)	y_0 (mm)	$ x_0 + x_c $ (mm)	$ y_0 + y_c $ (mm)
			-3,91047	-1,5025		
186	1,926638	2,004609			5,837105	3,507112
188	1,970898	2,03623			5,881365	3,538733
190	2,025531	2,053069			5,935998	3,555572
192	2,077063	2,093031			5,987530	3,595534
194	2,137242	2,134213			6,047709	3,636716
198	2,231432	2,211147			6,141899	3,71365
200	2,351545	2,267995			6,262012	3,770498
202	2,37206	2,289049			6,282527	3,791552
204	2,466206	2,322754			6,376673	3,825257
206	2,568433	2,37482			6,478900	3,877323

Figure 4.10. Experimental results (x_c, y_c) as measured at SPARC_LAB in YAG reference frame varying the solenoid current *ISOL*. (x_0, y_0) represents the coordinate of the unperturbed frame with respect to the flag frame, while $(|x_0| + |x_c|, |y_0| + |y_c|)$ are the beam displacements in the unperturbed reference frame.

In order to find the solenoid misalignments in x and y axis, GPT simulations have been performed, starting from the cathode $z = 0$ m up to the YAG flag $z = 1.181$ m. Using the centroid displacements in the unperturbed reference frame $(|x_0| + |x_c|, |y_0| + |y_c|)$ obtained varying the current, the misalignments had been found by the GPT solver, moving the solenoid in the transverse plane and trying to reproduce the centroid displacements.

As we said the bunch in GPT was optimized up to re-create the experimental measurements, the imported spot on cathode is in Figure 4.11 the spot sizes are $\sigma_{x,rms} = 493\mu m$ and $\sigma_{y,rms} = 481\mu m$, the bunch duration is set to $\sigma_{z,rms} = 660$ fs and the thermal emittance is set to $0.7\mu m$.

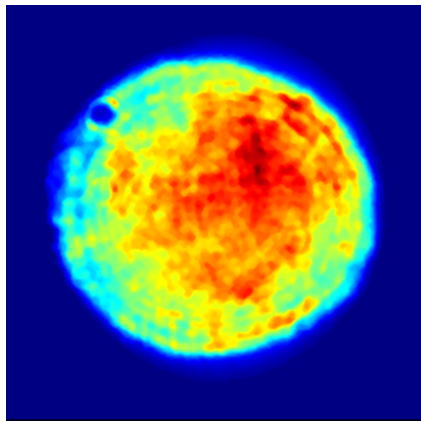


Figure 4.11. Laser spot on the cathode used during the run and imported in the GPT simulations.

At SPARC_LAB the beam energy was measured at the gun exit varying the current and so the magnetic field in an orbit corrector, by the beam displacement measurements the bunch energy was measured. The results are shown in Figure 4.12, resulting in a beam energy of about 4.7 MeV.

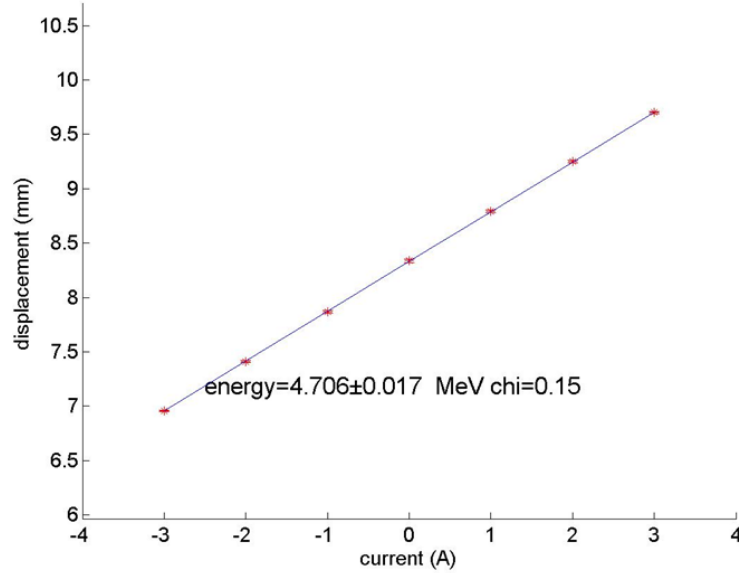


Figure 4.12. Energy measurements at SPARC_LAB, using the variation of the magnetic field of an orbit corrector after the gun and measuring the relative beam displacement. The energy at the gun exit was about 4.7 MeV.

In GPT the power in the RF gun cells was tuned in order to have the same beam energy obtained during the run. Figure 4.13 shows the beam longitudinal phase space in GPT, approximately in the same position of the experimental measurement and also in GPT the beam energy is about 4.7 MeV.

In simulations the solenoid was initially set in the position x_0, y_0 and was moved in x and y axis by the GPT solver, performing different simulations for different solenoid transverse positions, in order to reproduce the bunch centroid displacement ($|x_0| + |x_c|, |y_0| + |y_c|$) experimentally measured with a current of $I = 186$ A.

By this scan the solenoid misalignments were found in the x plane equal to 0.927mm and in the y plane equal to 0.515mm.

Placing the solenoid in the found misaligned position, the current in the coils was varied in order to reproduce the experimental values obtained in the current range of 186 – 206 A. In Figure 4.15 are reported the bunch centroid positions from the simulations compared with the ones from the experimental data. The found misalignments well reproduce the experimental data. From the difference between the experimental and simulated centroid positions, we have that aligning the solenoid

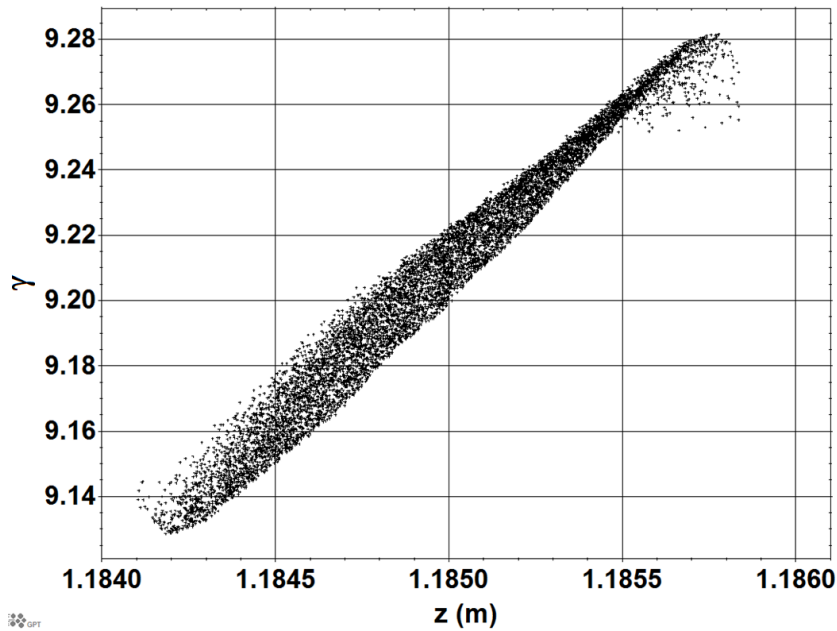


Figure 4.13. Beam phase space from the GPT simulation optimized to have the same experimental beam energy in the flag at $z = 1.181$ m.

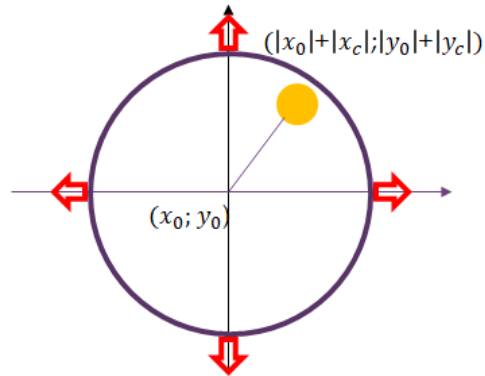


Figure 4.14. Schematic representation of the scan simulations performed by the GPT solver. Initially the solenoid (the circle in the figure) was set in the position x_0, y_0 , in order to reproduce the beam position $(|x_0| + |x_c|, |y_0| + |y_c|)$ (yellow ball) measured at SPARC_LAB using a current of $I = 186$ A, the solenoid was moved in the x and y axis.

to the found values it is possible to improve the centroid orbit displacement up to 99.4%.

<i>ISOL</i> (A)	$ x_0 + x_c $ (mm)	$ y_0 + y_c $ (mm)	<i>Misx</i> (mm)	<i>Misy</i> (mm)	<i>Avgx</i> (GPT)(mm)	<i>Avgy</i> (GPT)(mm)	Δ_x (mm)	Δ_y (mm)
186	5,837105	3,507112	0,927	0,515	5,80251	3,49263	0,034595	0,014482
188	5,881365	3,538733			5,88227	3,52415	-0,0009	0,014583
190	5,935998	3,555572			5,95578	3,59244	-0,01978	-0,03687
192	5,987530	3,595534			6,06527	3,65916	-0,07774	-0,06363
194	6,047709	3,636716			6,14559	3,72954	-0,09788	-0,09282
198	6,141899	3,71365			6,31664	3,81466	-0,17474	-0,10101
200	6,262012	3,770498			6,3927	3,90247	-0,13069	-0,13197
202	6,282527	3,791552			6,44695	3,95908	-0,16442	-0,16753
204	6,376673	3,825257			6,50522	3,98656	-0,12855	-0,1613
206	6,478900	3,877323			6,62641	4,10475	-0,14751	-0,22743

Figure 4.15. Placing the solenoid in the misaligned position (*Misx* and *Misy* in the table) found by GPT considering the experimental bunch displacement measured with a solenoid current of 186 A. $|x_0| + |x_c|$ and $|y_0| + |y_c|$ are the measured displacement in the x and y axis of the unperturbed frame. *Avgx* and *Avgy* are the bunch displacements measured with the misaligned solenoid in GPT. Δ_x and Δ_y are the differences between the experimental and simulated centroid positions.

Also a solenoid misalignment optimization at a current of 206 A has been found with GPT using the same method and results are very similar. In fact the found misalignment on the x axis is 0,902 mm and the one on the y axis is 0,517 mm, but the differences between the experimental centroid displacements and the simulated ones, Δ_x and Δ_y , are higher compared to the ones in Figure 4.15.

Also the emittance degradation due to the misaligned solenoid was checked. In the position $z = 1.181$ m without misalignments we have by GPT a normalized rms emittance of $\epsilon_{n,rms} = 1.06 \times 10^{-6}$. In the same position considering the found misalignments we obtain an emittance of $\epsilon_{n,rms} = 1.1 \times 10^{-6}$, resulting in an emittance degradation of about 3%.

Finally the reliability of the analysis was checked, to confirm that the solenoid field map used in simulations agrees with experimental measurements. In the GPT simulations the gun solenoid field map was obtained running SUPERFISH, then the map was misaligned with the found values. To test as expected the linear bunch centroid displacements with the current increase, a solenoid scan with GPT was done measuring the bunch centroid positions in the same place of the SPARC_LAB flag. The solenoid current scan was performed in the region in which we expect a linear growth of the field, varying the current from 0 A to 300 A. In Figure 4.16 are reported the GPT results. In the horizontal axis currents in the coils are reported, in the vertical axis the beam horizontal centroid positions are reported considering

the found solenoid misalignments. In the region where the current was varied during the experimental scan, the GPT data are in good agreement with a linear trend, confirming the reliability of the analysis.

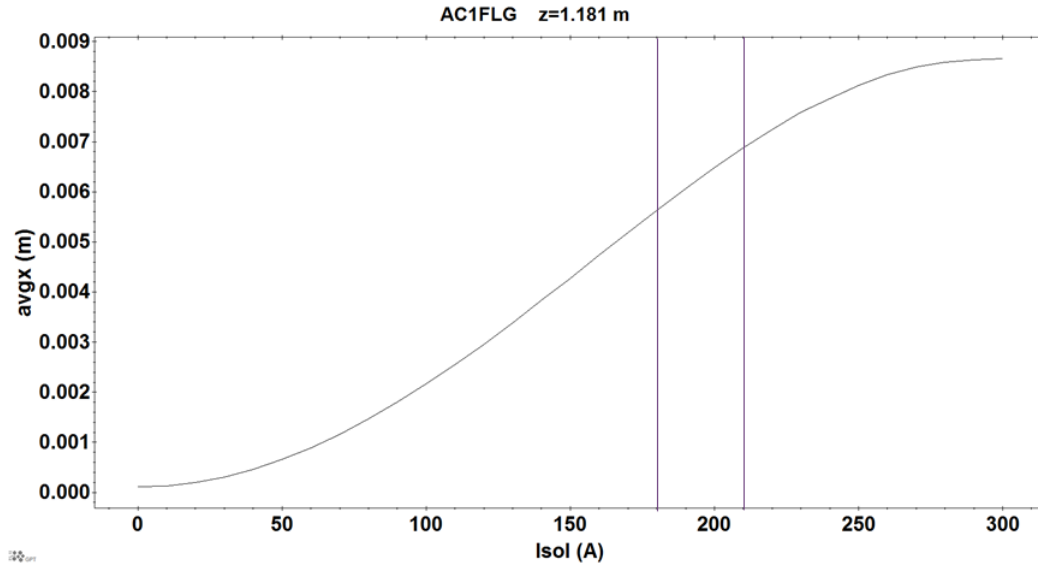


Figure 4.16. To check also in GPT the linear trend of the bunch centroid displacements increasing the current, a simulation scan was performed, varying the solenoid current in the range 0 – 300 A with a step of 1 A. In the y axis are reported the average x positions of the bunch particles that represent the bunch centroid.

4.4 Printed circuit skew quadrupoles at SPARC_LAB

In order to perform experiments where a transverse circular shape is necessary, as for example plasma acceleration that we are going to start at SPARC_LAB and where the stringent transverse matching conditions require a circular beam profile of only some microns, we need to have a transverse beam spot as near as possible to a circular shape. A not perfectly aligned device along the beam line (magnetic devices, accelerating structures...), or a misaligned laser on the cathode can generate an ellipsoidal bunch shape. By machine operations this effect is evident at SPARC_LAB, also due to the misaligned gun solenoid. In order to correct or pre-correct the beam profile, having a circular profile at the plasma entrance, I studied the possibility to insert Printed Circuit (PC) skew quadrupoles on the SPARC_LAB beam line.

As seen in the first section of this chapter, rotated quadrupoles are able to couple the transverse plane. In fact (see Ref. [57]) the equation of motion for skew quadrupoles are:

$$\begin{aligned}x'' + ky &= 0 \\y'' + kx &= 0\end{aligned}\tag{4.11}$$

where k is the quadrupole strength. These equations are very similar to the equations for ordinary quadrupoles, but in this case the restoring force in one plane depends on the particle amplitude in the other plane. As it happens for the upright quadrupole, the skew one is focusing in one plane and defocusing in the other, but the effect of the rotated quadrupoles is to mix both planes. The final effect using more than one of that devices, is that it is possible to correct an ellipsoidal bunch shape, that is out by the main axis x and y .

Since at the moment there is no free space in the SPARC_LAB linac, I proposed to insert these devices inside the new gun solenoid which is currently being planned. Because the transverse free space is not so much to install standard magnetic quadrupoles, I evaluated the hypothesis to use PC quadrupoles. By the gun solenoid design, the longitudinal and horizontal free space inside the new solenoid is on the first solenoid coil. In fact inserting these devices in the second coil, the beam is too much focused by the solenoid so that we need to increase too much the gradients and however in this position the effects of the PC quads are very low. According to the free space the proper length can be about 3 cm.

Firstly we realized the design of these devices using ANSYS Maxwell. Each PC quadrupole is made by four PC copper coils, each one has a transverse section of $1mm^2$ as shown in Figure 4.17.

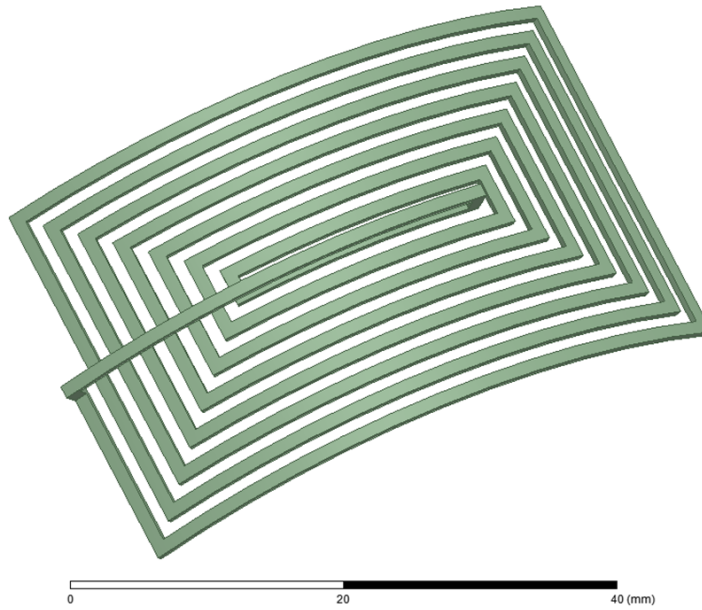


Figure 4.17. One of the four PC copper coil, with a transverse section of 1mm^2 .

By the magnetic simulation results of these PC quadrupoles, they can reach a gradient of 2.1×10^{-2} T/m, using a current of 10 A. The design of the quadrupole and the simulated magnetic field are shown in Figure 4.18.

Using that devices, considering a rotation of 45° , I searched with GPT the proper positions and proper gradients to obtain a transverse circular beam shape. I simulated the SPARC_LAB beam line up to the first YAG flag, in the longitudinal position of $z = 1.181$ m, considering a 100 pC beam with an ellipsoidal shape on the cathode. The difference in the spot sizes was about 14% between x and y planes. In fact the laser parameters on the cathode are set to $\sigma_x = 550\mu\text{m}$ and $\sigma_y = 632\mu\text{m}$ and a laser duration of 660 fs.

The optimization with GPT were done considering 10k macro particles. After the the longitudinal positions optimization, we have that using a gradient of the first quadrupole of 5×10^{-2} T/m and a gradient of the second one of 3.7×10^{-2} T/m, we can reduce the ellipsoidal bunch shape on the first flag from the starting 14% to 1%. In figure Figure 4.19 are shown the simulation results for the beam spot sizes. The emittance evolutions in both transverse planes are in Figure 4.20. Considering that also the emittances in the x and y plane has an initial difference of about 14%, using these devices it is possible to reduce the difference on the first flag up to 5%. By the simulation results obtained with GPT, currently we are modifying the new SPARC_LAB gun solenoid design with the insertion of these devices. To produce the PC quadrupoles we are evaluating the possibility to print firstly the copper circuit and after immerse it in a silicone bath. Furthermore by magnetic simulation results

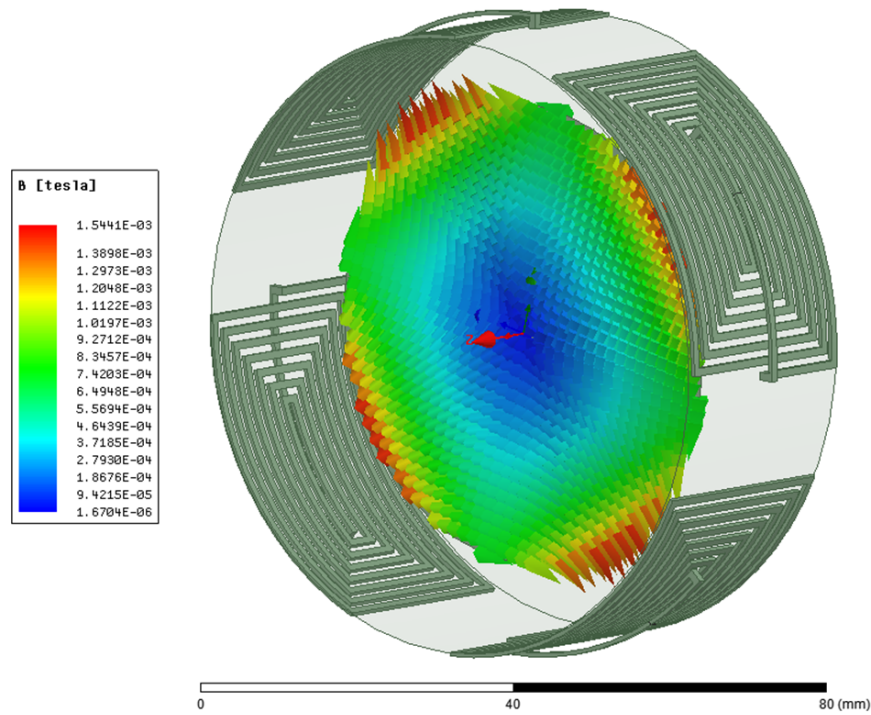


Figure 4.18. Design of the PC skew quadrupole and the simulated magnetic field obtained by ANSYS Maxwell.

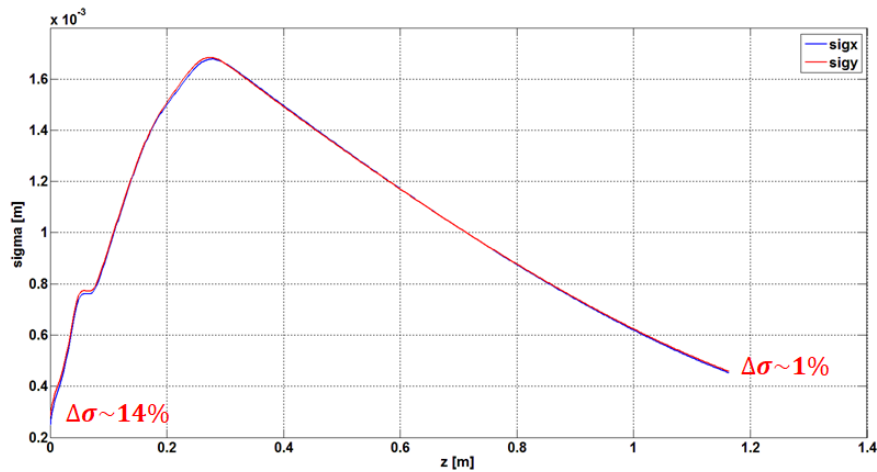


Figure 4.19. Evolution of the σ_x and σ_y up to the first flag at $z = 1.181$. Using the skew quadrupoles in optimized positions on the first coil of the gun solenoid, starting with a beam spot difference in the x and y plane of about 14%, it is possible to reduce this difference up to about 1%.

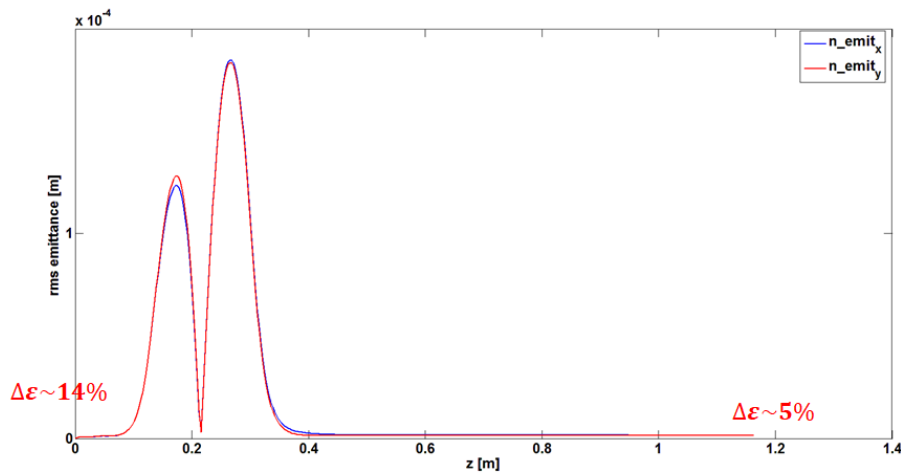


Figure 4.20. Evolution of the normalized rms emittances $\epsilon_{x,n,rms}$ and $\epsilon_{y,n,rms}$ up to the first flag at $z = 1.181$. Using the PC skew quadrupoles in optimized positions on the first gun solenoid coil, starting with an emittance difference in the x and y planes of about 14%, it is possible to reduce this difference up to about 5%.

obtained with ANSYS Maxwell these quadrupoles can reach very high temperatures, about $T \approx 250\text{ C}^\circ$, using a current in the coils of 10 A. To fix this drawback, currently we are also planning a proper system to cool these devices. We are evaluating the possibility to position these devices directly on the solenoid coil, that has a proper water cooling.

Conclusions

After an introduction over the photoinjector, starting from the electrons emission from the cathode surface, the main photoinjector physical aspects were treated. By means of an higher RF peak field on the cathode surface it has been shown that it is possible to strongly reduce the final beam normalized rms emittance, taking under control the space charge forces responsible for the emittance growth. It has been taken into account a recent proposal for a reduced half cell S-band gun in which, operating at cryogenic temperature, it is possible to increase the peak field on the cathode surface up to 240 MV/m. The beam dynamics in this gun was optimized with GPT for a very low charge beam ($Q = 0.1$ pC) using the so called beam cigar regime. The final bunch parameters are: length of $\sigma_z = 3$ μm and final emittance of $\epsilon_{n,rms} = 10$ nm that can be useful for QFEL experiment. To envision a realistic QFEL experiment the energy spread has to be improved from, the current value, of 10^{-2} to, the value required by the theory, of 10^{-5} . This result can be obtained for example by changing the compression technique.

The beam dynamics for a completely new high gradient (240 MV/m) C-band gun was optimized with GPT. The optimized cathode laser parameters, gun solenoid magnetic field and position of the first accelerating section were found. Using a cigar beam shape the final energy of about 150 MeV was reached exploiting two TW C-band. The final beam emittance was about 55 nm. The final beam peak current $I \approx 64.1$ A leads to a final FWHM beam brightness of about $B_{FWHM} \approx 4.2 \times 10^{16}$ A/m².

Using a blow out shaped beam, I took advantage of this gun to design with GPT the layout of the future SPARC_LAB upgrade, where using 24 X-band modules after the S-band photoinjector the final beam energy is about 1.1 GeV, with a final emittance of about $\epsilon_{n,rms} = 280$ nm and an energy spread of about 0.1% resulting to a beam brightness of about $B \approx 9 \times 10^{16}$ A/m².

Leveraging on the same linac machine layout we are investigating a cigar shaped bunch whose advantage is the achievement of a much higher brightness compared to the blow out shaped bunch. This new investigation relies on a full C-band photoinjector (gun and accelerating sections) followed by an X-band linac, the same already used for previous investigations discussed in this thesis.

In order to optimize the present and future SPARC_LAB beam line I developed an algorithm to estimate the gun solenoid misalignment in the transverse directions, avoiding the bunch centroid displacement that we experimentally observed during the machine operation. Using GPT the found misalignments are of about 0.927 mm on the x plane and of about 0.515 mm on the y plane. According to GPT simulations, performing this solenoid alignment to these values it will be possible to improve the centroid bunch displacement up to 99.4%.

Future upcoming SPARC_LAB plasma acceleration experiments will demand for perfectly circular bunches on the transverse plane. However, during the beam transport in the linac, the bunch can suffer from transverse misalignments of some devices (e.g. solenoids, accelerating structures or a misaligned laser on the cathode surface) reaching an ellipsoidal transverse shape that should be avoided. The issue of ellipticity on the transverse plane has been observed and measured during preliminary SPARC_LAB machine operations. To correct or pre-correct the transverse beam profile, achieving a circular profile at the plasma entrance, I studied the possibility to insert Printed Circuit (PC) skew quadrupoles on the SPARC_LAB beam line. The magnetic field simulation were performed using ANSYS-Maxwell code. According to the SPARC_LAB free space, these devices will be installed inside the new gun solenoid. Using GPT I optimized the longitudinal positions and the focusing gradients. Starting with an ellipsoidal bunch transverse shape of about 14% and using these devices, it will be possible to reduce up to 1% the ellipsoidal shape. Considering that also the emittances in the x and y planes has an initial difference of about 14% it will be possible to reduce this difference up to 5%.

By the simulation results obtained with GPT, currently we are modifying the new SPARC_LAB gun solenoid design with the insertion of these devices. To produce the PC quadrupoles we are evaluating the possibility to print firstly the copper circuit and after immerse it in a silicone bath. Furthermore by magnetic simulation results obtained with ANSYS Maxwell these quadrupoles can reach very high temperatures, about $T \approx 250 C^\circ$, using a current in the coils of 10 A. To fix this drawback, currently we are also planning a proper system to cool these devices. We are evaluating the possibility to position these devices directly on the solenoid coil, that has a proper water cooling.

Bibliography

- [1] <http://www.pulsar.nl/gpt/>. General particle tracer.
- [2] R. Wideröe. Über ein neues prinzip zur herstellung hoher spannungen. In *Arbeiten aus dem Elektrotechnischen Institut der Technischen Hochschule Aachen*, pages 157–176. Springer, 1929.
- [3] R. Bonifacio, L. D. S. Souza, and C. Pellegrini. *High gain, high power free electron laser: physics and application to TeV particle acceleration*. Elsevier, 2012.
- [4] P. Emma et al. First lasing and operation of an ångstrom-wavelength free-electron laser. *nature photonics*, 4(9):641–647, 2010.
- [5] M. Ferrario. Accelerator physics: basic principles on beam focusing and transport. *Proc. Int. School of Physics ‘Enrico Fermi’, Course CLXXIX, Laser-plasma acceleration, Varenna*, pages 20–25, 2011.
- [6] N. Pichoff. Beam dynamics basics in rf linacs. 2006.
- [7] S. Humphries. *Charged particle beams*. Courier Corporation, 2013.
- [8] J. Buon. Beam phase space and emittance. Technical report, Cern, 1992.
- [9] W. Barletta, L. Spentzouris, and E. Harms. Uspas notes.
- [10] J. Stohr. Linac coherent light source ii (lcls-ii) conceptual design report. Technical report, SLAC National Accelerator Laboratory (SLAC), 2011.
- [11] Brian WJ McNeil and Neil R Thompson. X-ray free-electron lasers. *Nature photonics*, 4(12):814–821, 2010.
- [12] John MJ Madey. Stimulated emission of bremsstrahlung in a periodic magnetic field. *Journal of Applied Physics*, 42(5):1906–1913, 1971.

- [13] David AG Deacon, LR Elias, John MJ Madey, GJ Ramian, HA Schwettman, and Ti I Smith. First operation of a free-electron laser. *Physical Review Letters*, 38(16):892, 1977.
- [14] James A Clarke. *The science and technology of undulators and wigglers*. Number 4. Oxford University Press on Demand, 2004.
- [15] J. S. Fraser, R. L. Sheffield, and E. R. Gray. A new high-brightness electron injector for free electron lasers driven by rf linacs. *Nuclear Instruments and Methods in Physics Research Section A: Accelerators, Spectrometers, Detectors and Associated Equipment*, 250(1-2):71–76, 1986.
- [16] B. E. Carlsten. New photoelectric injector design for the los alamos national laboratory xuv fel accelerator. *Nuclear Instruments and Methods in Physics Research Section A: Accelerators, Spectrometers, Detectors and Associated Equipment*, 285(1-2):313–319, 1989.
- [17] J.E. Clendenin. Rf photoinjectors. In *Conf. Proc.*, volume 9608262, pages 298–302, 1996.
- [18] K. J. Kim. Rf and space-charge effects in laser-driven rf electron guns. *Nuclear Instruments and Methods in Physics Research Section A: Accelerators, Spectrometers, Detectors and Associated Equipment*, 275(2):201–218, 1989.
- [19] B. E. Carlsten. Space charge induced emittance compensation in high brightness photoinjectors. *Part. Accel.*, 49:27–65, 1995.
- [20] M. E. Jones and B. E. Carlsten. Space-charge induced emittance growth in the transport of high-brightness electron beams. In *Proc. 1987 IEEE Particle Accelerator Conference, IEEE Catalog*, number 87CH2387-9, page 1319, 1987.
- [21] M. Ferrario, J. E. Clendenin, D. T. Palmer, J. B. Rosenzweig, and L. Serafini. Homodyn study for the lcls rf photo-injector. In *The Physics of High Brightness Beams*, pages 534–563, 2000.
- [22] M. Ferrario et al. Direct measurement of the double emittance minimum in the beam dynamics of the sparc high-brightness photoinjector. *Physical review letters*, 99(23):234801, 2007.
- [23] L. Serafini and J. B. Rosenzweig. Envelope analysis of intense relativistic quasilaminar beams in rf photoinjectors: ma theory of emittance compensation. *Physical Review E*, 55(6):7565, 1997.

- [24] L. Serafini, R. Rivolta, L. Terzoli, and C. Pagani. Rf gun emittance correction using unsymmetrical rf cavities. *Nuclear Instruments and Methods in Physics Research Section A: Accelerators, Spectrometers, Detectors and Associated Equipment*, 318(1):275–281, 1992.
- [25] D. H. Dowell. Electron emission and cathode emittance. *High Brightness Electron Injectors for Light Sources*, pages 4–5, 2010.
- [26] David H Dowell and John F Schmerge. Quantum efficiency and thermal emittance of metal photocathodes. *Physical Review Special Topics-Accelerators and Beams*, 12(7):074201, 2009.
- [27] T. Rao and D. H. Dowell. An engineering guide to photoinjectors. *arXiv preprint arXiv:1403.7539*, 2014.
- [28] D. H. Dowell, F. K. King, R. E. Kirby, J. F. Schmerge, and J. M. Smedley. In situ cleaning of metal cathodes using a hydrogen ion beam. *Physical Review Special Topics-Accelerators and Beams*, 9(6):063502, 2006.
- [29] M. Krasilnikov. Impact of the cathode roughness on the emittance of an electron beam. In *Proceedings of FEL 2006 Conference, Berlin, Germany*, pages 583–586, 2006.
- [30] D. Xiang, W. H. Huang, Y. C. Du, L. X. Yan, R. K. Li, C. X. Tang, and Y. Z. Lin. First principle measurements of thermal emittance for copper and magnesium. In *Particle Accelerator Conference, 2007. PAC. IEEE*, pages 1049–1051. IEEE, 2007.
- [31] D. Alesini et al. High power test results of the eli-np s-band gun fabricated with the new clamping technology without brazing. In *8th Int. Particle Accelerator Conf.(IPAC'17), Copenhagen, Denmark, 14–19 May, 2017*, pages 3662–3665. JACOW, Geneva, Switzerland, 2017.
- [32] D. T. Palmer. *The next generation photoinjector*. PhD thesis, 1998.
- [33] L. Serafini and M. Ferrario. Velocity bunching in photo-injectors. In *AIP conference proceedings*, volume 581, pages 87–106. AIP, 2001.
- [34] M. Bellaveglia, D. Alesini, M. Ferrario, and A. Gallo. An rf gun pulse shaping system to increase the accelerating gradient. 2011.
- [35] T. P. Wangler. *RF Linear accelerators*. John Wiley & Sons, 2008.
- [36] J. W. Wang. Some problems on rf breakdown in room temperature accelerator structure, a possible criterion. Technical report, SLAC/AP-51, 1986.

- [37] D. P. Pritzkau and R. H. Siemann. Experimental study of rf pulsed heating on oxygen free electronic copper. *Physical Review Special Topics-Accelerators and Beams*, 5(11):112002, 2002.
- [38] V. A. Dolgashev, S. G. Tantawi, A. D. Yermian, D. W. Martin, J. R. Lewandowski, and S. P. Weathersby. Study of rf breakdown in normal conducting cryogenic structure. In *Conf. Proc.*, volume 1205201, pages 3368–3370, 2012.
- [39] J. B. Rosenzweig et al. Next generation high brightness electron beams from ultra-high field cryogenic radiofrequency photocathode sources. *arXiv preprint arXiv:1603.01657*, 2016.
- [40] V. Dolgashev, S. Tantawi, Y. Higashi, and B. Spataro. Geometric dependence of radio-frequency breakdown in normal conducting accelerating structures. *Applied Physics Letters*, 97(17):171501, 2010.
- [41] A. Grudiev, S. Calatroni, and W. Wuensch. New local field quantity describing the high gradient limit of accelerating structures. *Physical Review Special Topics-Accelerators and Beams*, 12(10):102001, 2009.
- [42] A. S. Pohjonen, F. Djurabekova, K. Nordlund, A. Kuronen, and S. P. Fitzgerald. Dislocation nucleation from near surface void under static tensile stress in cu. *Journal of Applied Physics*, 110(2):023509, 2011.
- [43] M. C. Divall, E. Prat, S. Bettoni, C. Vicario, A. Trisorio, T. Schietinger, and C. P. Hauri. Intrinsic emittance reduction of copper cathodes by laser wavelength tuning in an rf photoinjector. *Physical Review Special Topics-Accelerators and Beams*, 18(3):033401, 2015.
- [44] O. J. Luiten, S. B. Van der Geer, M. J. De Loos, F. B. Kiewiet, and M. J. Van Der Wiel. How to realize uniform three-dimensional ellipsoidal electron bunches. *Physical review letters*, 93(9):094802, 2004.
- [45] R. K. Li, K. G. Roberts, C. M. Scoby, H. To, and P. Musumeci. Nanometer emittance ultralow charge beams from rf photoinjectors. *Physical Review Special Topics-Accelerators and Beams*, 15(9):090702, 2012.
- [46] D. Filippetto, P. Musumeci, M. Zolotarev, and G. Stupakov. Maximum current density and beam brightness achievable by laser-driven electron sources. *Physical Review Special Topics-Accelerators and Beams*, 17(2):024201, 2014.
- [47] M. Ferrario et al. Experimental demonstration of emittance compensation with velocity bunching. *Physical review letters*, 104(5):054801, 2010.

- [48] A. Bacci, M. Migliorati, L. Palumbo, and B. Spataro. An x-band structure for a longitudinal emittance correction at sparc. *SIS-Pubblicazioni, LNF-INFN, LNF*, 3(008), 2003.
- [49] H. Fares. private communication.
- [50] J. Rosenzweig. *Fundamentals of beam physics*. Oxford University Press Oxford, 2003.
- [51] D. Alesini et al. Design, realization and test of c-band accelerating structures for the sparc_lab linac energy upgrade. *Nuclear Instruments and Methods in Physics Research Section A: Accelerators, Spectrometers, Detectors and Associated Equipment*, 837:161–170, 2016.
- [52] T. Sakurai, H. Ego, T. Inagaki, T. Asaka, D. Suzuki, S. Miura, and Y. Otake. C-band disk-loaded-type accelerating structure for a high acceleration gradient and high-repetition-rate operation. *Physical Review Accelerators and Beams*, 20(4):042003, 2017.
- [53] R. Akre et al. Commissioning the linac coherent light source injector. *physical review special topics-accelerators and beams*, 11(3):030703, 2008.
- [54] H. Qian, D. Filippetto, and F. Sannibale. S-band photoinjector investigations by multiobjective genetic optimizer. In *7th International Particle Accelerator Conference (IPAC'16), Busan, Korea, May 8-13, 2016*, pages 3979–3982. JACOW, Geneva, Switzerland, 2016.
- [55] A. Bacci, A. R. Rossi, et al. Ultra-short electron bunches by velocity bunching as required for plasma wave accelerations. *Nuclear Instruments and Methods in Physics Research Section A: Accelerators, Spectrometers, Detectors and Associated Equipment*, 740:42–47, 2014.
- [56] F. Fusco. Campo magnetico sull'asse di un solenoide, <http://osiris.df.unipi.it/fusco/dida/solenoide.pdf>.
- [57] H. Wiedemann et al. *Particle accelerator physics*, volume 314. Springer, 2007.
- [58] W. Beinhauer, R. Cee, W. Koch, M. Krassilnikov, A. Novokhatski, S. Ratschow, T. Weiland, P. Castro, and S. Schreiber. Beam-based alignment of ttf rf-gun using v-code. In *Particle Accelerator Conference, 2001. PAC 2001. Proceedings of the 2001*, volume 4, pages 3099–3101. IEEE, 2001.
- [59] B. Bolli, S. Ceravolo, M. Esposito, F. Iungo, M. Paris, M. Preger, C. Sanelli, F. Sardone, F. Sgamma, M. Troiani, P. Musumeci, G. Bazzano, D. Bianculli, and

I. De Cesaris. Magnetic measurements on the gun focusing solenoid. Technical report, SPARC-MM-05/003, 20 September, 2005.